Title

Rational Design of Peptide-Modified Nanoparticles for use as Targeted Diagnostic and Drug Delivery Vehicles

Permalink

https://escholarship.org/uc/item/8hh9j6b0

Author

Mlinar, Laurie Beth

Publication Date

2014

Peer reviewed|Thesis/dissertation

Rational Design of Peptide-Modified Nanoparticles for use as Targeted Diagnostic and Drug Delivery Vehicles

by

Laurie Beth Mlinar

A dissertation submitted in partial satisfaction of the

requirements for the degree of

Doctor of Philosophy

in

Chemical Engineering

in the

Graduate Division

of the

University of California, Berkeley

Committee in charge:

Professor Matthew Tirrell, Chair
Professor David Schaffer
Professor Rachel Segalman
Professor Sanjay Kumar

Fall 2014

Rational Design of Peptide-Modified Nanoparticles for use as Targeted Diagnostic and Drug Delivery Vehicles

by

Laurie Beth Mlinar

Abstract

Rational Design of Peptide-Modified Nanoparticles for use as Targeted Diagnostic and Drug Delivery Vehicles

by

Laurie Beth Mlinar

Doctor of Philosophy in Chemical Engineering

University of California, Berkeley

Professor Matthew Tirrell, Chair

The use of functionalized nanoparticles in biomedical applications has become increasingly more prevalent due to the promise of using these materials as drug delivery and molecular imaging agents. Targeting of specific markers of disease *in vivo* can be achieved using functionalization techniques, such as modification of nanoparticles with short peptides. Peptides exhibit definite advantages versus whole proteins and their small size leads to the ability to display tens to hundreds of targeting peptides per nanoparticle. In this work, peptide functionalization is utilized to target both model drug delivery and imaging nanoparticles to a site of interest displayed by atherosclerotic plaques. The biocompatibility and clearance of these particles is considered as well as the overall targeting ability. After first establishing the biocompatibility and safety of these materials, the ability to create targeted nanoparticles as well as modular, multifunctional materials through the combination of multiple targeting peptides was assessed.

Two strategies are employed in this work: the formation of self-assembled peptide amphiphile micelles as potential drug delivery agents and peptide-functionalized iron oxide particles for use as molecular imaging agents. The establishment of biocompatibility was first determined using a peptide amphiphile micelle, DSPE-PEG$_{2000}$-CREKA, which specifically binds to fibrin, a marker of late stage atherosclerotic plaques. Both CREKA and PEG micelles were evaluated *in vivo* using a standard atherosclerosis mouse model, ApoE -/-. Atherosclerosis is characterized by the presentation of multiple markers of the disease and progresses from early to late stage through the growth and development of lipid-core plaques. Injection of small, spherical Cy7-labeled micelles allowed for *in vivo* near-infrared imaging. These studies showed that these micelles are cleared both through the liver and spleen, therefore involving the reticuloendothelial and renal system, respectively. Biocompatibility was observed through histological staining of excised tissues, determining the level of apoptosis in the liver and spleen, as well as testing for liver function. By varying the mole percent of Cy7 in the micelles, it was possible to determine an optimal regime for both whole body and *ex vivo* near-infrared imaging.

Utilizing the results of the biocompatibility and biodistribution of peptide amphiphile micelle study, it was found that 10 mole percent Cy7 was optimal for future

in vivo studies. While late stage targeting of atherosclerotic plaques had previously been demonstrated, the ability to actively target earlier stages of plaque formation with a model drug delivery vehicle formed from peptide amphiphile micelles had yet to be observed. Therefore, the formation of early stage targeting was achieved through DSPE-PEG_{2000}-VCAM micelles labeled with a near-infrared dye, Cy7. These micelles were designed to be small enough to extend their *in vivo* circulation time and also be spherical. The intended target, vascular cell adhesion molecule-1, or VCAM-1, is expressed by endothelial cells that line the developing plaque, making it a great target for intravenously injected particles. VCAM-1 targeting micelles were shown to accumulate in the cardiovascular system in early stage mice. Immunohistochemistry showed that VCAM-1 expression overlapped with Cy7 dye in the aortic tree, providing evidence for active targeting of early and mid-stage atherosclerotic plaques.

While active targeting was shown with VCAM-1 micelles, one of the central advantages to self-assembled micelles is the inherent ability to incorporate multifunctionality through mixing of different amphiphiles. To determine the ability to mix different peptide amphiphiles, micelles composed of DSPE-PEG_{2000}-CREKA and DSPE-PEG_{2000}-VCAM as well as diC_{16}CREKA and diC_{16}VCAM were analyzed. Both systems showed some degree of mixing via transmission electron microscopy and Förster resonance energy transfer and the region over which one population of mixed micelles were formed was established. Mixing was additionally determined using two amphiphiles that individually formed different geometry micelles, either spherical or cylindrical particles. The ability to incorporate otherwise cylindrical-forming amphiphiles into spherical micelles was demonstrated.

Each peptide amphiphile study focused on the formation of platform technologies for drug delivery. A strategy to form a targeted contrast agent was additionally developed via peptide functionalization of iron oxide particles. Using CREKA-functionalized contrast agents developed for magnetic particle imaging (MPI), the ability to bind to fibrin *ex vivo* was shown to be dependent on the amount of fibrin present, demonstrating the specific binding of these nanoparticles. The *in vivo* biodistribution additionally showed clearance through the liver, as is expected for iron oxide nanoparticles.

In each study presented, both the function of the peptide-functionalized nanoparticle system was established as well as the *in vivo* biodistribution. As the field of targeted delivery agents progresses, the design parameters as well as the establishment of biodistribution, safety, and targeting ability set forth in this work will be a guide for future studies using peptide-functionalized and targeted nanoparticles.

Table of Contents

List of Figures

List of Tables

List of Abbreviations and Symbols

ALT	alanine aminotransferase
ANOVA	analysis of variance
ApoE -/-	apolipoprotein E knockout mouse
AST	aspartate aminotransferase
CD	circular dichroism
CMC	critical micelle concentration
CREKA	cysteine-arginine-glutamic acid-lysine-alanine peptide
Cy7	Cyanine 7
DBU	1,8-diazabicyclo[5.4.0]undec-7-ene
DCM	dichloromethane
Dde	1-(4,4-dimethyl-2,6-dioxocyclohexylidene)ethyl
DIPEA	*N,N*-diisopropylethylamine
DLS	dynamic light scattering
DMF	dimethylformamide
DMSO	dimethyl sulfoxide
DPH	1,6-diphenyl-1,3,5-hexatriene
DSPE-PEG$_{2000}$-maleimide	1,2-distearoyl-sn-glycero-3-phosphoethanolamine-N-[maleimide(polyethylene glycol)-2000]
FFP	field-free point
Fmoc	fluorenylmethyloxycarbonyl chloride
FOV	field of view
FRET	Förster resonance energy transfer
FTIR	Fourier transform infrared spectroscopy
H & E	hematoxylin and eosin
HBTU	2-(1H-Benzotriazole-1-yl)-1,1,3,3-tetramethyluronium hexafluorophosphate
HOBt	hydroxybenzotriazole
HPLC	high performance liquid chromatography
HUVEC	human umbilical vein endothelial cell
LDL	low density lipoprotein
mAEC	murine aortic endothelial cell
MALDI	matrix-assisted laser desorption/ionization
MPI	magnetic particle imaging
MRI	magnetic resonance imaging
NHS	N-hydroxysuccinimide
OCT	optimum cutting temperature
PA	peptide amphiphile
PBS	phosphate buffered saline
PEG	polyethylene glycol
PSF	point spread function
RES	reticuloendothelial system
SPDP	3-(2-pyridyldithio)propionic acid *N*-hydroxysuccinimide ester
SPECT	single photon emission computed tomography
SPIO	superparamagnetic iron oxide particles

TCEP-HCL	tris(2-carboxyethyl)phosphine hydrochloride
TEM	transmission electron microscopy
TFA	trifluoroacetic acid
THF	tetrahydrofuran
UV-vis	ultraviolet-visible spectroscopy
VCAM-1	vascular cell adhesion molecule-1

Acknowledgements

It is without question that my drive to pursue a PhD in Chemical Engineering stems from my family's devotion to education. Being a woman in science has never fazed me and I owe that to two people who laid the groundwork for my career: my mother and brother. My mother's devotion to math, science, and appreciation for medical research along with my brother's own pursuit of a ChE PhD inspire me each and every day. My parents provided me with the opportunity to attend a wonderful high school, Gill St. Bernard's, and I am grateful everyday for that as I wholeheartedly believe I would not be where I am today without such an amazing educational background. To all of my family, thank you for your support. Your love and laughter make any challenge surmountable. Tim and Kirsten, I am extremely grateful for our four years together in California and for making California feel like a second home to me. To Cameron and Gavin, you never cease to make me smile and remind me what is truly most important in life.

My academic career led me to the University of Minnesota, where I not only met amazing people, but received a wonderful background in chemical engineering complete with many sleepless nights of homework. I still contend we had the best study group and without Chris and Brian, undergrad would have been much more stressful. To Adam, Beth, Becky, and Matt W, thank you for all of your support as I trudged through grad school. Missy, your support has always meant so much to me, and you never fail to put life in perspective, a very welcome attribute.

The particular subject of my PhD became evident to me in 6th grade when I learned about the potential of targeted drug delivery, a topic that has fascinated me since that time. Joining Prof. Matthew Tirrell's lab at Berkeley provided me with the amazing opportunity to design my own delivery system, an opportunity I will be forever grateful for. Thank you, Matt, for the opportunity to shape my own research and to learn from my failures to makes the successes that much greater. I appreciate all of the guidance and support throughout graduate school. While I wish the lab had stayed in Berkeley, my own research benefited from the access to different facilities in Chicago.

Graduate school would just not be the same without an amazing lab group. I am especially grateful to Rachel Marullo, Amanda Trent, Brian Lin, Katie Black, and Matt Black, who never thought twice about teaching me something new in lab and were so willing to help me learn. Katie, we survived the Berkeley lab together, and what an experience that was. Thank you especially to Dan Krogstad for all of your cryo-TEM help and expertise. Matt Kade, Surekha Gajria, Badri Ananthanarayanan, Dimitris Priftis, Sarah Perry, Lorraine Leon, Bret Ulery, Michael Lueckheide, John Barrett, and Handan Acar, it has been a pleasure working with each of you and thank you for being great labmates! I owe a special thank you to Eunji Chung for teaching me about animal experiments as well as Emily Wonder, Katie Nord, and Matthew Sugimoto for all of their hours and hours of help and assistance with each *in vivo* experiment. The CREKA biodistribution work would not have been possible without Eunji's guidance. I cannot thank you all enough for all of your time and efforts. In addition, I worked particularly closely with two undergraduates, Mohit Jethi at Berkeley and Abby Skwara in Chicago. Thank you both for all of your hard work and devotion to each of the projects that you worked on. You taught me how to be a better teacher and ultimately a better researcher.

I had the privilege of working with amazing collaborators from the Conolly and McConnell labs: Laura Croft, Patrick Goodwill, Daniel Hensley, Elaine Yu, and Hisanori Kosuge. While we worked with such a large group of people, your devotion to developing a new imaging technique was an inspiration to me and a sign of what amazing research is currently being done. Thank you, as well, to Prof. Steven Conolly for supporting our project despite its challenges. I also have to thank Carlet Altamirano for all of her assistance to make sure that I could spend the last few months of my PhD with my group in Chicago. Amber Janda and Zheng Zhai thank you each for your friendship and for making grad school that much more enjoyable.

The last, but certainly not least, person to acknowledge is someone I would have never guessed to meet in grad school: my husband. Throughout my years of schooling, my focus was on just that, school. To find someone who shares the same passions in life is a rarity and I consider myself extremely lucky to have found that one person that makes me complete. Grad school would not have been the same experience had I not spent it with Anton, who heard me practice presentations about my research probably no less than 50 times, so much so that he could almost give the talk himself. Life is about more than the pursuit of degrees or titles and Anton, you make every day more special to me than the last and for that I am and will forever be grateful. While it may take some getting used to not going to school after 22 straight years, I know that my next journey in life will be with those closest to me and for that, I feel blessed and excited.

Chapter 1

Introduction

Over the past decades, nanomedicine has significantly contributed to the development of new treatments for a wide range of diseases. One of the most underserved diseases by nanomedicine, however, is cardiovascular disease. The leading cause of cardiovascular disease, atherosclerosis, is particularly dangerous to the patient because of its asymptomatic nature. The disease itself is characterized by the formation of lipid-filled plaques within the artery wall that develop and progress oftentimes over the course of decades. Without symptoms, patients are not subjected to preemptive or preventative treatment or diagnostic imaging due to both the potential for unwelcome side effects as well as the cost. As of 2006, The American Heart Association reported that the average death rate in the United States alone due to cardiovascular disease was one death every 38 seconds [1]. It is for these reasons that this work focuses on the formation of nanomedicine-based platform technologies with the potential to diagnose and treat atherosclerosis.

It is important, then, to understand the underlying biology of atherosclerosis so that more effective therapies can be developed. The cascade of events leading to the formation of atherosclerotic plaques begins with excess circulating LDL (low density lipoprotein), a condition known as hyperlipidemia [2]. This excess LDL enters into the artery wall and is oxidized, resulting in the upregulation of inflammatory markers, such as vascular cell adhesion molecule-1 (VCAM-1) [2-4]. VCAM-1, which is expressed by endothelial cells that line the artery [3, 5-7], facilitates adhesion of monocytes to the artery wall, a process that, under normal conditions, is resisted by endothelial cells [3]. After monocytes enter through the artery wall, they differentiate to become macrophages that consume the excess LDL and transform into foam cells [8]. Over time, smooth muscle cells move from the media to the intima where the lipid-filled plaques developed [2, 8]. Apoptosis of macrophages and smooth muscle cells leads to the necrotic lipid core characteristic of an advanced stage plaque [8]. The development of a fibrous cap can be protective [9], but a thin fibrous cap can lead to rupture of the plaque and the formation of a thrombus [8]. This work focuses on targeting two markers of atherosclerosis: VCAM-1 and fibrin, via targeting of the fibrous cap. These two markers represent an opportunity to demarcate different stages of plaque formation from one of the earliest markers, VCAM-1, to a very late stage marker in fibrin.

In order to target and bind to these markers of atherosclerosis, previously established short peptides that bind to VCAM-1 [10] and fibrin [11] were used. One method of incorporating these peptides into targeted drug delivery or diagnostic agents is through the use of peptide amphiphile micelles. Peptide amphiphiles are formed through the conjugation of a hydrophilic peptide to a hydrophobic alkyl tail [12]. Two hydrophobic tails are utilized in this work: DSPE-PEG$_{2000}$, which is formed from two eighteen carbon alkyl chains conjugated to a 2,000 molecular weight polyethylene glycol polymer as well as diC$_{16}$, formed from two sixteen carbon alkyl chains. Each tail is conjugated to a peptide using either a thioether bond for the DSPE-PEG$_{2000}$ tail or an amide bond when using the diC$_{16}$ tail. Peptide amphiphiles have been used for a number of different biomedical applications including targeting atherosclerotic plaques [11] and tumors [13-15], the formation of vaccines [16], as well as biomaterial scaffolds [17-19]. These micelles are amenable to biomedical applications due to their low critical micelle concentrations, which leads to stable formulations that have the potential to be injected *in vivo* and remain in micelle form in circulation [2]. In addition, the hydrophobic interior provides a means to encapsulate hydrophobic drugs or imaging agents that are otherwise insoluble [2, 20, 21]. Spherical micelles formed within the range of 10-200 nm have also been shown to lead to prolonged circulation times when using nanoparticles [2], which can lead to an increase in the targeting efficiency of the particles. Therefore, when considering micelles as drug delivery agents, the shape formed becomes exceedingly important. Micelle shape can be predicted using the critical packing parameter as detailed in Table 1.1. The critical packing parameter has been successfully used to describe the geometry formed when using surfactants, but the theory can also be applied to peptide amphiphiles. The critical packing parameter is described by v/a_0l_c where v is the hydrophobic tail volume, a_0 denotes the optimal surface area of the headgroup that comes in contact with the hydrophobic tail, and l_c is the critical chain length of the hydrophobic tail [22]. Using geometrical arguments, the critical packing parameter can help to describe the micelle shape that is formed. Due to the incorporation of charged amino acids and peptide secondary structure, this prediction measure is not perfect for peptide amphiphile micelles, but provides a guide for understanding and predicting the micelle shape expected. This is a powerful tool when one considers the importance of size and shape, especially for biomedical applications.

In Chapter 2, the use of a model peptide amphiphile, DSPE-PEG$_{2000}$-CREKA, which was previously shown to bind to fibrin *in vivo* [11], was utilized to assess the biocompatibility and clearance of peptide amphiphile micelles in a mouse model of atherosclerosis. Cy7, a near-infrared dye, was incorporated into the micelles to provide a means to image the mice as well as the excised organs to determine both the biodistribution and clearance mechanisms of peptide amphiphile micelles. After establishing the biocompatibility of peptide amphiphile micelles *in vivo* after 24 hours in circulation, Chapter 3 discusses the formation of an earlier stage atherosclerotic plaque targeting micelle. Using a micelle designed to bind to VCAM-1, the *in vivo* targeting ability of VCAM-1 targeted micelles was established versus a long-circulating PEG micelle control. To show active targeting, VCAM-1 targeted micelles were therefore compared to a passive control nanoparticle, which, due to its increased circulation time, can accumulate non-specifically at plaques. In both early and mid-stage atherosclerotic mice, VCAM-1 targeted and Cy7 labeled micelles showed a two-fold enhancement in Cy7 signal in the aortic tree versus similarly labeled PEG micelles. This study provides a means to target earlier stages of plaque progression using a micelle construct that has the potential of carrying a payload of either diagnostic or therapeutic agents to the site of plaque formation.

Peptides can additionally be used to functionalize contrast agents to create molecularly targeted imaging agents. While both noninvasive as well as invasive techniques have been used to image atherosclerotic plaques, each technique has certain advantages and disadvantages. In this work, the use of magnetic particle imaging (MPI) is explored due to its inherent advantages such as the lack of ionizing radiation and excellent contrast as no signal is expected from background tissue [23, 24]. Chapter 4, therefore, discusses the functionalization of iron oxide particles with the short peptide, CREKA, to create a fibrin binding nanoparticle. *In vitro* results point to the promise of using targeted contrast agents with MPI as the MPI signal is shown to be linearly dependent on the amount of fibrin present. In fact, using a non-labeled control, no such response is observed. Translation of these results *in vivo* would provide the potential to quantify the deposition of targeted contrast agents throughout the aortic tree and allow for monitoring over time.

Building upon the establishment of both early and late stage targeting using VCAM-1 and fibrin binding peptides, Chapter 5 shows that these two peptides and their respective amphiphiles can be incorporated into mixed micelles. The extent of mixing, a key consideration when forming mixed micelles, is additionally considered. When analyzing the critical packing parameter, one might expect to form cylindrical micelles with the amphiphile diC$_{16}$CREKA due to the large hydrophobic tail volume and short peptide headgroup. In fact, transmission electron microscopy shows the formation of long, cylindrical micelles formed from this amphiphile. However, certain applications dictate the formation of spherical nanoparticles. In Chapter 5, the use of both peptide amphiphiles as well as non-peptide labeled amphiphiles are shown to confer a spherical particle when self-assembled with the otherwise cylindrical micelle forming diC$_{16}$CREKA. The parameters over which spherical micelles are observed, dictated by the mole percentage of each amphiphile, is established.

With each application of peptide-functionalized and peptide-targeted nanoparticles within this work, the extent of targeting, biocompatibility, as well as certain design parameters are considered. As the nanomedicine field continues to grow, both peptide amphiphile micelles as well as peptide-targeted contrast agents provide a means to address an otherwise underserved disease, cardiovascular disease. Through an understanding of how these materials interact with the body via the consideration of targeting efficiency, biocompatibility, and clearance combined with an appreciation for the design aspects of multi-functional nanoparticles, a new avenue of innovation within nanomedicine could be enabled.

Table 1.1 Predicted micelle shape using the critical packing parameter. Adapted from Israelachvili JN. Intermolecular and surface forces. 3rd ed. San Diego: Elsevier; 2011, p. 538-50.

Micelle Shape	**Critical Packing Parameter**
Sphere	< ⅓
Cylinder	⅓ - ½
Vesicle	½ - 1

References:

[1] Lloyd-Jones D, Adams RJ, Brown TM, Carnethon M, Dai S, De Simone G, et al. Executive summary: heart disease and stroke statistics-2010 update: a report from the American Heart Association. Circulation 2010;121:948-54.
[2] Lewis DR, Kamisoglu K, York AW, Moghe PV. Polymer-based therapeutics: nanoassemblies and nanoparticles for management of atherosclerosis. Wiley Interdiscip Rev Nanomed Nanobiotechnol 2011;3:400-20.
[3] Libby P. Inflammation in atherosclerosis. Nature 2002;420:868-74.
[4] Hansson GK, Libby P. The immune response in atherosclerosis: a double-edged sword. Nat Rev Immunol 2006;6:508-19.
[5] Nahrendorf M, Jaffer FA, Kelly KA, Sosnovik DE, Aikawa E, Libby P, et al. Noninvasive vascular cell adhesion molecule-1 imaging identifies inflammatory activation of cells in atherosclerosis. Circulation 2006;114:1504-11.
[6] Iiyama K, Hajra L, Iiyama M, Li H, DiChiara M, Medoff BD, et al. Patterns of vascular cell adhesion molecule-1 and intercellular adhesion molecule-1 expression in rabbit and mouse atherosclerotic lesions and at sites predisposed to lesion formation. Circ Res 1999;85:199-207.
[7] Cybulsky MI, Iiyama K, Li H, Zhu S, Chen M, Iiyama M, et al. A major role for VCAM-1, but not ICAM-1, in early atherosclerosis. J Clin Invest 2001;107:1255-62.
[8] Libby P, Ridker PM, Hansson GK. Progress and challenges in translating the biology of atherosclerosis. Nature 2011;473:317-25.
[9] Libby P, Aikawa M. Stabilization of atherosclerotic plaques: new mechanisms and clinical targets. Nat Med 2002;8:1257-62.
[10] Kelly KA, Nahrendorf M, Yu AM, Reynolds F, Weissleder R. In vivo phage display selection yields atherosclerotic plaque targeted peptides for imaging. Mol Imaging Biol 2006;8:201-7.
[11] Peters D, Kastantin M, Kotamraju VR, Karmali PP, Gujraty K, Tirrell M, et al. Targeting atherosclerosis by using modular, multifunctional micelles. Proc Natl Acad Sci U S A 2009;106:9815-9.
[12] Berndt P, Fields GB, Tirrell M. Synthetic lipidation of peptides and amino acids: monolayer structure and properties. J Am Chem Soc 1995;117:9515-22.
[13] Chung EJ, Cheng Y, Morshed R, Nord K, Han Y, Wegscheid ML, et al. Fibrin-binding, peptide amphiphile micelles for targeting glioblastoma. Biomaterials 2014;35:1249-56.
[14] Missirlis D, Krogstad DV, Tirrell M. Internalization of p53(14-29) peptide amphiphiles and subsequent endosomal disruption results in SJSA-1 cell death. Mol Pharm 2010;7:2173-84.
[15] Missirlis D, Khant H, Tirrell M. Mechanisms of peptide amphiphile internalization by SJSA-1 cells in vitro. Biochemistry 2009;48:3304-14.
[16] Black M, Trent A, Kostenko Y, Lee JS, Olive C, Tirrell M. Self-assembled peptide amphiphile micelles containing a cytotoxic T-cell epitope promote a protective immune response in vivo. Adv Mater 2012;24:3845-9.
[17] Lin BF, Megley KA, Viswanathan N, Krogstad DV, Drews LB, Kade MJ, et al. pH-responsive branched peptide amphiphile hydrogel designed for applications in

regenerative medicine with potential as injectable tissue scaffolds. J Mater Chem 2012;22:19447-54.
[18] Niece KL, Hartgerink JD, Donners JJ, Stupp SI. Self-assembly combining two bioactive peptide-amphiphile molecules into nanofibers by electrostatic attraction. J Am Chem Soc 2003;125:7146-7.
[19] Webber MJ, Tongers J, Newcomb CJ, Marquardt KT, Bauersachs J, Losordo DW, et al. Supramolecular nanostructures that mimic VEGF as a strategy for ischemic tissue repair. Proc Natl Acad Sci U S A 2011;108:13438-43.
[20] Trent A, Marullo R, Lin B, Black M, Tirrell M. Structural properties of soluble peptide amphiphile micelles. Soft Matter 2011;7:9572-82.
[21] Lukyanov AN, Torchilin VP. Micelles from lipid derivatives of water-soluble polymers as delivery systems for poorly soluble drugs. Adv Drug Deliv Rev 2004;56:1273-89.
[22] Israelachvili JN. Intermolecular and surface forces. 3rd ed. San Diego: Elsevier; 2011, p. 538-50.
[23] Goodwill PW, Tamrazian A, Croft LR, Lu CD, Johnson EM, Pidaparthi R, et al. Ferrohydrodynamic relaxometry for magnetic particle imaging. Appl Phys Lett 2011;98:262502.
[24] Goodwill PW, Saritas EU, Croft LR, Kim TN, Krishnan KM, Schaffer DV, et al. X-space MPI: magnetic nanoparticles for safe medical imaging. Adv Mater 2012;24:3870-7.

Chapter 2

In Vivo Biodistribution and Safety of Peptide Amphiphile Micelles

Abstract

Peptide amphiphile micelles present a growing class of materials used widely in a number of biomedical applications. In order to translate *in vivo* functionality studies to the clinic, it is necessary to evaluate the biodistribution and safety of these materials. Small, spherical, Cy7-labeled peptide amphiphile (PA) micelles specifically formed through the use of the fibrin-binding peptide CREKA were evaluated *in vivo* versus a PEG micelle as well as PBS control. *In vivo* biocompatibility, biodistribution, and clearance of PA micelles was evaluated. No toxicity was observed via liver and spleen cytotoxity assays as measured by caspase-3 activity, liver function through ALT and AST levels were found to be normal, and histological analysis of the aortic tree, heart, lung, liver, spleen, intestines, kidney, or bladder in a murine model of atherosclerosis, ApoE -/- mice, showed no signs of tissue damage. Clearance was observed through both the liver and kidney, showing both reticuloendothelial and renal system involvement. Analysis of Cy7 signal in the kidney provided evidence that, despite changing the mole percentage of Cy7 from 2.5 to 25 percent, no change in the pattern of clearance was observed. This study represents the first analysis of PA micelle distribution and safety in the literature and shows the potential of using PA micelles clinically due to their biocompatibility.

2.1 Introduction

Targeted nanoparticles represent a developing technology with the promise of delivering both therapeutic and diagnostic agents specifically to a biological marker within the body [1]. Specific targeting has been shown through the incorporation of either an antibody or peptide [1-5] that can bind to a target of interest. The use of a short peptide has certain advantages over the use of a whole protein, namely the ability to escape immune recognition and lead to an increase in tissue penetration [6-8]. The ability to avoid immediate clearance via the immune system may lead to increased circulation time for peptide-based nanoparticle systems versus protein-targeted particles. One class of peptide-based materials that shows great promise as a drug delivery vehicle or diagnostic agent are peptide amphiphile (PA) micelles. PAs are formed by conjugating a hydrophilic peptide headgroup to a hydrophobic lipid tail [9]. PAs self-assemble in aqueous conditions to form micelles with a hydrophobic interior and hydrophilic corona. Peptides are displayed within the hydrophilic corona; these peptides then provide a means to bind to specific targets. Two qualities of PA micelles that confer a particularly favorable nanoparticle system for targeting diseased tissues are the concentrated and multivalent display of peptides as well as the ability to integrate multifunctionality into micelles through the incorporation of multiple different amphiphiles [3]. In fact, due to the self-assembled nature of PA micelles, a variety of amphiphiles, such as those that target, present a therapeutic peptide, or provide a means to image the target of interest can all be incorporated into the same micelle construct.

PA micelles have been shown to be successful at targeting or imaging atherosclerosis [3] and cancer [10-12], as well as forming biomaterials for tissue engineering [13-15]. One particularly interesting PA micelle was formed from a peptide shown to bind specifically to fibrin. This pentapeptide, CREKA (cysteine-arginine-glutamic acid-lysine-alanine), has been shown to target PA micelles to sites of fibrin deposition in the aortic tree of atherosclerotic mice [3]. Co-delivery of a therapeutic peptide, hirulog, was also demonstrated with this micelle system.

Here, we evaluate the *in vivo* biodistribution and clearance of a PA micelle system composed of DSPE-PEG$_{2000}$-CREKA versus a PEG micelle construct. Functionalization of nanoparticles as well as drugs and other particulate systems with polyethylene glycol (PEG) has been shown to increase the *in vivo* circulation time [16]. This phenomena has been attributed to the ability of PEG to create a hydrophilic exterior that can prevent opsonin binding [17]. PEG micelles were therefore used as a control system to compare PA micelles formed from the peptide CREKA to a long-circulating nanoparticle construct. Biodistribution and clearance of nanoparticles is related to many properties such as the surface charge, hydrophilicity, and shape. The effect of surface charge is debated as studies have shown that both positive and negative surface charge leads to an increase in clearance [18-20]. Positively charged particles are thought to be cleared due to their association with the negatively charged cell membrane leading to an increase in phagocytosis by macrophages [18]. Alternatively, negatively charged particles can bind to the cationic or positive regions of macrophages [18]. The magnitude of the surface charge or zeta potential is therefore thought be play the most important role as larger values, either positive or negative, lead to an increase in macrophage uptake [18]. The adsorption of plasma proteins onto the surface of nanoparticles is thought to affect clearance through the reticuloendothelial system via macrophages as well [21]. Protein adsorption can also be related to the surface charge of the nanoparticle.

Similarly, the relative hydrophilicity of particles plays an important role in clearance, where more hydrophobic particles are phagocytosed to a greater degree [19]. The shape of the nanoparticles also affects *in vivo* biodistribution [22, 23] and depending on the target, can influence the particle's ability to reach the intended location. In this study, nanoparticles with a similar magnitude zeta potential, relative hydrophilicity, and shape are utilized. PEG and CREKA micelles differ in their surface charge, but both form small, nanometer scale, spherical micelles.

PEG and CREKA micelles were injected intravenously using a mouse model of athersclerosis, ApoE -/- mice, and the relative biodistribution, clearance, and safety of the micelle formulation was assessed after 24 hours in circulation. Near infrared imaging was utilized to image live mice combined with imaging of the excised organs. A range of concentrations of dye-labeled amphiphiles were mixed with the PEG and CREKA amphiphiles to form 2.5, 5, 10, and 25 mole percent dye-labeled micelles. The range of dye addition led to a comparison of the ability to image the deposition and biodistibution of these micelles *in vivo*, while remaining non-toxic to the mouse and determine the optimal working concentrations for future PA micelle studies.

2.2 Materials and Methods

2.2.1 Micelle Synthesis and Preparation

CREKA (Cys-Arg-Glu-Lys-Ala) peptide was synthesized on rink amide resin using an automated peptide synthesizer (PS3 Benchtop Peptide Synthesizer, Protein Technologies, Tucson, AZ) using standard Fmoc peptide synthesis techniques [9, 24, 25]. To acetylate the N-terminus of the peptide, 10x molar excess of acetic anhydride (Sigma-Aldrich, St. Louis, MO) in dimethylformamide (DMF, Sigma-Aldrich, St. Louis, MO) was utilized after deprotection of the final Fmoc group. To cleave the peptide from resin and deprotect amino acid side chains, a trifluoroacetic acid (TFA):triisopropylsilane:water:1,2-ethanedithiol (94:1:2.5:2.5) solution was mixed with the peptide-containing resin for 2 hours. The resulting product was precipitated in cold diethyl ether. Peptide was first purified using a reverse phase high performance liquid chromatograph (HPLC, Prominence, Shimadzu Corporation, Kyoto, Japan) with a C_8 Waters column (Waters Corporation, Milford, MA) prior to conjugation to the DSPE-PEG_{2000} tail. The resulting peptide product identity was confirmed using matrix-assisted laser desorption/ionization (MALDI) mass spectrometry (Biflex III, Bruker, Billerica, MA, USA).

To form the peptide amphiphile, DSPE-PEG_{2000}-CREKA, pure peptide was mixed with 1,2-distearoyl-sn-glycero-3-phosphoethanolamine-N-[maleimide(polyethylene glycol)-2000] (DSPE-PEG_{2000}-maleimide) (Avanti Polar Lipids, Alabaster, AL) in water using a 10% molar excess of peptide. Dilute sodium hydroxide was used to maintain the pH between 6.5 and 7.5. The solution was aggitated overnight at room temperature. Purification proceeded using the method described above on a C_4 Waters column. To determine the concentration of PA in solution, amino acid analysis was utilized (Molecular Structure Facility, UC Davis, Davis, CA).

DSPE-PEG_{2000}-Cy7 was formed by reaction of N-hydroxysuccinimide (NHS) ester Cyanine 7 (Cy7) dye (GE Healthcare, Buckinghamshire, England) with 10% molar excess of DSPE-PEG_{2000}-amine (Avanti Polar Lipids, Alabaster, AL, USA) in 10 mM aqueous sodium carbonate buffer (pH= 8.5) for 24 hours. Purification was completed using the method described above on a C_4 Waters column.

After purification of each amphiphile, micelles were formed by first lyophilizing the amphiphiles and subsequently dissolving the amphiphiles in methanol. CREKA micelles were formed by careful measurement of various ratios of DSPE-PEG_{2000}-Cy7: DSPE-PEG_{2000}-CREKA (2.5:97.5, 5:95, 10:90, 25:75). A methanol film was formed in the interior wall of a glass vial and dried under vacuum overnight. Films were then hydrated in water or PBS, vortexted, and allowed to incubate at 80°C for 30 minutes to completely form mixed micelles. Similarly, PEG micelles were formed using DSPE-PEG_{2000}-Cy7: DSPE-PEG_{2000}-maleimide (2.5:97.5, 5:95, 10:90, 25:75) and prepared as described above.

2.2.2 Micelle Characterization

Micelles were analyzed to determine both size and shape using two methods. The hydrodynamic diameter was evaluated using a single angle Viscotek 802 DLS (Malvern Instruments, Malvern, UK) with 200 μM micelle solutions. The hydrodynamic radius was calculated by using the diffusion coefficient as determined from the auto correlation function. In addition to DLS, transmission electron microscopy (TEM) was performed to determine the size and shape of the resulting micelles. An accelerating voltage of 120 kV with a FEI Tecnai 12 TEM was used for imaging. CREKA and PEG micelle solutions were prepared at 200 μM in water. 1 μL of sample was loaded onto ultrathin carbon type-A 400 mesh copper grids and allowed to nearly dry. Excess solution was removed by filter paper and grids were blotted with water to remove excess salt. Finally, 1 μL of a phophotungstic acid in water solution was applied for 2 minutes. Excess solution was removed and grids were imaged dry.

To determine the zeta potential of CREKA and PEG micelles, 100 μM DSPE-PEG_{2000}-CREKA or DSPE-PEG_{2000}-maleimide micelle solutions in water were measured using a Zetasizer Nano ZS (Malvern Worcestershire, United Kingdom, N=3).

2.2.3 In Vivo Animal Experiments

Female, transgenic mice homozygous for the $ApoE^{tm1Unc}$ mutation (The Jackson Laboratory, Bar Harbor, ME) were fed a high fat diet beginning at an age of 4 weeks. The diet is composed of 21% (wt/wt) fat, 0.15% (wt/wt) cholesterol, 19.5% (wt/wt) casein, and no sodium cholate (Harlan TD.88137, Indianapolis, Indiana) and the mice were fed for 22 weeks to generate stage V lesions [26]. To image the mice, they were first shaved and an application of Nair was used to remove any residual fur. Prior to injection, the tail vein was sterilized and dilated with 70% ethanol. Injections were administered intraveneously and were composed of 100 μL of a 1 mM solution of DSPE-PEG_{2000}-Cy7:DSPE-PEG_{2000}-CREKA (2.5:97.5, 5:95, 10:90, 25:75 by mole percentage) to form CREKA micelles or DSPE-PEG_{2000}-Cy7:DSPE-PEG_{2000}-maleimide (2.5:97.5, 5:95, 10:90, 25:75) to form PEG micelles ($N \geq 3$). Each solution was suspended in 1X PBS and 100 μL of 1X PBS alone was injected as a control. After allowing micelles to circulate for 24 hours, mice were anesthetized with 2.5% isoflurane in O_2 and near-infrared whole body imaging was completed using an IVIS 200 (Xenogen, PerkinElmer, Waltham, MA). Mice were euthanized via CO_2 overdose. The aortic tree, heart, lung, liver, spleen, intestines, kidney, and bladder were harvested for both histological analysis and toxicity studies. Organs were imaged using near-infrared imaging with an IVIS 200 to allow for quantification of the resulting fluorescence signal with PerkinElmer's Living Image software. All animals were housed at The University of Chicago and all protocols were approved by the University of Chicago's Institutional Animal Care and Use Committee (Chicago, IL)

2.2.4 Liver and Spleen Cytotoxicity Assays

Liver and spleen cytotoxicity was assessed by determining the level of apoptosis through the quantification of caspase-3 activity using a colorimetric assay (R&D Systems, Minneapolis, MN). To further determine liver function, alanine aminotransferase (ALT) and aspartate aminotransferase (AST) were measured using an equal mass of homogenized tissue in lysis buffer via a commercial assay kit for each aminotransferase (Sigma-Aldrich, St. Louis, MO). Statistical significance was calculated using the Student's t-test between means of pairs. Analysis of variance (ANOVA) with Newman-Keuls multiple comparison test post-hoc analysis was employed when comparing differences between three or greater means.

2.2.5 Histology

After excision of the aortic tree, heart, lung, liver, spleen, intestines, kidney, and bladder, each tissue was washed in 1X PBS to prepare for fixation. Tissues were fixed in

4% paraformaldehyde at 4°C overnight and subsequently submerged in 30% sucrose solution for 8 hours. Samples were then frozen in OCT (Tissue Tek, Sakura Finetek, Torrance, CA). Tissues were cryosectioned using a Microm HM 505 E (MICROM International GmbH, Walldorf, Germany) cryomicrotome and stained with hematoxylin and eosin (H&E). Imaging of the slides was completed using a DMI6000 B Leica Microsystems (Wetzlar, Germany) microscope.

2.3 Results

2.3.1 Synthesis and Characterization of Micelles

CREKA micelles were formed through a thioether linkage to DSPE-PEG$_{2000}$-maleimide to form DSPE-PEG$_{2000}$-CREKA. PEG micelles were formed from the monomer alone, DSPE-PEG$_{2000}$-maleimide. Negative stain transmission electron microscopy (TEM) showed the formation of small, nanometer scale, spherical nanoparticles for both PEG and CREKA micelles (Figure 2.1). Through dynamic light scattering (DLS), it was determined that the hydrodynamic diameter of PEG micelles was 9.6 ± 0.2 nm and CREKA micelles formed 13.2 ± 0.8 nm diameter particles (Figure 2.2 and Table 2.1). DLS also showed the presence of one population of micelles with a tight size distribution for both micelle groups. The surface charge of each micelle system was determined via the zeta potential. PEG micelles were found to have a zeta potential of -23 ± 5 mV whereas CREKA micelles had a positive zeta potential of 36 ± 2 mV (Table 2.1).

Mixed micelles formed from the amphiphiles, DSPE-PEG$_{2000}$-maleimide and DSPE-PEG$_{2000}$-Cy7 or DSPE-PEG$_{2000}$-CREKA and DSPE-PEG$_{2000}$-Cy7, at varying ratios of the two amphiphiles were used *in vivo* to determine the overall biodistribution of micelles when changing the percentage of each amphiphile. The molar percentage of DSPE-PEG$_{2000}$-Cy7 used was 2.5%, 5%, 10%, or 25%.

2.3.2 Biodistribution and Clearance In Vivo

ApoE -/- mice were intravenously injected with either PEG or CREKA micelles containing 2.5, 5, 10, or 25 mol% Cy7 amphiphile. Micelles were allowed to circulate for 24 hours prior to live, *in vivo* near-infrared imaging. Figure 2.3 shows no significant Cy7 signal in the control, PBS mouse. An increase in Cy7 signal was observed throughout the mice as the mole percentage of Cy7 increased in the mixed micelle formulations. The images are presented on the same radiance scale. Accumulation of Cy7 signal was only observed in the mice receiving CREKA micelles with 10 or 25 mol% Cy7 and appears in the neck region of each mouse. Evaluating the *in vivo* images each on their own radiance scale so that the highlighted regions are observed shows that mice with CREKA micelles injected with 10 mol% Cy7 have a bright region near the neck (Figure 2.4). While some signal accumulation is seen with PEG micelles, it is not as profound as the CREKA micelle accumulation.

Further analysis of the aortic trees showed an increase in Cy7 signal as the molar percentage of Cy7 increased (Figure 2.5). No statistically significant difference was calculated between the PEG and CREKA micelles at each molar percentage of Cy7 (Table 2.2).

Clearance of micelles was observed through the liver and kidney via the reticuloendothelial (RES) or renal system, respectively (Figure 2.6). A representative image of each organ is shown with 25 mol% Cy7 as this relates to the highest radiance values observed. Quantification of the radiance values in the kidney of each mole percentage of Cy7 showed a linear relationship between the average radiance values versus the mole percentage of Cy7 for both PEG and CREKA micelles (Figure 2.7). A linear trend was shown when calculating the average radiance and total flux.

Comparison of the average radiance from the kidneys of mice receiving PEG or CREKA micelles showed a statistically significant difference for two conditions, 2.5% Cy7 ($p = 0.0001$) and 25% Cy7 ($p = 0.0057$). A statistically significant difference was not observed in micelles composed of 5% Cy7 ($p = 0.15$) and 10% Cy7 ($p = 0.75$).

2.3.3 In Vivo Biocompatibility of Peptide Amphiphile Micelles

Cytotoxicity was assessed by evaluating caspase-3 activity in the liver and spleen as these two organs represent the major components of the reticuloendothelial system. For both micelle formulations, PEG and CREKA, as compared to the PBS control in both the liver and spleen, no statistically significant increase in caspase-3 activity was found (Figure 2.8).

Liver function was further assessed by measuring the alanine aminotransferase (ALT) and aspartate aminotransferase (AST) levels in homogenized tissue (Figure 2.9). No statistically significant increase in either ALT or AST levels was observed in either micelle system versus the PBS control.

Biocompatibility of PEG and CREKA micelles was additionally evaluated through H&E staining of the heart, lung, liver, spleen, intestines, kidney, and bladder. Imaging of H&E stained tissues showed no morphological or cellular changes versus images from PBS control mice (Figure 2.10). Images represent the tissue state after the micelles circulated for 24 hours *in vivo*.

2.4 Discussion

In this *in vivo* study, the biodistribution and safety of peptide amphiphile (PA) micelles was evaluated. Given the growing number of applications for PA micelles, a priori knowledge of the biocompatibility of these materials would be beneficial when considering the clinical applicability of PA micelles. Small, spherical PA micelles were therefore evaluated to determine their biodistribution and safety after 24 hours in circulation versus a PEG micelle control and compared to an injection of PBS alone. Biodistribution over a range of mole percentages of Cy7 and correspondingly a change in PEG or peptide content was determined in a mouse model of atherosclerosis, ApoE -/- mice.

The presence of small, spherical micelles using both PEG and CREKA micelles was confirmed using negative stain TEM (Figure 2.1). The hydrodynamic diameter of PEG and CREKA micelles, as determined via DLS, was close in size and each micelle system had a tight size distribution with one population of particles which is important when evaluating the effect of size on biodistribution (Figure 2.2 and Table 2.1, PEG: 9.6 ± 0.2 nm, CREKA: 13.2 ± 0.8 nm). A difference in surface charge, which is important when considering biodistribution and clearance [18], was observed between PEG (-23 ± 5 mV) and CREKA (36 ± 2 mV) micelles as determined via the zeta potential (Table 2.1). The negative surface charge of PEG micelles is likely due to the negative charge of the phosphate group. CREKA micelles were synthesized on rink amide resin, resulting in an amide group and therefore no charge at the C-terminus. Similarly, no charge contribution was expected from the N-terminus due to acetylation. Three charges would be expected from the amino acids arginine (+), glutamic acid (-), and lysine (+) at physiological pH. This would predict an overall net positive surface charge for the CREKA micelles.

Micelles were injected via the tail vein and allowed to circulate for 24 hours prior to live *in vivo* imaging. Display of a representative mouse from each group on the same radiance scale showed an increase in Cy7 signal as the Cy7 percentage per micelle increased, as expected (Figure 2.3). No significant background signal was observed from the mice receiving a PBS injection, which provides evidence that the solvent, PBS, used for injecting the micelles did not provide a background signal. When presented on the same scale, mice from the CREKA group with 10 or 25 mole percentage Cy7 had a slight accumulation in the neck region, which could potentially be due to accumulation in the lymph nodes. The region highlighted appears to be distinct from the cardiovascular region and could be due to macrophage uptake of the micelles. The lack of accumulation in the mice from the PEG group provides evidence that either PEG provides a protective coat to the micelles such that they are not uptaken via macrophages or they have yet to be uptaken and cleared via another route. This effect of accumulation in the neck region of mice in the CREKA group was prominent when imaging the mice with 10 mol% Cy7 (Figure 2.4).

Near infrared imaging of the excised aortic trees also provided information about the deposition of micelles with differing amounts of peptide and dye (Figure 2.5). No statistically significant difference was found between PEG and CREKA groups with the same mole percentage of Cy7 (Table 2.2), however, it may be possible to optimize the CREKA micelles to lead to increased binding to the aortic tree. As has been observed, an optimal amount of peptide displayed can lead to an increase in binding to a given target [27]. A statistically significant difference in deposition may be observed through the use of larger numbers of mice per group, especially at the lower amounts of Cy7.

Biodistribution was evaluated via near-infrared imaging of the excised organs. The largest signal, as determined by the relative radiance values, was observed in the liver and kidneys for both PEG and CREKA micelles (Figure 2.6), which shows clearance through both the RES (liver) and renal (kidney) systems, respectively. The cut-off for clearance through the kidney is approximately 5.5 nm [28, 29], which points to the clearance of monomers via the kidney and larger constructs, such as micelles, via the liver. No preference for clearance via the kidney was found by varying the amount of Cy7 or PEG content in the micelle formulations (Figure 2.7). A linear relationship between the average radiance and the total flux versus the mole percent of Cy7 provides evidence that the signal in the kidney is constant despite the change in micelle composition. Thus, to adversely affect the clearance of CREKA micelles, it would be necessary to use a mole percent greater than 25% of a dye-labeled monomer. Due to quenching effects, a larger mole percentage would be unlikely. In addition, by showing that kidney clearance is linearly proportional to the amount of Cy7 in each micelle and with the knowledge that most likely monomers are cleared through the kidneys, this begins to show that the stability of CREKA or PEG micelles was not significantly altered through the use of 25 mole percent of a dye-labeled monomer. A statistically significant increase in the average radiance from the kidneys was not observed in all micelle formulations using CREKA versus PEG micelles. An increase in average radiance was observed for all CREKA micelles versus the corresponding PEG counterpart, as may be expected due to the ability of PEG to increase the circulation time of nanoparticles *in vivo*. Organs from mice were only excised from two mice per group such that it was not possible to determine any statistically significant information from other excised organs.

Excised organs were used to also determine the relative safety and biocompatibility of PA micelles as compared to an injection of PBS alone. No increase in apoptosis was observed within the liver or spleen as was elucidated from caspase-3 activity (Figure 2.8). ALT and AST levels in the liver also showed good biocompatibility after a 24 hour circulation time as no statistically significant differences for either the PEG or CREKA micelle formulations was observed versus the PBS control (Figure 2.9). In addition, no morphological or cellular changes were detected in any of the organs, as was assessed via H&E staining (Figure 2.10). Each of these assays and methods of comparing PA micelles to a known, non-cytotoxic injection of PBS provides the first evidence that PA micelles do not cause harm to tissues or elicit any statistically significant change in liver or spleen function.

2.5 Conclusions

PA micelles formed from the fibrin-binding pentapeptide CREKA were evaluated for their biodistribution and safety versus both a long-circulating control micelle formed from DSPE-PEG$_{2000}$ and a PBS control. Both PEG and CREKA micelles were shown to form small, spherical micelles with differing surface change of -23 mV (PEG micelles) and 36 mV (CREKA micelles). *In vivo*, while no statistically significant differences in accumulation in the aortic tree were found between PEG and CREKA formulation, this study points at the importance of using the optimal mole percentage of each monomer in a micelle formulation. Clearance was also established through both the liver (RES) and kidney (renal) system and kidney clearance was shown to be constant despite the changes in micelle formulations. Cytotoxicity studies combined with liver function analysis via ALT and AST levels as well as histological analysis of the heart, lung, liver, spleen, intestines, kidney, and bladder showed that both PEG and CREKA micelles were non-cytotoxic *in vivo* up to 24 hours in circulation. This study shows the potential of using PA micelles *in vivo* and points to their safety as well as clearance, two aspects of material design particularly important for future biomedical applications of both CREKA micelles specifically and PA micelles in general.

2.6 Supplemental Information

2.6.1 Live In Vivo Imaging of Mice at Varying Mole Percentages of Cy7

In vivo imaging was performed as described in section 2.2.3. Direct comparison of each micelle formation was achieved by evaluating each mole percentage of Cy7 on the same radiance scale. At 2.5 mole percent Cy7, mice receiving an injection of CREKA micelles showed some accumulation in the cardiovascular and neck region, but no accumulation was seen in the mice from the PEG group (Figure 2.11). Through the use of 5 mole percent Cy7, some signal is observed in the bladder region for each micelle formulation (Figure 2.12). The largest signal for 10 mole percent Cy7 in mice from the

CREKA group was seen in the neck region (Figure 2.13, f and g). Finally, micelle formulations with 25 mole percent Cy7 showed no repeatable accumulation (Figure 2.14) as the largest signals were observed in the bladder (a and g), but also the neck region (e and g). Given the relatively large amount of Cy7 in the 25 mole percent construct and the potential for signal quenching, it would most likely be advised that this amount of Cy7 would not be used in future studies. However, to determine the optimal amount of Cy7 for any given PA system, it may be advantageous to explore a range of Cy7 amounts from 2.5 – 10 mole percent Cy7.

Figure 2.1 Transmission electron micrograph of PEG and CREKA micelles. TEM shows spherical micelles are formed by (a) PEG or (b) CREKA micelles.

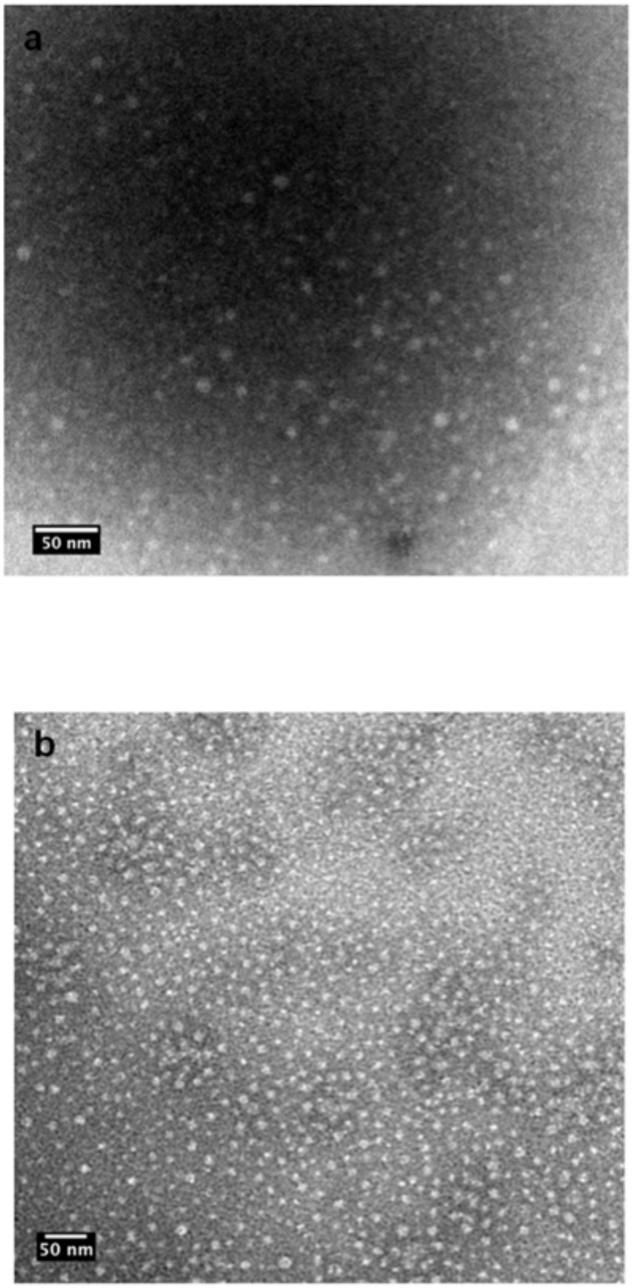

Figure 2.2 Dynamic light scattering of PEG and CREKA micelles. Dynamic light scattering of both (a) PEG and (b) CREKA micelles shows a tight size distribution of one population of micelles for each system tested.

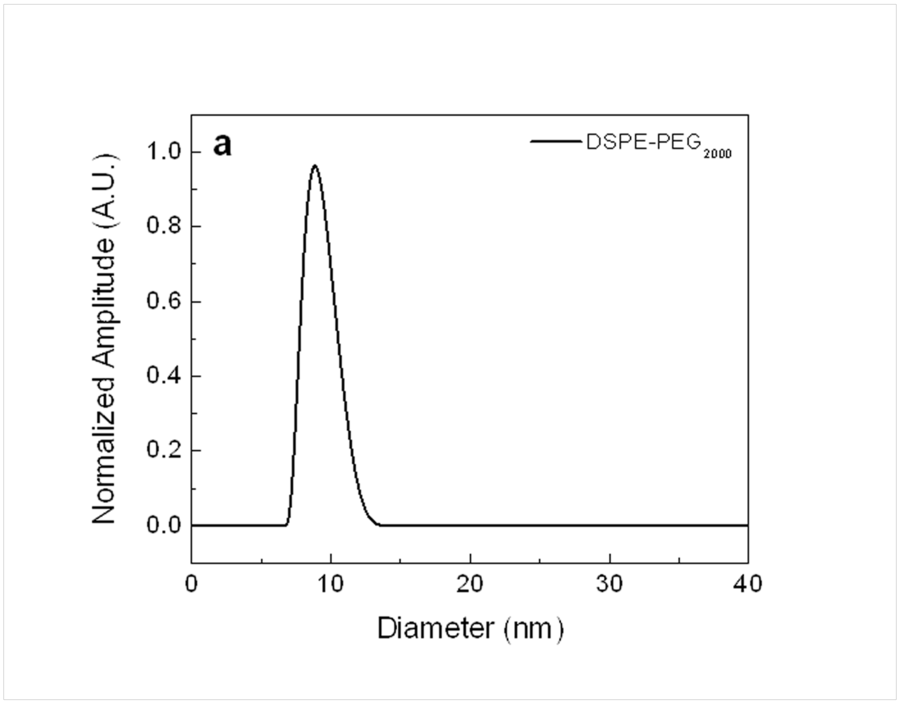

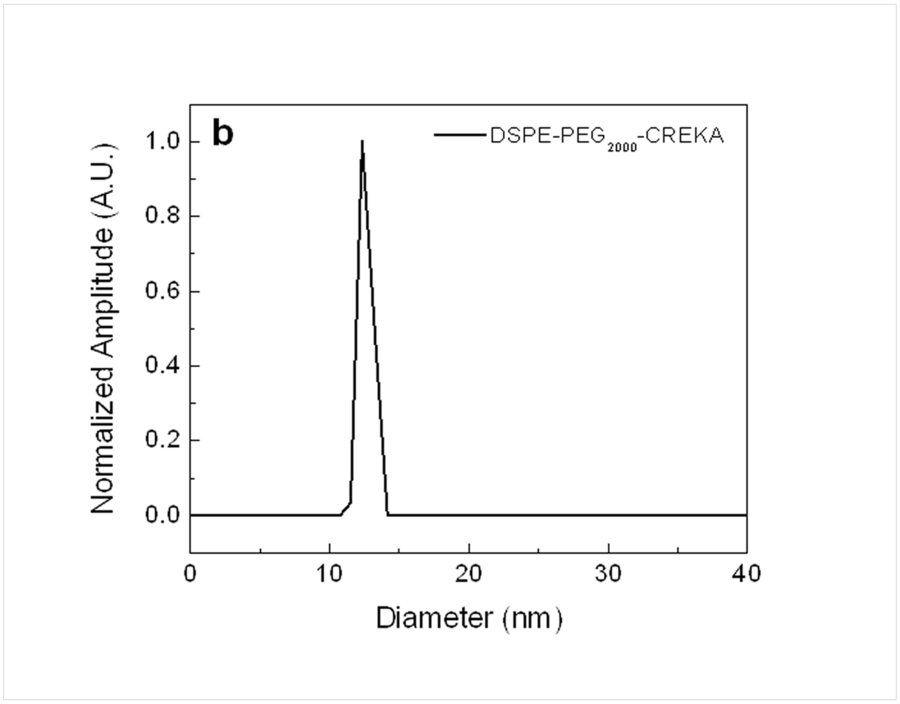

Table 2.1 Physical properties of PEG and CREKA micelles.

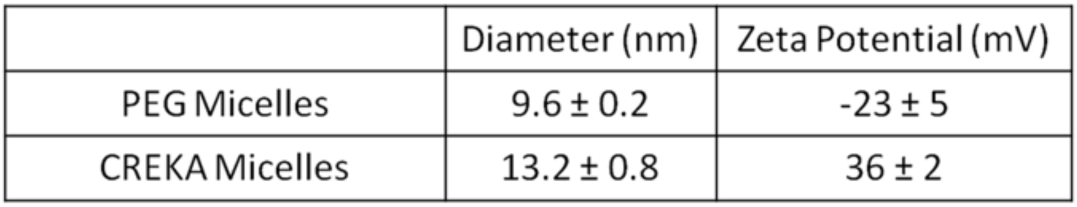

	Diameter (nm)	Zeta Potential (mV)
PEG Micelles	9.6 ± 0.2	-23 ± 5
CREKA Micelles	13.2 ± 0.8	36 ± 2

Figure 2.3 Whole body images of ApoE -/- mice using near-infrared imaging. An increase in radiance correlates with the increase in percentage of Cy7 per micelle. As a background control, mice receiving an injection of only PBS (a) presented no significant signal. The neck region begins to be highlighted in the CREKA micelles receiving 10 mol% (h) or 25 mol% (i) Cy7.

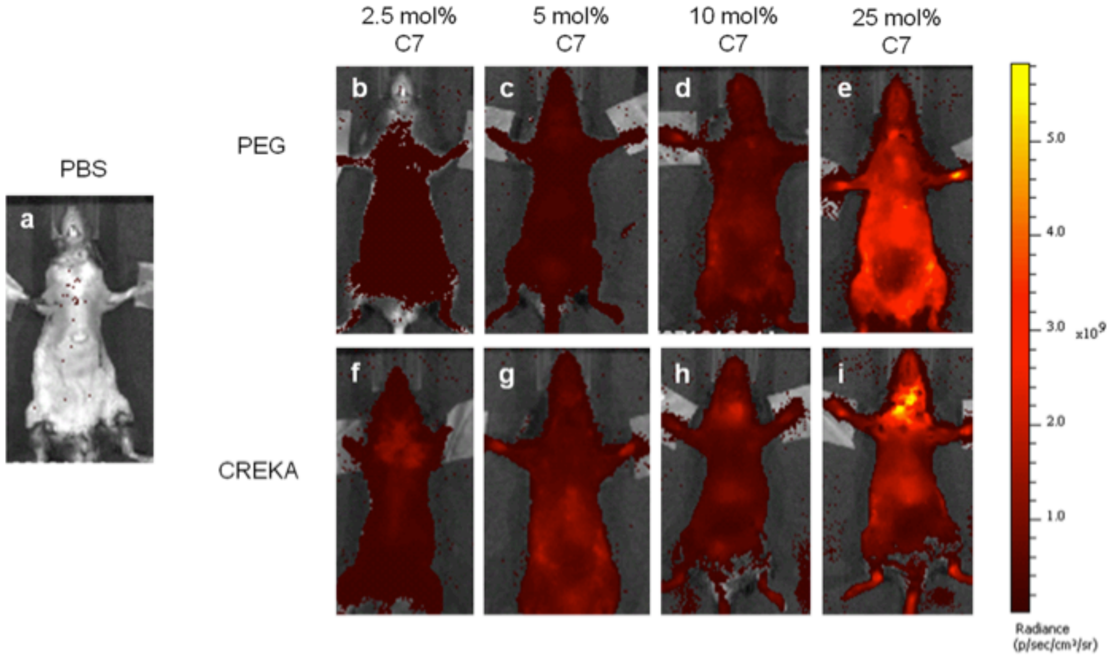

Figure 2.4 Whole body images of ApoE -/- mice with 10 mol% Cy7 using near-infrared imaging. Mice receiving PEG micelles showed no accumulation of Cy7 signal (a-c). More pronounced signal was observed in mice from the CREKA group, but does not appear in the cardiovascular region.

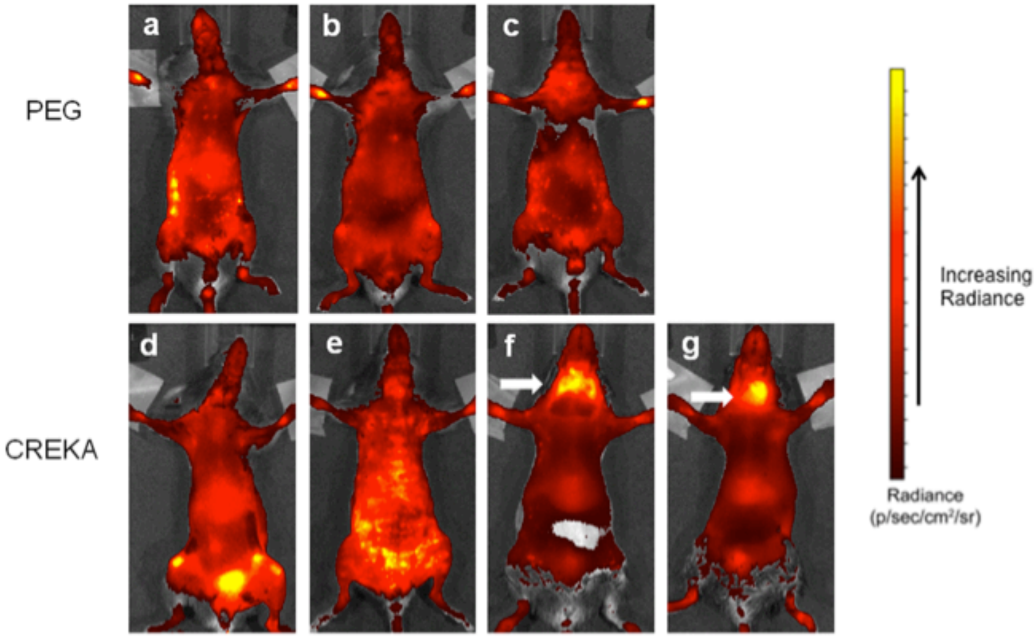

Figure 2.5 Near-infrared imaging of aortic trees. No statistically significant difference ($p > 0.1$) was calculated between radiance values from PEG and CREKA groups at each respective mol% of Cy7. An increase in Cy7 signal was observed as the mol% of Cy7 increased.

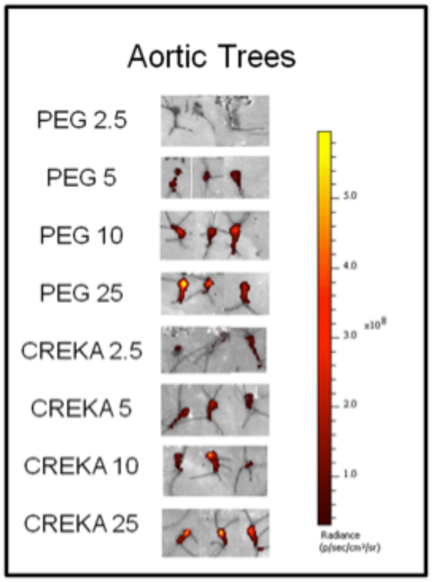

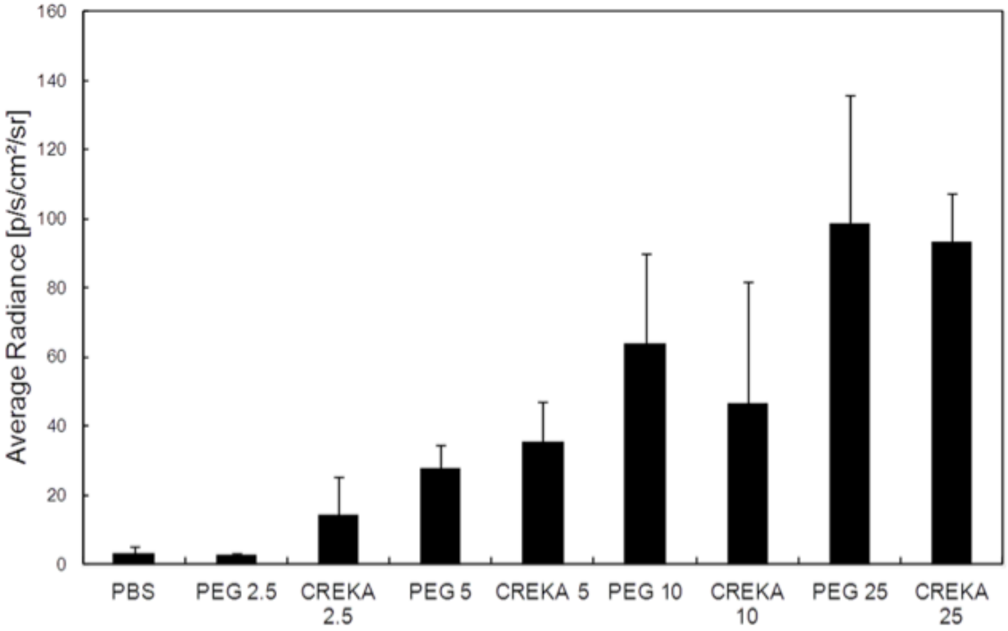

Table 2.2 Quantification of the deposition of PEG and CREKA micelles in the aortic tree.

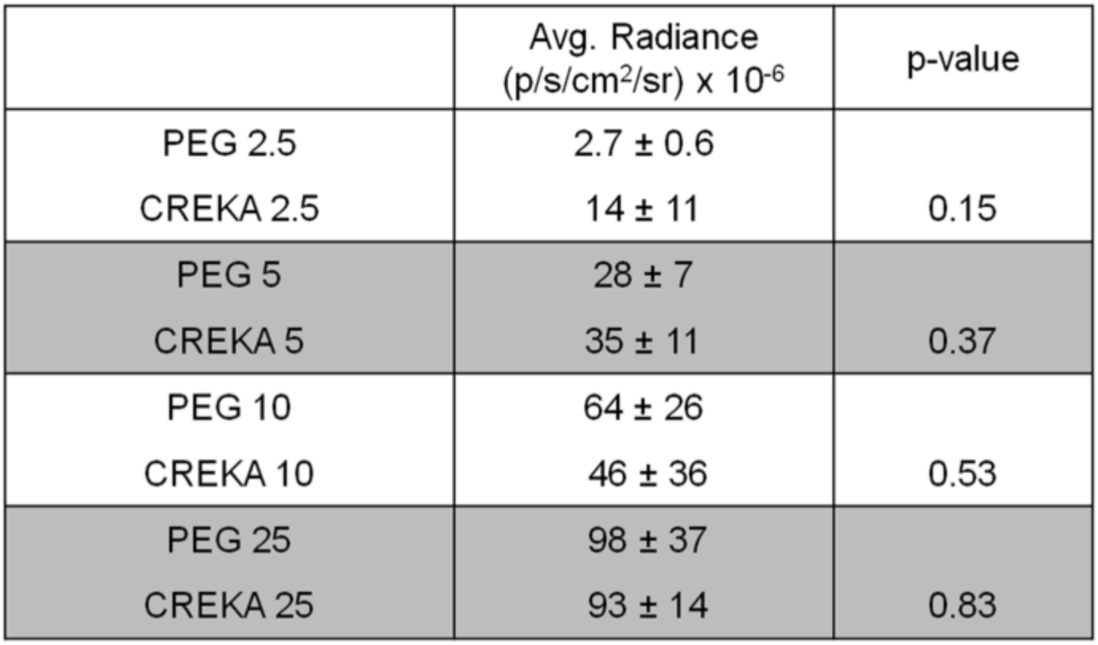

	Avg. Radiance ($p/s/cm^2/sr$) x 10^{-6}	p-value
PEG 2.5	2.7 ± 0.6	
CREKA 2.5	14 ± 11	0.15
PEG 5	28 ± 7	
CREKA 5	35 ± 11	0.37
PEG 10	64 ± 26	
CREKA 10	46 ± 36	0.53
PEG 25	98 ± 37	
CREKA 25	93 ± 14	0.83

Figure 2.6 Biodistribution of PEG and CREKA micelles after 24 hours *in vivo*. Clearance is observed through the liver (reticuloendothelial system) and kidney (renal system). A representative image using 25 mol% Cy7 is shown.

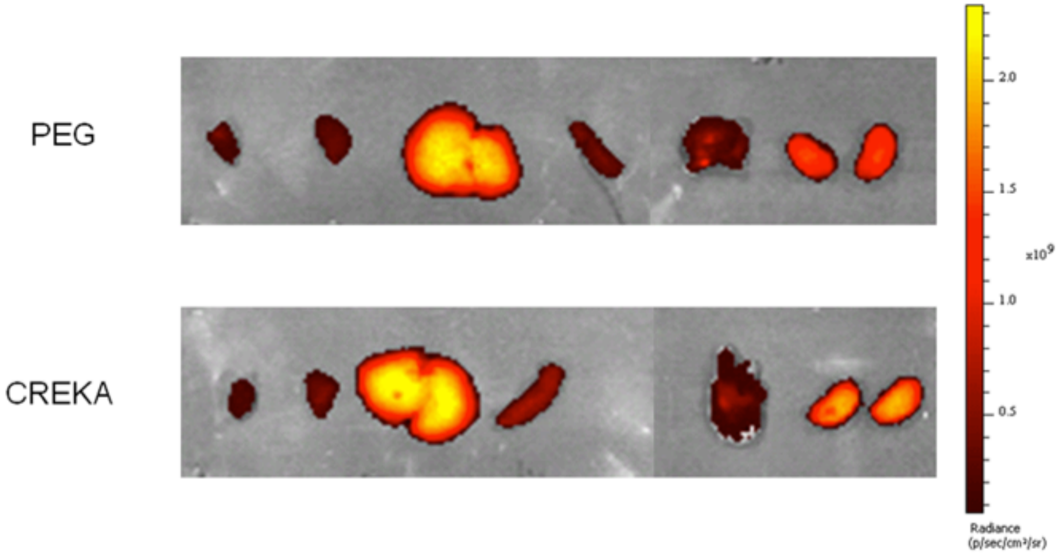

Figure 2.7 Radiance values in the kidney. The average radiance (a, c) and total flux (b, d) in the kidney was shown to be proportional to the mol% of Cy7 in the injected micelle system with both PEG and CREKA micelles.

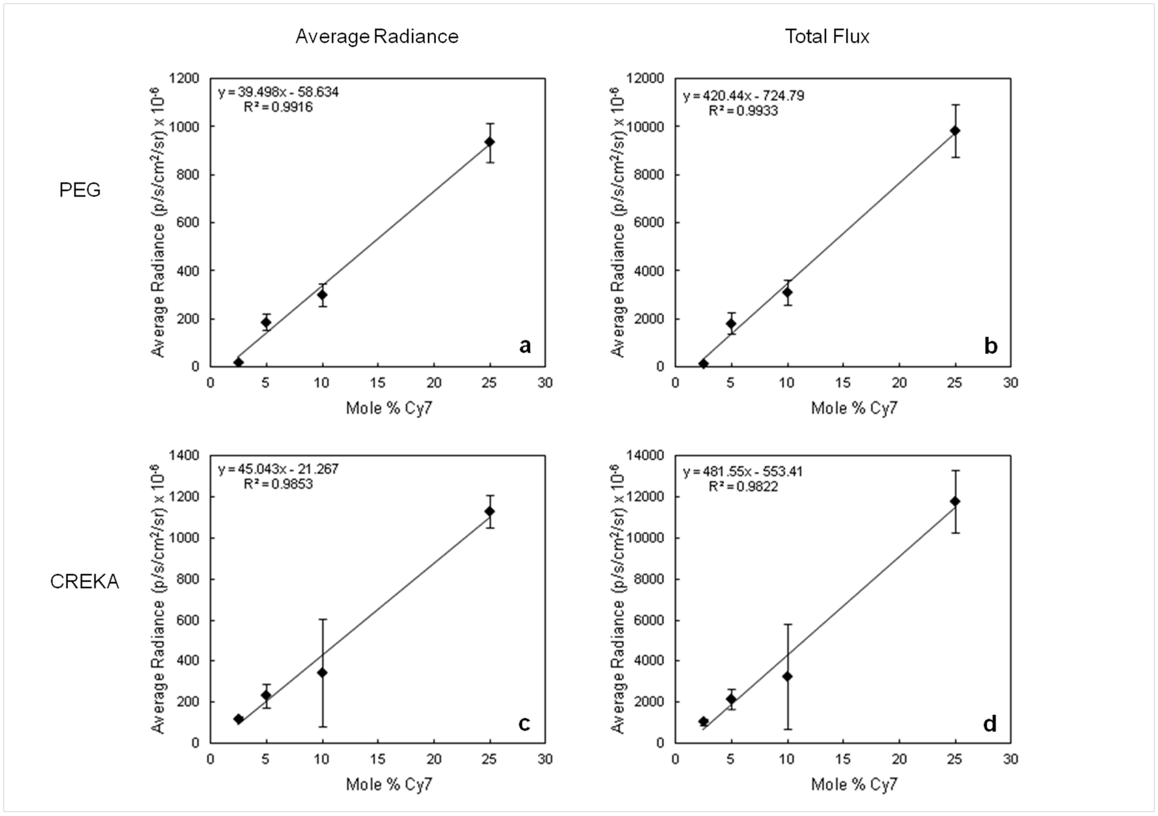

Figure 2.8 Cytotoxicity of PEG and CREKA micelles in the liver and spleen. Neither PEG nor CREKA micelles resulted in increased apoptosis in the liver (a) or spleen (b) when compared to the PBS control as shown by no statistically significant increase in caspase activity.

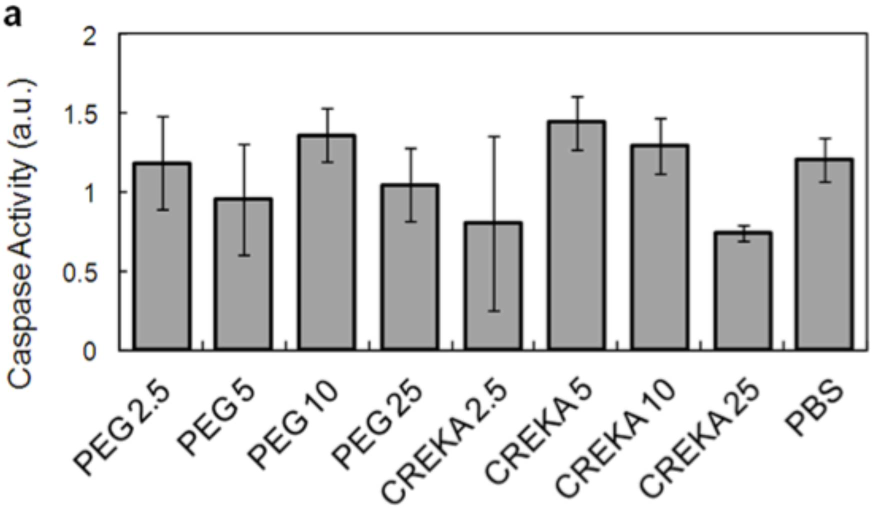

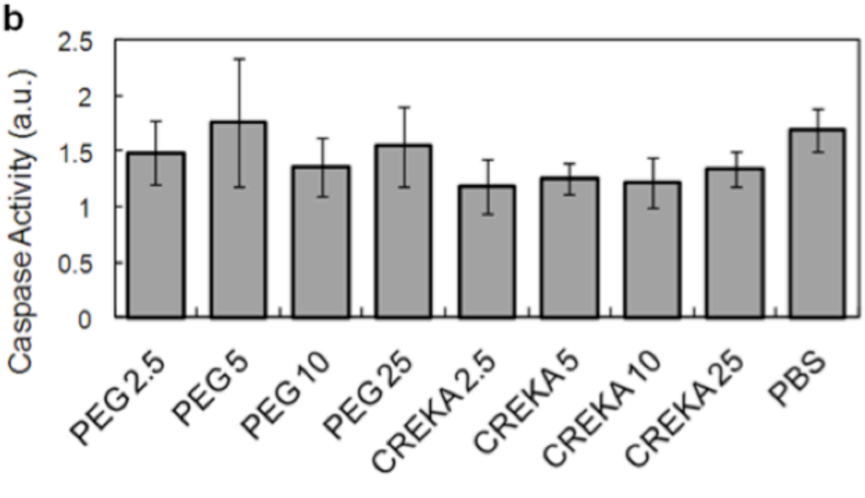

Figure 2.9 Liver function analysis. For both the alanine aminotransferase (ALT) (a) and aspartate aminotransferase (AST) (b) assay, no statistically significant change in activity was observed for any PEG or CREKA micelle group versus the PBS control.

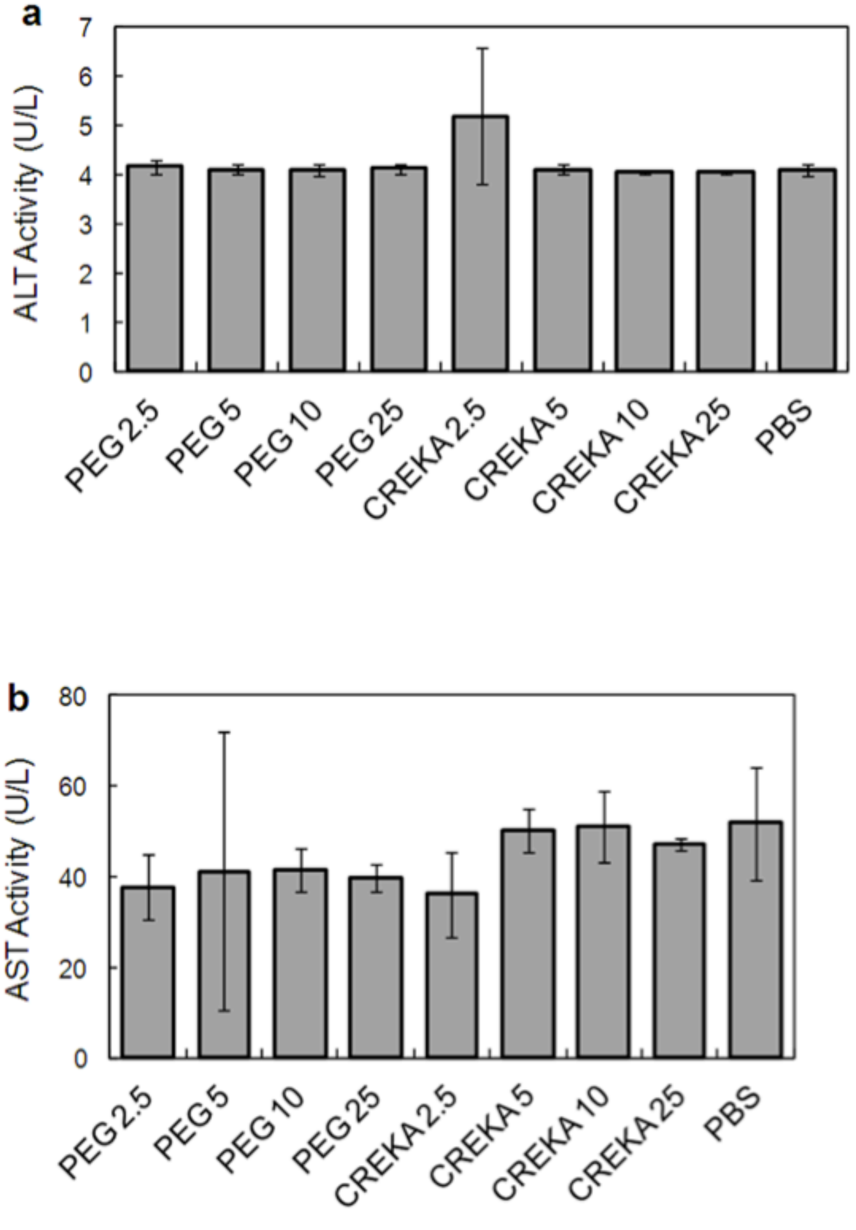

Figure 2.10 Histological analysis of tissues. No morphological or cellular changes were observed in the tissues from mice receiving PEG or CREKA micelles as compared to tissues from the PBS control.

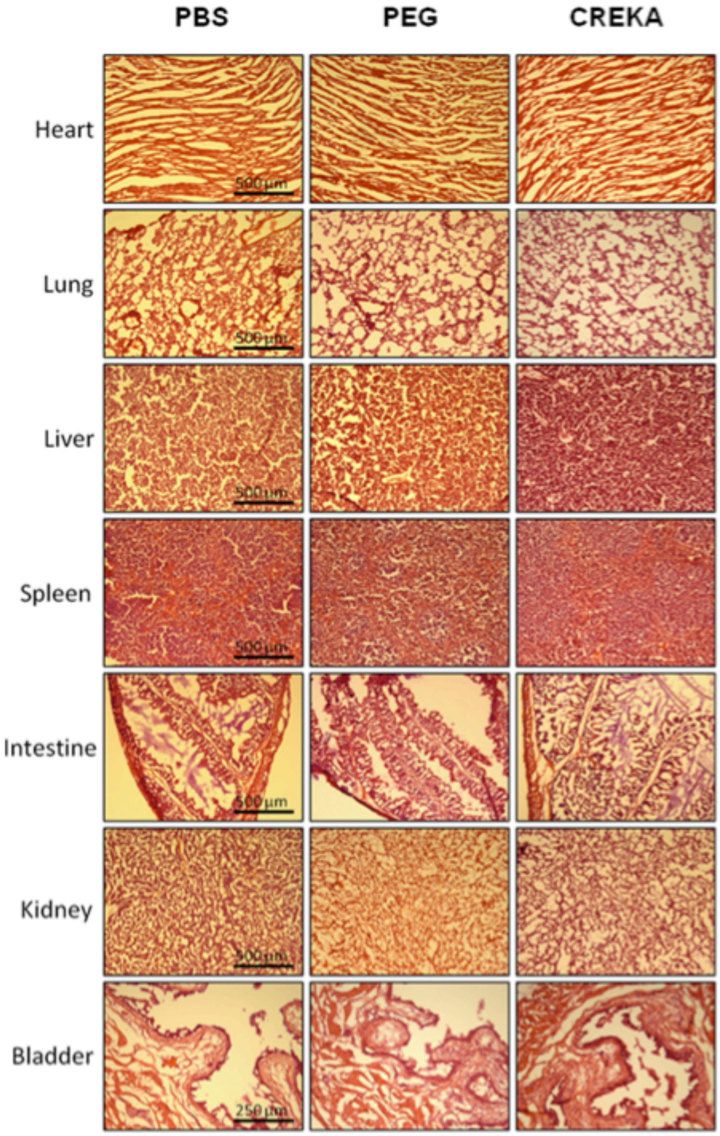

Figure 2.11 *In vivo* live imaging of mice receiving 2.5 mol% Cy7 micelles. CREKA micelles can be distinguished in the cardiovascular and neck region in one mouse (d). Cy7 signal is dispersed among the mice in all other mice receiving 2.5 mol% Cy7 micelles.

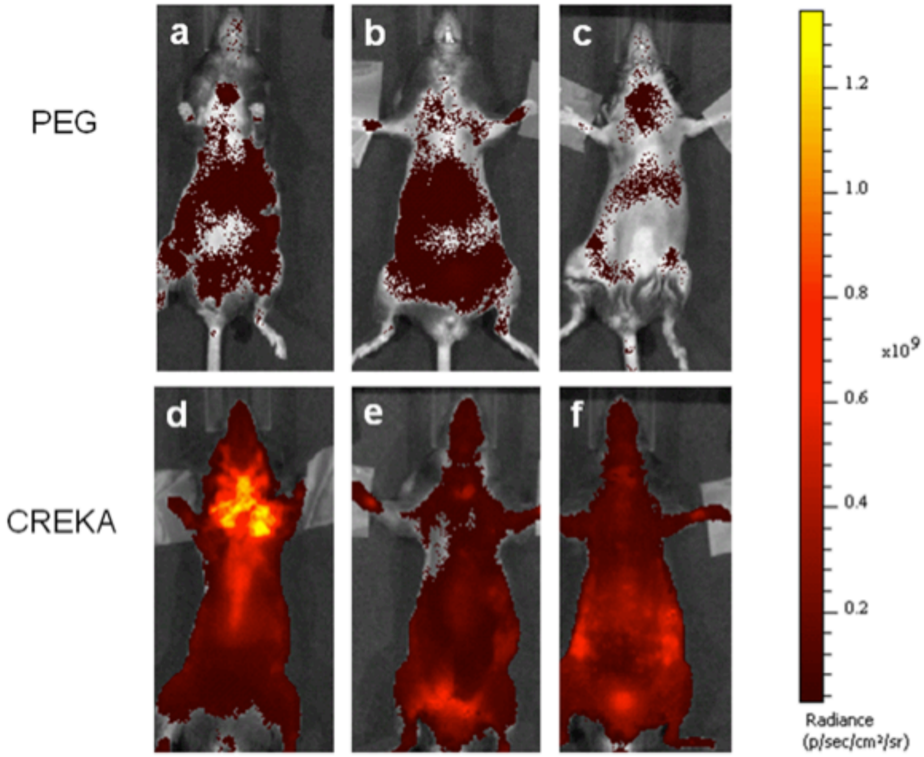

Figure 2.12 *In vivo* live imaging of mice receiving 5 mol% Cy7 micelles. Accumulation of Cy7 signal is observed in the bladder in the mice receiving 5 mol% Cy7 in a-c and d,f most prominently.

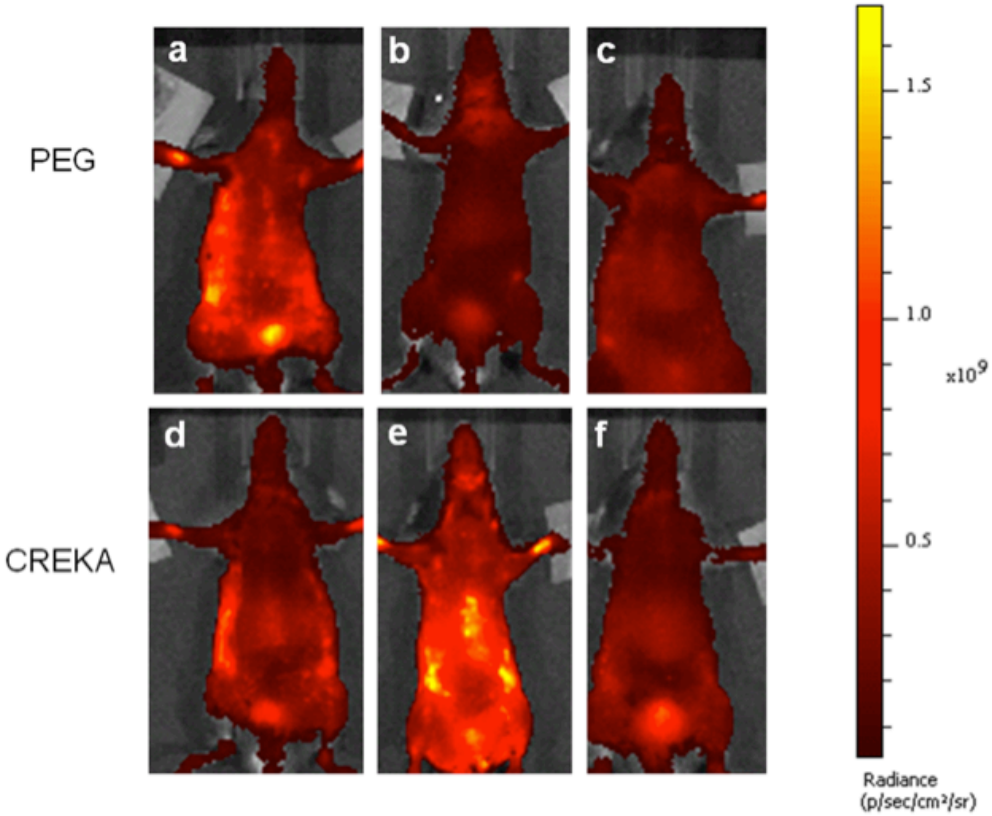

Figure 2.13 ***In vivo*** **live imaging of mice receiving 10 mol% Cy7 micelles.** CREKA micelles can be distinguished in the neck region (f, g). Cy7 signal is dispersed throughout the animal in all other mice receiving 10 mol% Cy7 micelles (PEG micelles: a-c, CREKA micelles: d, e). The images are presented on the same radiance scale.

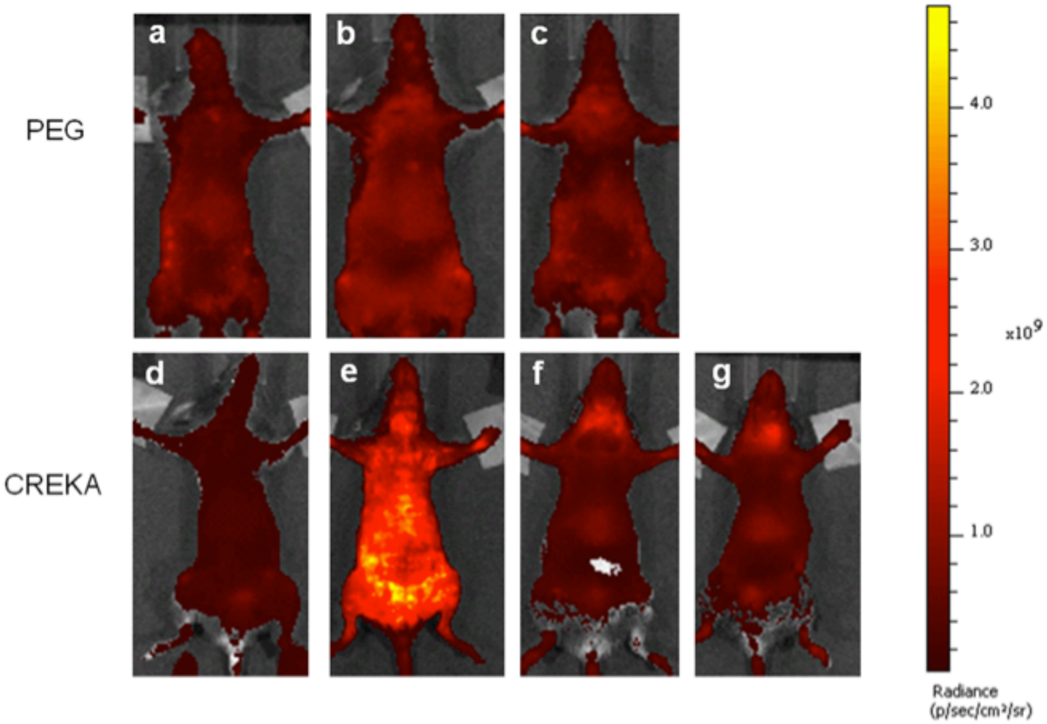

Figure 2.14 *In vivo* live imaging of mice receiving 25 mol% Cy7 micelles. No repeatable specific accumulation is observed in mice receiving PEG micelles (a-d) or CREKA micelles (e-g) at 25 mol% Cy7. The large Cy7 signal throughout the body may make it more difficult to distinguish specific accumulation.

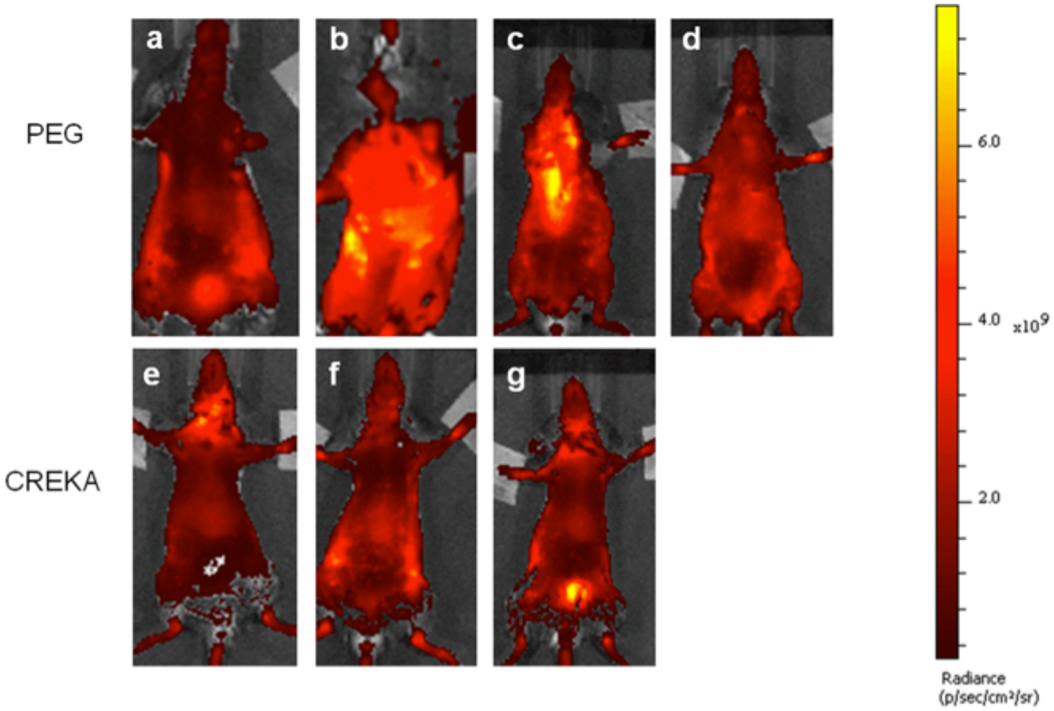

References:

[1] Lewis DR, Kamisoglu K, York AW, Moghe PV. Polymer-based therapeutics: nanoassemblies and nanoparticles for management of atherosclerosis. Wiley Interdiscip Rev Nanomed Nanobiotechnol 2011;3:400-20.

[2] Nasongkla N, Bey E, Ren J, Ai H, Khemtong C, Guthi JS, et al. Multifunctional polymeric micelles as cancer-targeted, MRI-ultrasensitive drug delivery systems. Nano Lett 2006;6:2427-30.

[3] Peters D, Kastantin M, Kotamraju VR, Karmali PP, Gujraty K, Tirrell M, et al. Targeting atherosclerosis by using modular, multifunctional micelles. Proc Natl Acad Sci U S A 2009;106:9815-9.

[4] McCarthy JR, Weissleder R. Multifunctional magnetic nanoparticles for targeted imaging and therapy. Adv Drug Deliv Rev 2008;60:1241-51.

[5] Schiener M, Hossann M, Viola JR, Ortega-Gomez A, Weber C, Lauber K, et al. Nanomedicine-based strategies for treatment of atherosclerosis. Trends Mol Med 2014;20:271-81.

[6] Lien S, Lowman HB. Therapeutic peptides. Trends Biotechnol 2003;21:556-62.

[7] Thapa N, Hong HY, Sangeetha P, Kim IS, Yoo J, Rhee K, et al. Identification of a peptide ligand recognizing dysfunctional endothelial cells for targeting atherosclerosis. J Control Release 2008;131:27-33.

[8] Burtea C, Laurent S, Port M, Lancelot E, Ballet S, Rousseaux O, et al. Magnetic resonance molecular imaging of vascular cell adhesion molecule-1 expression in inflammatory lesions using a peptide-vectorized paramagnetic imaging probe. J Med Chem 2009;52:4725-42.

[9] Berndt P, Fields GB, Tirrell M. Synthetic lipidation of peptides and amino acids: monolayer structure and properties. J Am Chem Soc 1995;117:9515-22.

[10] Chung EJ, Cheng Y, Morshed R, Nord K, Han Y, Wegscheid ML, et al. Fibrin-binding, peptide amphiphile micelles for targeting glioblastoma. Biomaterials 2014;35:1249-56.

[11] Missirlis D, Khant H, Tirrell M. Mechanisms of peptide amphiphile internalization by SJSA-1 cells in vitro. Biochemistry 2009;48:3304-14.

[12] Missirlis D, Krogstad DV, Tirrell M. Internalization of p53(14-29) peptide amphiphiles and subsequent endosomal disruption results in SJSA-1 cell death. Mol Pharm 2010;7:2173-84.

[13] Niece KL, Hartgerink JD, Donners JJ, Stupp SI. Self-assembly combining two bioactive peptide-amphiphile molecules into nanofibers by electrostatic attraction. J Am Chem Soc 2003;125:7146-7.

[14] Lin BF, Megley KA, Viswanathan N, Krogstad DV, Drews LB, Kade MJ, et al. pH-responsive branched peptide amphiphile hydrogel designed for applications in regenerative medicine with potential as injectable tissue scaffolds. J Mater Chem 2012;22:19447-54.

[15] Webber MJ, Tongers J, Newcomb CJ, Marquardt KT, Bauersachs J, Losordo DW, et al. Supramolecular nanostructures that mimic VEGF as a strategy for ischemic tissue repair. Proc Natl Acad Sci U S A 2011;108:13438-43.

[16] Hamley IW. PEG-peptide conjugates. Biomacromolecules 2014;15:1543-59.

[17] Lukyanov AN, Gao Z, Mazzola L, Torchilin VP. Polyethylene glycol-diacyllipid micelles demonstrate increased acculumation in subcutaneous tumors in mice. Pharm Res 2002;19:1424-9.
[18] Duan X, Li Y. Physicochemical characteristics of nanoparticles affect circulation, biodistribution, cellular internalization, and trafficking. Small 2013;9:1521-32.
[19] Stolnik S, Illum L, Davis SS. Long circulating microparticulate drug carriers. Adv Drug Deliv Rev 1995;16:195-214.
[20] Alexis F, Pridgen E, Molnar LK, Farokhzad OC. Factors affecting the clearance and biodistribution of polymeric nanoparticles. Mol Pharm 2008;5:505-15.
[21] Roser M, Fischer D, Kissel T. Surface-modified biodegradable albumin nano- and microspheres. II: effect of surface charges on in vitro phagocytosis and biodistribution in rats. Eur J Pharm Biopharm 1998;46:255-63.
[22] Champion JA, Katare YK, Mitragotri S. Particle shape: a new design parameter for micro- and nanoscale drug delivery carriers. J Control Release. 2007;121:3-9.
[23] Champion JA, Walker A, Mitragotri S. Role of particle size in phagocytosis of polymeric microspheres. Pharm Res 2008;25:1815-21.
[24] Knorr R, Trzeciak A, Bannwarth W, Gillessen D. New coupling reagents in peptide chemistry. Tetrahedron Lett 1989;30:1927-30.
[25] Fields GB, Noble RL. Solid phase peptide synthesis utilizing 9-fluorenylmethoxycarbonyl amino acids. Int J Pept Protein Res 1990;35:161-214.
[26] Whitman SC. A practical approach to using mice in atherosclerosis research. Clin Biochem Rev 2004;25:81-93.
[27] Kusunose J, Zhang H, Gagnon MK, Pan T, Simon SI, Ferrara KW. Microfluidic system for facilitated quantification of nanoparticle accumulation to cells under laminar flow. Ann Biomed Eng 2013;41:89-99.
[28] Choi HS, Liu W, Misra P, Tanaka E, Zimmer JP, Ipe BI, et al. Renal clearance of quantum dots. Nat Biotechnol 2007;25:1165-70.
[29] Rao J. Shedding light on tumors using nanoparticles. ACS Nano 2008;2:1984-6.

Chapter 3

Active Targeting of Early and Mid-Stage Atherosclerotic Plaques using Self-Assembled Peptide Amphiphile Micelles

Abstract

Inflammatory cell adhesion molecules expressed by endothelial cells on the luminal surface of atherosclerotic plaques, such as vascular cell adhesion molecule-1 (VCAM-1), provide a rational target for diagnostic and therapeutic delivery vehicles. Therefore, the potential of using spherical, self-assembled micelles synthesized from VCAM-1 targeted peptide amphiphile molecules was examined for the ability to specifically bind to both early and mid-stage atherosclerotic plaques. *In vitro*, cells incubated with VCAM-1 targeted and dye labeled micelles show enhanced fluorescence signal as compared to cells incubated with a PEG micelle control. *In vivo*, VCAM-1 targeted and Cy7 labeled peptide amphiphile micelles were shown to specifically accumulate at atherosclerotic plaques in both early and mid-stage ApoE -/- mice through co-localization of Cy7 signal with anti-VCAM-1 antibody staining in fixed tissue. No specific accumulation was observed with a PEG micelle control. Histological analysis of excised tissue provided evidence for the *in vivo* biocompatibility of these micelle formulations as no tissue damage was observed. These results demonstrate that VCAM-1 targeted micelles have potential as a platform for targeted drug delivery to multiple stages of atherosclerotic plaque formation due to their established specificity and safety.

3.1 Introduction

Cardiovascular disease leads to nearly one-third of deaths annually in the United States according to The American Heart Association [1]. Atherosclerosis, characterized by the formation of arterial wall plaques, is widely accepted as a main cause of cardiovascular disease [2]. Atherosclerotic plaque formation develops over the course of decades and progresses through multiple stages from lipid accumulation in the artery wall which leads to a cascade of inflammatory responses, growth of the lipid core, and eventual fibrous cap formation. Inflammation plays a large role in the development of plaques and key inflammatory markers have been identified to selectively target plaques [2-4]. Clinically speaking, late-stage vulnerable plaques, typically signified by a thinning fibrous cap, require the greatest immediate attention as these plaques are the most likely to cause imminent danger to the patient [5]. From a diagnostic standpoint, however, establishing a method to identify atherosclerotic plaques at an earlier stage could provide a means to treat these plaques prior to a catastrophic event such as myocardial infarction.

Multiple inflammatory markers have been interrogated for their ability to identify plaques [2, 4]. Inflammatory markers of atherosclerosis provide a target for drug delivery vehicles due to their overexpression and specificity, as well as providing a means to directly deliver a potential anti-inflammatory therapeutic. One of the most prominent markers of early stage atherosclerotic plaques is vascular cell adhesion molecule-1 (VCAM-1), which is expressed by endothelial cells that line the developing plaque [2, 6-

8]. VCAM-1 expression at the site of plaque development is not limited to mouse models of atherosclerosis, but is also observed as a marker of human atherosclerotic plaques [9, 10]. Overexpression of VCAM-1 has also been shown to be limited to regions of plaque development in the aorta and has been identified as an early marker of regions of the aorta prone to lesion formation [2, 11], making its targeting specificity ideal for drug delivery vehicles to accumulate at atherosclerotic plaques. VCAM-1 targeting has previously been shown to successfully enhance the delivery of MRI and SPECT contrast agents to plaques for imaging of varying stages of atherosclerotic plaque formation [6, 12-15], however, such targeting has yet to be shown using micellar nanoparticles capable of delivering a payload to the plaque.

Micelles provide a platform for drug delivery due to their ability to carry hydrophobic or weakly soluble drugs in their hydrophobic core [16, 17] or hydrophilic drugs as part of the hydrophilic corona [18]. Peptide amphiphiles formed by conjugating a hydrophobic tail to a hydrophilic peptide head group [19] self-assemble into peptide amphiphile micelles in aqueous solutions above the critical micelle concentration (CMC). By incorporating a targeting peptide in the hydrophilic corona, the applicability of the micelle platform is enhanced. The modular nature of peptide amphiphile micelles provides a facile means of incorporating a variety of monomers that allow for both targeting and imaging of atherosclerotic plaques. Peptide amphiphile micelles also confer certain advantages such as forming nanoparticles with a micromolar CMC and a hydrodynamic diameter large enough to avoid renal clearance [4]. Moreover, peptides have distinct advantages over the use of whole proteins, namely, their shorter structure curtails certain immune responses and increased tissue penetration is observed using peptides due to their smaller size [14, 20, 21].

Here, we present a peptide amphiphile micelle targeted to VCAM-1 expression in both early and mid-stage atherosclerotic plaques. The VCAM-1 targeting peptide used has been shown to be homologous to very late antigen-4 (VLA-4) [22], which is expressed by monocytes, lymphocytes, and eosinophils [23] and binds to VCAM-1, displayed at the endothelial cell surface. VCAM-1 targeted micelles labeled with a near-infrared dye, Cy7, were intravenously injected into ApoE -/- mice to compare their deposition in the aortic tree of mice with early and mid-stage atherosclerotic plaques. It is hypothesized that the targeting peptide will direct VCAM-1 targeted micelles to sites of VCAM-1 expression throughout the aortic tree and therefore lead to an increase in binding versus the passive PEG micelle control.

3.2 Materials and Methods

3.2.1 Synthesis and Purification of Peptide Amphiphiles

Peptides were purchased fully protected on rink amide resin from ChinaTech Peptide (Suzhou, China) and were synthesized using standard Fmoc solid phase peptide synthesis [19, 24, 25]. The VCAM-1 binding sequence was modified with an N-terminal cysteine (sequence: CVHPKQHR) to allow for conjugation to a maleimide-containing hydrophobic tail. The N-terminus was acetylated using acetic anhydride following Fmoc deprotection. Complete deprotection and cleavage from the resin was achieved using a trifluoroacetic acid (TFA):triisopropylsilane:water:1,2-ethanedithiol (94:1:2.5:2.5) solution. The resulting product was precipitated in cold diethyl ether prior to purification.

Purified peptide was conjugated to 1,2-distearoyl-sn-glycero-3-phosphoethanolamine-N-[maleimide(polyethylene glycol)-2000] (DSPE-PEG$_{2000}$-maleimide) (Avanti Polar Lipids, Alabaster, AL) in water using a 10% molar excess of peptide and allowed to shake overnight at room temperature. The pH of the solution was maintained between 6.5-7.5 using dilute sodium hydroxide. Peptides and peptide amphiphiles (PAs) were purified using reverse phase high performance liquid chromatography (HPLC, Prominence, Shimadzu Corporation, Kyoto, Japan) with a C_8 or C_4 Waters column (Waters Corporation, Milford, MA), respectively. Product identity was confirmed using matrix-assisted laser desorption/ionization (MALDI) mass spectrometry (Voyager DE Pro, Applied Biosystems, Life Technologies, Carlsbad, CA). The final concentration of PA in solution was determined using amino acid analysis (Molecular Structure Facility, UC Davis, Davis, CA). To form DSPE-PEG$_{2000}$-Cy7, an N-hydroxysuccinimide (NHS) ester Cyanine 7 (Cy7) dye (GE Healthcare, Buckinghamshire, England) was reacted with 10% molar excess DSPE-PEG$_{2000}$-amine (Avanti Polar Lipids, Alabaster, AL) in 10 mM sodium carbonate buffer (pH: 8.5) with 10% methanol by volume overnight. The resulting product was purified as described above on a C_4 column.

3.2.2. Micelle Formation

To form micelles, pure PA was lyophilized and dissolved in methanol. A methanol film was then formed in a glass vial by evaporating the methanol. Films were dried under vacuum overnight and subsequently rehydrated in the desired solution, vortexed to dissolve the PA, and allowed to sit at room temperature for a minimum of three hours.

3.2.3. Micelle Characterization

Micelle size and shape were determined via two methods. Micelle size was confirmed with 200 μM micelle solutions using a single angle Viscotek 802 DLS (Malvern Instruments, Malvern, UK). Hydrodynamic radii were determined via the Stokes-Einstein equation using the diffusion coefficient determined from the auto correlation function. Transmission electron microscopy (TEM) was performed at an accelerating voltage of 120 kV using a FEI Tecnai 12 TEM. PA micelle solutions were prepared at 200 μM in water. Ultrathin carbon type-A 400 mesh copper grids were loaded with 1 μL of sample and allowed to nearly dry. Samples were blotted with water to remove salts and then negatively stained with 1 μL of a 1% phosphotungstic acid in water solution. Grids were allowed to dry for 2 minutes followed by the removal of excess solution.

The critical micelle concentration (CMC) was determined using the DPH (1,6-diphenyl-1,3,5-hexatriene) fluorescence method [26]. DPH uptake into the hydrophobic micelle core yields an increase in fluorescence above the CMC. Below the CMC, DPH fluorescence is constant. DPH was dissolved in tetrahydrofuran (THF, Sigma-Aldrich, St. Louis, MO) and added to water to form a 1 μM DPH in water solution, with a final concentration of 0.1% THF. PA films were allowed to completely dry under vacuum overnight and were subsequently rehydrated in the DPH water solution described above to form a 1 mM stock solution. The stock solution was serially diluted to form working concentrations for the CMC measurement. Peptide amphiphile concentrations ranged from 316 μM to 0.001 μM. Solutions were allowed to equilibrate for 1 hour prior to measurement using a Tecan Infinite 200 plate reader (ex. 350 nm, em. 428 nm).

Circular dichroism was conducted using 200 μM peptide or PA solutions in water at 20°C with a Jasco J-815 Circular Dichroism Spectropolarimeter. A quartz cuvette with a 0.1 cm pathlength was used and scans were recorded from 250 nm to 190 nm. Curves reported are averaged from three scans. CD spectra were fit using a linear combination of polylysine basis spectra [27].

3.2.4 In Vitro Viability and Cell Binding

Human umbilical vein endothelial cells (HUVEC, Lonza Group Ltd, Basel, Switzerland) and murine aortic endothelial cells (mAEC, Cell Biologics, Chicago, IL) were used to assess cell viability *in vitro*. All cell studies were completed with cells from passages 3-5 and grown using mouse endothelial cell media (EGM-2, Lonza Group, Ltd, Basel, Switzerland and M1168, Cell Biologics, Chicago, IL, respectively) at 37°C and 5% CO_2. To determine cell viability, 5,000 cells/well were allowed to attach to a 96 well plate overnight, followed by incubation with 1-100 μM peptide or peptide amphiphile in 20% 1X PBS suspended in media. Control cells received 20% 1X PBS in media only. Cells were incubated with peptide or PA for 24 hours. Viability was determined using the presto blue assay (Invitrogen, Life Technologies, Carlsbad, CA) and read using a plate reader (ex. 560 nm, em. 590 nm, Infinite 200 Pro, Tecan Group Ltd., Mannedorf, Switzerland).

To determine the *in vitro* specificity of VCAM-1 targeted PAs, mAECs were passed onto 12-well plates and allowed to attach and spread overnight. Cells were incubated with 100 μM solutions containing 10% 1X PBS in media for 3 hours. PA solutions were composed of 90:10 mol% DSPE-PEG$_{2000}$-VCAM: DSPE-PEG$_{2000}$-Cy7. Control solutions contained only DSPE-PEG$_{2000}$-Cy7 or 90:10 mol% DSPE-PEG$_{2000}$-maleimide: DSPE-PEG$_{2000}$-Cy7. Cells were fixed with 10% formalin (Thermo Fisher Scientific, Waltham, MA) at room temperature for 10 min. Nuclei were stained with Hoechst 33342 (Invitrogen, Life Technologies, Carlsbad, CA) at 2 μg/mL for 10 min at room temperature and subsequently imaged (DMI6000 B, Leica Microsystems GmbH).

3.2.5 In Vivo Injections and Imaging

Transgenic, female, 4 week old mice homozygous for the *Apoe*^{tm1Unc} mutation (The Jackson Laboratory, Bar Harbor, ME) were fed a 42% by fat diet (Harlan TD.88137, Indianapolis, IN) for 10 weeks or 16 weeks to generate stage II or IV lesions, respectively [28]. Mice were housed at the University of Chicago and all procedures were approved by the University of Chicago's Institutional Animal Care and Use Committee (Chicago, IL). In order to image the mice, they were first shaved, followed by an application of Nair to remove any residual fur. The tail vein was dilated and sterilized with 70% ethanol prior to injection with 100 μL of a 1 mM solution. Injected solutions contained 90:10 mol% DSPE-PEG$_{2000}$-VCAM: DSPE-PEG$_{2000}$-Cy7 suspended in 1X PBS, 90:10 mol% DSPE-PEG$_{2000}$-maleimide: DSPE-PEG$_{2000}$-Cy7 suspended in 1X PBS, or 1X PBS ($N \geq 3$). After allowing micelles to circulate for 24 hours, mice were anesthetized with 2.5% isoflurane in O_2, and imaged (IVIS 200, Xenogen, PerkinElmer, Waltham, MA). Following injection, mice were euthanized via CO_2 overdose and the aortic tree as well as organs were harvested for further analysis. Organs were then imaged and Cy7 fluorescence signal was quantified using the Living Image software developed by PerkinElmer. Average radiance was used to quantify micelle deposition in the aortic tree to account for variation in sizes.

3.2.6 Histology and Immunohistochemistry

Organs were fixed overnight using 4% paraformaldehyde at 4°C. Following fixation, each tissue was submerged in a 30% sucrose solution and allowed to incubate for 8 hours. Finally, the tissue samples were embedded in OCT (Tissue Tek, Sakura Finetek, Torrance, CA) and stored frozen at -80°C. Tissue samples were cryosectioned using a Microm HM 505 E (MICROM International GmbH, Walldorf, Germany) cryomicrotome to a thickness of 5-10 μm. Further processing of the tissue sections was completed through hematoxylin and eosin staining or anti-VCAM-1 Ab staining (Santa Cruz Biotechnology, Dallas, TX). Following staining, sections were imaged using a DMI6000 B Leica Microsystems (Wetzlar, Germany) microscope.

3.3 Results

3.3.1 Micelle Characterization

Incorporation of cysteine into the N-terminus of the VCAM-1 binding peptide, VHPKQHR, allowed for conjugation of the peptide to a maleimide-containing hydrophobic tail via a thioether linkage forming DSPE-PEG$_{2000}$-CVHPKQHR (Figure 3.1). Peptide amphiphile monomers were self-assembled into small, spherical micelles as shown by negative stain transmission electron microscopy (TEM). VCAM-1 targeting micelles formed from DSPE-PEG$_{2000}$-CVHPKQHR amphiphiles were found to have a hydrodynamic diameter of 17 ± 2 nm using both TEM and dynamic light scattering (DLS) (Figure 3.1). PEG micelles were also shown to be spherical with a hydrodynamic diameter of 9.6 ± 0.2 nm as determined via DLS (Figure 3.3). The critical micelle concentration, CMC, was calculated using the DPH method. The CMC was determined to be 14 μM for VCAM micelles and 17 μM for PEG micelles formed from DSPE-PEG$_{2000}$-maleimide (Figure 3.2 and 3.3, respectively). In order to compare the function of VCAM-1 targeting peptide to VCAM-1 targeting PAs, it was necessary to show that similar secondary structure was maintained in each structure. Circular dichroism (CD) confirms that the secondary structure is primarily random coil in each case, between the VCAM-1 peptide (33% beta sheet, 67% random coil) and VCAM-1 PA micelle (28% beta sheet, 72% random coil) (Figure 3.2 and Table 3.1).

3.3.2 Biocompatibility and Targeting Ability of VCAM-1 Micelles In Vitro

In vitro biocompatibility of both the VCAM-1 targeting peptide and VCAM-1 targeting PAs was measured. Greater than 80% cell viability was observed in both murine aortic endothelial cells (mAEC) as well as human umbilical vein endothelial cells (HUVEC) up to a concentration of 100 μM of VCAM-1 targeting peptide or PA after a 24 hour incubation time (Figure 3.4). Cell viability was assessed as compared to a PBS control.

The ability to enhance uptake and binding to endothelial cells using VCAM-1 targeting PAs was determined using mAECs. As observed in Figure 3.5, mAECs incubated with 90:10 mol% DSPE-PEG$_{2000}$-VCAM:DSPE-PEG$_{2000}$-Cy7 mixed micelles show increased Cy7 signal when compared to controls containing either 90:10 mol% DSPE-PEG$_{2000}$-maleimide: DSPE-PEG$_{2000}$-Cy7 mixed micelles or DSPE-PEG$_{2000}$-Cy7 alone. Quantification via ImageJ showed an average two-fold increase in Cy7 signal in cells receiving VCAM-1 targeted micelles versus PEG micelles and a six-fold increase versus cells incubated with Cy7 monomers alone (Figure 3.6).

3.3.3 In Vivo Studies

100 μL of a 1 mM solution of 90:10 mol% DSPE-PEG$_{2000}$-VCAM:DSPE-PEG$_{2000}$-Cy7 (actively targeting micelles) or 90:10 mol% DSPE-PEG$_{2000}$: DSPE-PEG$_{2000}$-Cy7 (control micelles) was injected via the tail vein into ApoE -/- mice. Cy7 incorporation allowed for near-infrared imaging of the micelles *in vivo*. *In vivo* imaging of early stage atherosclerotic mice revealed targeting to the cardiovascular system in mice receiving VCAM-1 targeting micelles after 24 hours (Figure 3.7). In mice that received an injection of PEG passive control micelles, near-infrared live imaging shows accumulation in the bladder and liver regions (Figure 3.7). Mid-stage ApoE -/- mice receiving either VCAM-1 targeting or PEG micelles confirmed accumulation of Cy7 signal in the bladder and liver via *in vivo* imaging (Figure 3.7).

Increased deposition in both early and mid-stage aortic trees from ApoE -/- mice was observed using VCAM-1 targeted micelles versus passive control PEG micelles (Figure 3.8). Immunohistochemistry of excised aortic trees, using anti-VCAM-1 antibody, showed VCAM-1 expression in both the endothelium as well as the adventitia in early stage ApoE -/- mice (Figure 3.9). No accumulation of PEG control micelles was observed in the aortic tree sections of early stage mice. However, aortic tree sections from early and mid-stage ApoE -/- mice receiving VCAM-1 targeting micelles showed co-localization of anti-VCAM-1 antibody staining and Cy7 signal (Figure 3.9). Regions of intense Cy7 signal overlapped with areas shown to express VCAM-1 in mid-stage ApoE -/- mice receiving VCAM-1 targeted micelles, particularly at the crest of the plaque shown. Cy7 signal is observed throughout the aortic tree of mice receiving PEG micelles, but the signal was non-specific and was not enhanced in regions where VCAM-1 was expressed.

3.3.4 Micelle Biocompatibility and Biodistribution

Excised organs were imaged using near-infrared imaging to determine overall biodistribution of both targeting and control micelles. Figure 3.10 shows Cy7 signal in both the liver and kidney for VCAM-1 targeted micelles and PEG control micelles, providing evidence for clearance through the liver (reticuloendothelial or mononuclear phagocyte system) as well as the kidney and bladder (renal system). A statistically significant increase in average radiance from the kidney was observed for both early ($p = 0.002$) and mid-stage ($p = 0.001$) mice receiving VCAM-1 targeted micelles versus PEG micelles.

OCT embedded organs were cryosectioned and stained with hematoxylin and eosin (H&E) to determine the biocompatibility of both VCAM-1 targeted and PEG micelles. Morphological changes in the tissues were not seen in Figure 3.11 and thus no tissue damage was observed 24 hours after administration of either micelle formulation in the heart, lung, liver, spleen, intestine, kidney, or bladder as compared to the PBS control. Representative images of each organ are presented (Figure 3.11).

3.4 Discussion

3.4.1. Characterization of VCAM-1 targeting micelles

DSPE-PEG$_{2000}$-VCAM PAs were shown to form small, spherical micelles with approximately a 17 ± 2 nm diameter. Due to the large headgroup size conferred by the incorporation of a sizeable PEG chain, a spherical micelle is expected from geometrical packing factor calculations [29]. DLS confirmed the presence of one population of micelles sufficiently small to escape renal clearance and have a prolonged circulation time as has been demonstrated for 10-200 nm nanoparticles [4]. The CMC for both the control PEG micelle and actively targeted VCAM-1 micelle was shown to be between 14-17 μM. These CMC values are sufficiently low such that upon injection of 100 μL of a 1 mM solution, the concentration in circulation in the mouse will remain above the CMC, therefore maintaining micelles in solution.

Incorporation of the VCAM-1 targeting peptide into a micelle did not alter the secondary structure of the peptide as compared to the free peptide in solution and determined by circular dichroism. Peptide secondary structure, or potentially the lack thereof, will often dictate the ability of a peptide to bind to its target [30-32]. Previous studies have utilized a VCAM-1 targeting peptide alone or tethered to a contrast agent [6, 22, 33] but synthesized in a similar fashion to the procedure in this work, while this study employs the VCAM-1 targeting peptide in the headgroup of a micelle. Confining a peptide into a micelle headgroup maintains similar structure to other studies in the literature and should not affect the peptide's binding capacity.

3.4.2. In vitro biocompatibility and specificity

Previous *in vivo* studies using peptide amphiphile micelles injected 1 mM PA solutions [18, 34] resulting in a circulating concentration of approximately 62-80 μM in a 20 g mouse [35]. Cell viability was therefore assessed from 1-100 μM using both VCAM-1 targeting peptide as well as VCAM-1 targeting micelles in both human umbilical vein endothelial cells (HUVEC), a model endothelial cell line, and murine aortic endothelial cells (mAEC) as this exceeds the maximum concentration expected in circulation. All formulations showed less than 20% cell death as measured via the presto blue assay after a 24 hour incubation time.

Increased binding to mAECs was observed when incubating cells with VCAM-1 targeted micelles versus PEG control micelles or near-infrared dye-labeled amphiphiles alone. Figure 3.5 shows an increase in Cy7 signal in cells receiving VCAM-1 targeted or PEG micelles versus dye alone. These *in vitro* results provide evidence for the ability of micelles to increase binding to cells. VCAM-1 displaying micelles, however, further enhance binding to VCAM-1 overexpressing endothelial cells and may therefore be able to increase delivery to VCAM-1 expressing endothelial cells as part of an atherosclerotic plaque.

3.4.3. Active targeting of VCAM-1 in vivo and biocompatibility

To establish active targeting of atherosclerotic plaques, VCAM-1 targeting micelles were compared to PEG passive control micelles *in vivo*. PEG micelles have been shown to have an extended circulation time *in vivo* due to their ability to avoid opsonin binding, therefore averting phagocytosis [36]. Extending the circulation time of nanoparticles allows for non-specific accumulation. While important in cancer due to enhanced permeation and retention, a similar effect has also been alluded to in mouse models of atherosclerosis [4, 37]. In order to show specific accumulation greater than a passive control, a well-established mouse model, ApoE -/-, was used for these studies. Early stage plaques were formed in ApoE -/- mice by feeding a high fat diet for 10 weeks to develop stage II lesions characterized by lipoprotein accumulation leading to a cascade of inflammatory events [28]. Feeding ApoE -/- mice a high fat diet for 16 weeks formed mid-stage atherosclerotic plaques. Stage IV lesions were expected in these mice, depicted by the formation of a lipid core [28]. Ex vivo imaging of the aortic trees of ApoE -/- mice revealed a statistically significant difference and an approximately two-fold increase in average radiance between mice receiving VCAM-1 targeting micelles versus PEG micelles in both early ($p<0.001$) and mid-stage ($p<0.01$) mice, showing that the addition of the VCAM-1 targeting peptide to the micelle headgroup leads to accumulation of VCAM-1 targeted micelles at the developing plaque. Increased accumulation of PA micelles at plaques when compared to PEG micelles suggests active targeting to atherosclerotic plaques. Further specificity of VCAM-1 targeting micelles was observed through VCAM-1 antibody staining. Consecutive aortic tree sections show that VCAM-1 is expressed in the same location as Cy7 signal and is observed only in mice that received VCAM-1 targeted micelles, providing evidence for direct targeting of VCAM-1 using DSPE-PEG$_{2000}$-VCAM micelles. Active and specific targeting of the endothelium provides potential for using these VCAM-1 targeted micelles for diagnostic and therapeutic measures as VCAM-1 targeted micelles can potentially enhance the delivery of a payload to early and mid-stage plaques. Earlier stage detection can allow for intervention prior to the onset of a heart attack or stroke. In addition, targeted drug delivery would provide a means to decrease the systemic concentration of drug administered, potentially decreasing unwanted side effects.

In vivo imaging prior to sacrifice of early stage atherosclerotic mice shows accumulation of VCAM-1 targeting micelles in the cardiovascular system, but no detectable accumulation of PEG micelles (Figure 3.7). PEG micelles were observed at this 24 hour time point to be present in the bladder and liver. It is important to note that the aorta was not as clearly illuminated in mid-stage mice receiving VCAM-1 targeted micelles, however, it may be possible to optimize the imaging time frame to see enhanced micelle accumulation in mid-stage atherosclerotic mice. A time course study of micelle accumulation could elicit the rate at which micelles bind to plaques as well as the rate of clearance. These results provide further evidence for the diagnostic capabilities of VCAM-1 targeted micelles. Direct comparison of excised organs with *in vivo* imaging, however, is not plausible with these results due to the signal loss to the skin and penetration depth of near-infrared imaging. As such, an increase in Cy7 signal is observed in some excised organs when compared to radiance values calculated from *in vivo* images prior to sacrifice. Through the use of imaging techniques with improved resolution, it may be feasible to image the severity and observe the progression of plaque development.

Biocompatibility of both control PEG micelles and VCAM-1 targeted micelles was also established in the present study through H&E staining (Figure 3.11). Comparison of tissue samples from mice receiving an injection of PBS with no micelles present to mice injected with micelle samples showed no morphological changes among any of the tissues, providing evidence that these micelles are not cytotoxic *in vivo* up to 24 hours in circulation. Future studies will be required to show biocompatibility past this time point as well as the mechanism for complete clearance of the micelles.

Clearance was observed through both the reticuloendothelial system (RES) as well as the renal system (Figure 3.10). Due to the cut-off size of the renal system at approximately 5.5 nm [38, 39], clearance via the kidney and bladder is most likely due to the excretion of monomers rather than micelles. A decrease in Cy7 signal in the kidney in mice receiving PEG micelles may be due to the increased circulation time of PEG micelles, thereby increasing the *in vivo* stability of PEG micelles, and leading to a decrease in monomer clearance after a 24 hour circulation time. Clearance through the liver shows that micelles are cleared and may provide support for the ability of these micelles to remain intact and in circulation for this 24 hour study.

3.5 Conclusions

While PEG micelles have been shown in the literature to accumulate well *in vivo* due to their increased circulation time, the VCAM-1 targeted micelles presented here provide a distinct and quantifiable advantage. VCAM-1 targeted, Cy7-labeled micelles were shown to accumulate in the aortic tree of early and mid-stage atherosclerotic mice. These VCAM-1 targeted micelles were spherical in shape with a hydrodynamic diameter of 17 ± 2 nm and a critical micelle concentration of approximately 14 μM as compared to PEG control micelles with a hydrodynamic diameter of 9.6 nm and a critical micelle concentration of approximately 17 μM. *In vitro*, VCAM-1 targeted micelles were shown to bind to murine aortic endothelial cells to a greater degree than PEG micelles. *In vivo*, a similar result was seen where VCAM-1 targeted micelles accumulated at regions where VCAM-1 was expressed, as shown via immunohistochemistry. In early stage ApoE -/- mice, targeting to the cardiovascular system was observed using near-infrared imaging prior to animal sacrifice. H&E staining also revealed no tissue damage, providing evidence for the *in vivo* biocompatibility of these materials. These results show that VCAM-1 targeted micelles are able to specifically accumulate in areas of VCAM-1 expression in aortic trees. Future studies will show the ability of these VCAM-1 targeted micelles to deliver a drug of interest to earlier stages of plaque development allowing for intervention at an earlier disease state.

Figure 3.1 Peptide amphiphile (PA) composition, shape, and size. a) DSPE-PEG$_{2000}$ was conjugated to the VCAM-1 targeting peptide (sequence: VHPKQHR) via a thioether bond through a cysteine used for conjugation. b) Negative-stain TEM of 200 µM DSPE-PEG$_{2000}$-VCAM micelles shows the formation of spherical micelles. c) Micelle diameter was confirmed to be 17 nm at 200 µM in water using DLS.

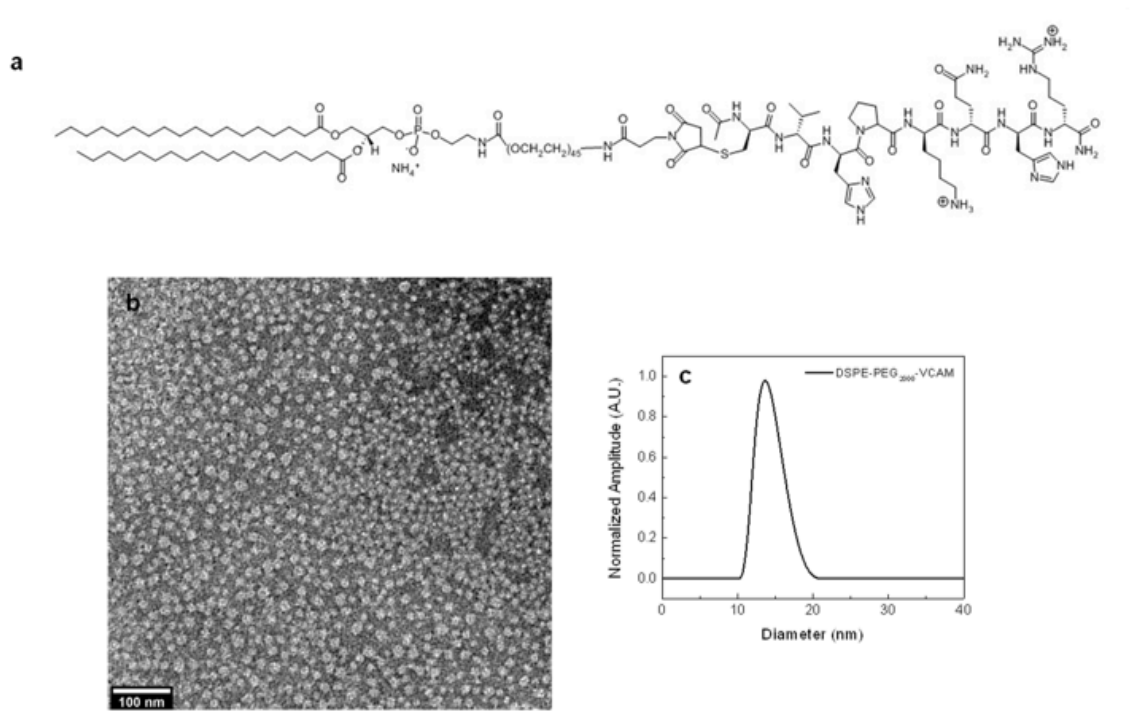

Figure 3.2 Characterization of DSPE-PEG$_{2000}$-VCAM micelles. a) Similar secondary structure is observed for the peptide in both the VCAM-1 targeting peptide as well as the VCAM-1 targeting micelles. b) Critical micelle concentration of VCAM-1 targeting micelles was found to be approximately 14 µM.

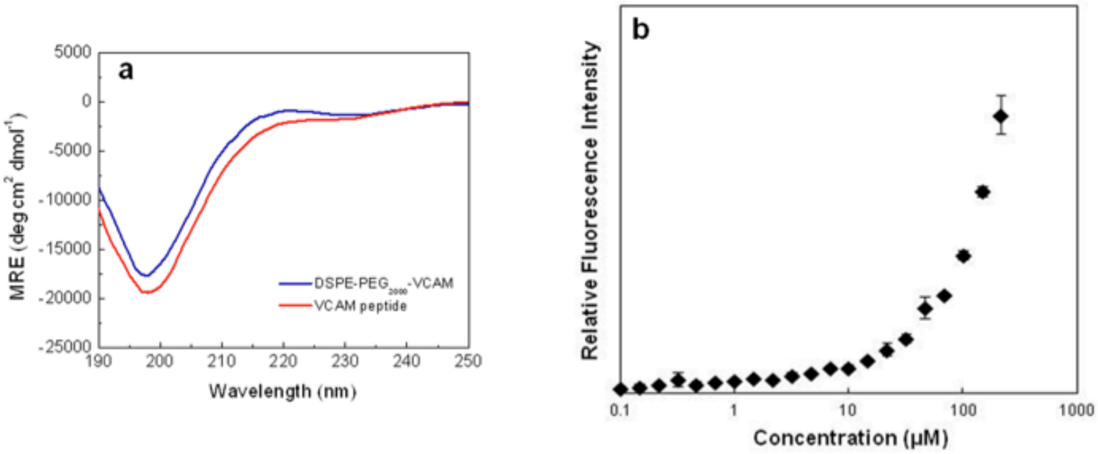

Figure 3.3 DSPE-PEG$_{2000}$ micelle properties. a) Dynamic light scattering shows the formation of one population of approximately 9.6 nm diameter micelles. b) Critical micelle concentration, as determined by the DPH method, was calculated to be 17 µM for DSPE-PEG$_{2000}$ micelles.

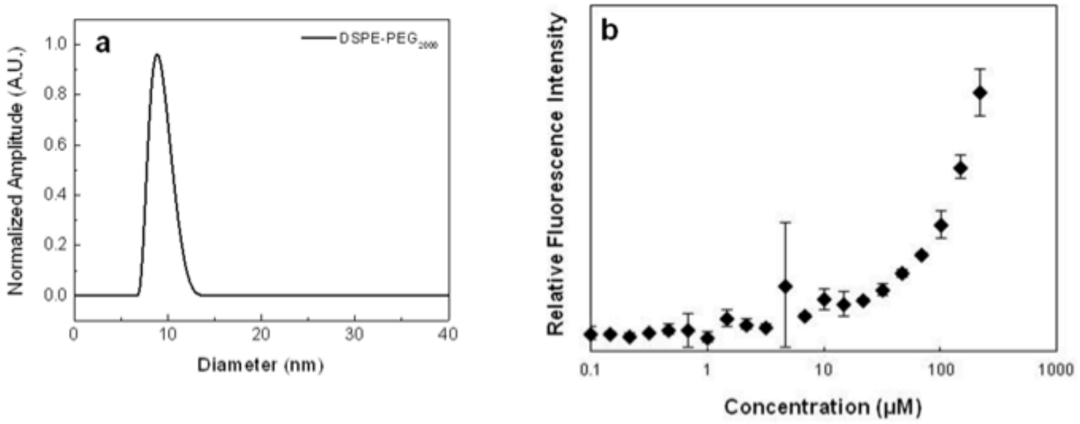

Figure 3.4 DSPE-PEG$_{2000}$-VCAM micelles and VCAM-1 targeting peptide are non-cytotoxic. Both human umbilical vein endothelial cells (HUVEC) and murine aortic endothelial (denoted "aortic") cells remain viable in the presence of varying concentrations of both VCAM-1 targeting peptide and micelles after 24 hours as compared to a PBS control.

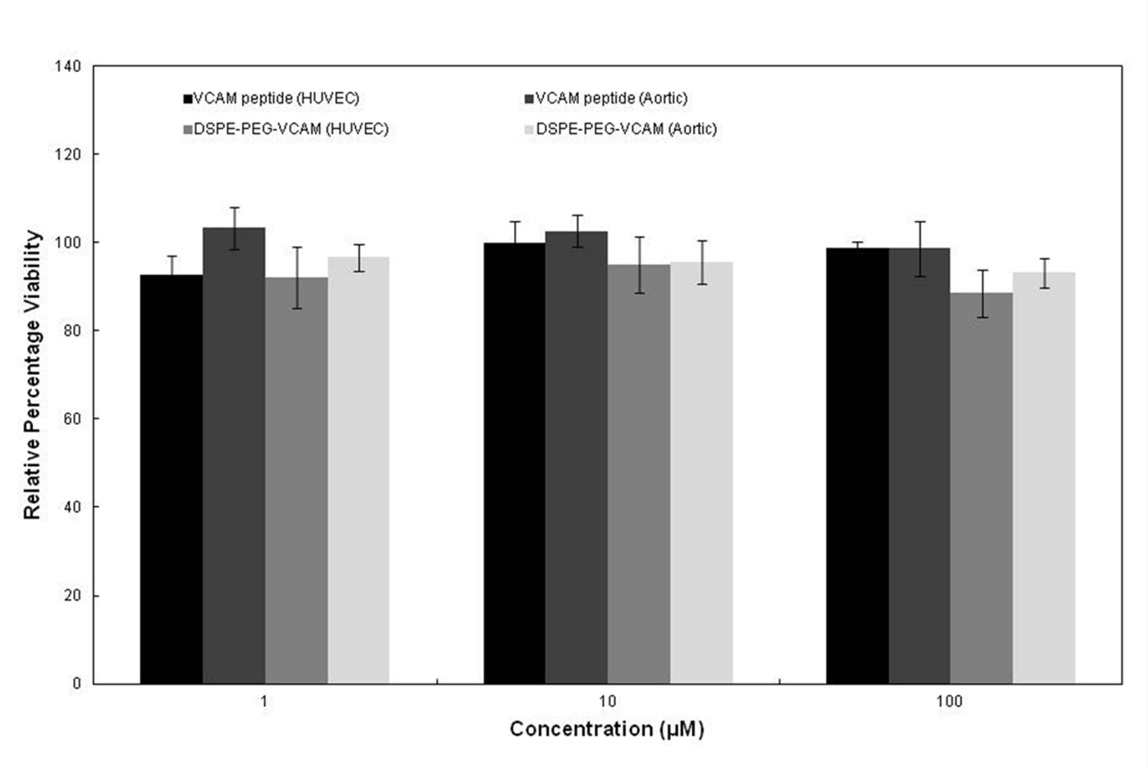

Figure 3.5 DSPE-PEG$_{2000}$-VCAM micelles bind to aortic endothelial cells. 3 hr incubation with 100 µM solutions of (a) DSPE-PEG$_{2000}$-Cy7 alone, (b) 90:10 DSPE-PEG$_{2000}$:DSPE-PEG$_{2000}$-Cy7 mixed micelles, or (c) 90:10 DSPE-PEG$_{2000}$-VCAM:DSPE-PEG$_{2000}$-Cy7 mixed micelles shows an increase in fluorescence when VCAM-1 targeting micelles are used. Nuclei: blue. Cy7: red.

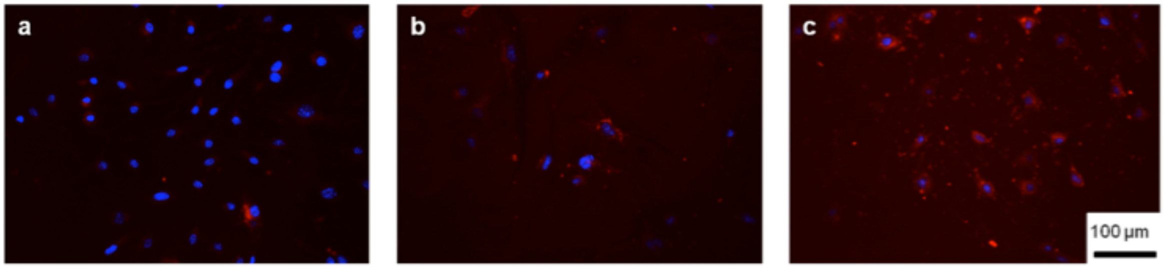

Figure 3.6 Quantification of Cy7 signal in murine aortic endothelial cells. ImageJ analysis shows a six-fold increase in Cy7 signal in cells incubated with VCAM-1 targeted micelles versus Cy7 monomers alone and a two-fold increase versus PEG micelles.

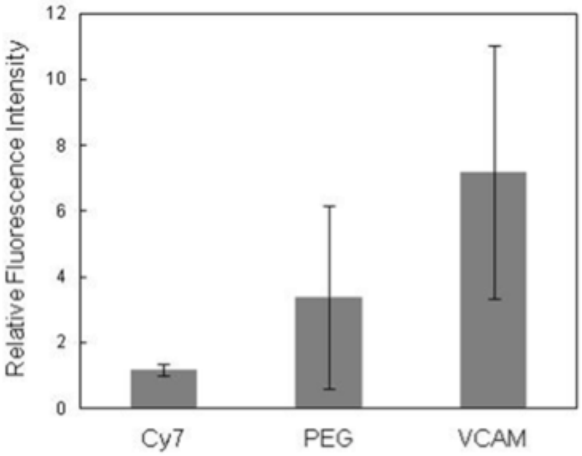

Figure 3.7 DSPE-PEG$_{2000}$-VCAM micelles are detectable via *in vivo* imaging in early stage ApoE -/- mice. a-d: DSPE-PEG$_{2000}$ control micelles do not show a strong signal in the aorta 24 hours post injection. Micelles are observed predominately in the bladder and liver. e-g: DSPE-PEG$_{2000}$-VCAM micelles 24 hours post injection. Near-IR *in vivo* imaging shows micelles are present predominately in the cardiovascular system (denoted by arrow). Neither DSPE-PEG$_{2000}$ control micelles (h-j) or DSPE-PEG$_{2000}$-VCAM micelles (k-m) show a strong signal in the cardiovascular system 24 hours post injection in mid-stage ApoE -/- mice.

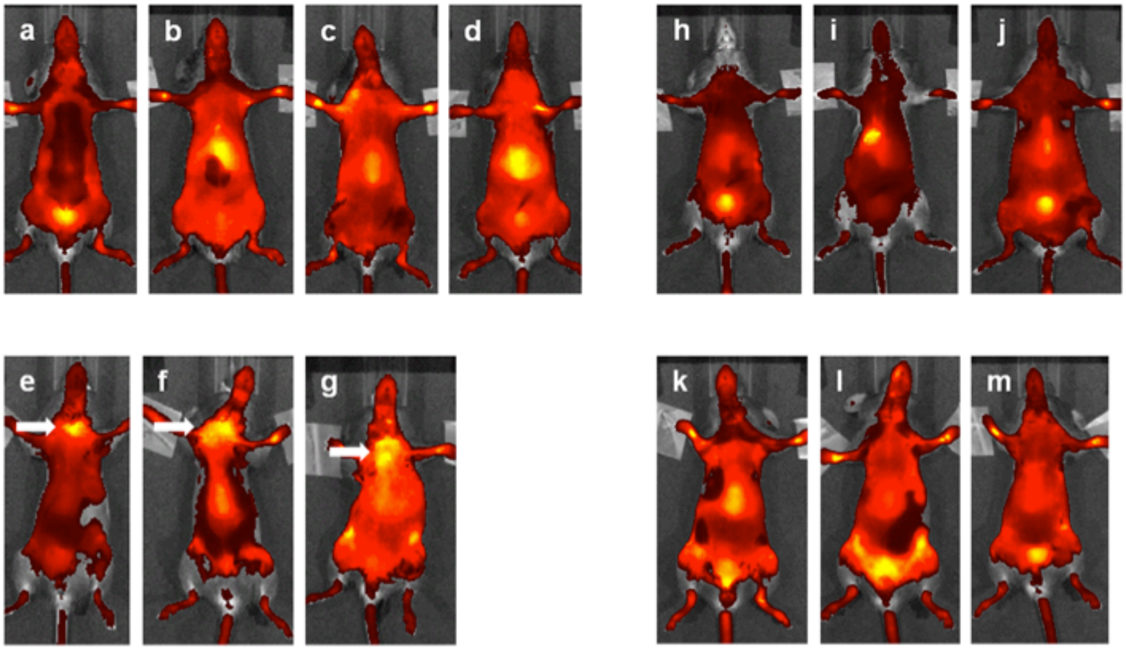

Figure 3.8 Active targeting of DSPE-PEG$_{2000}$-VCAM micelles. a) In vivo imaging of Cy7-labeled micelles shows accumulation in the aortic tree. b) Quantification of the deposition of micelles in the aortic tree shows statistical significance between control PEG micelles and actively targeted VCAM-1 micelles in both ApoE -/- mice with early stage plaques (*, p<0.001) and mid-stage plaques (**, p<0.01).

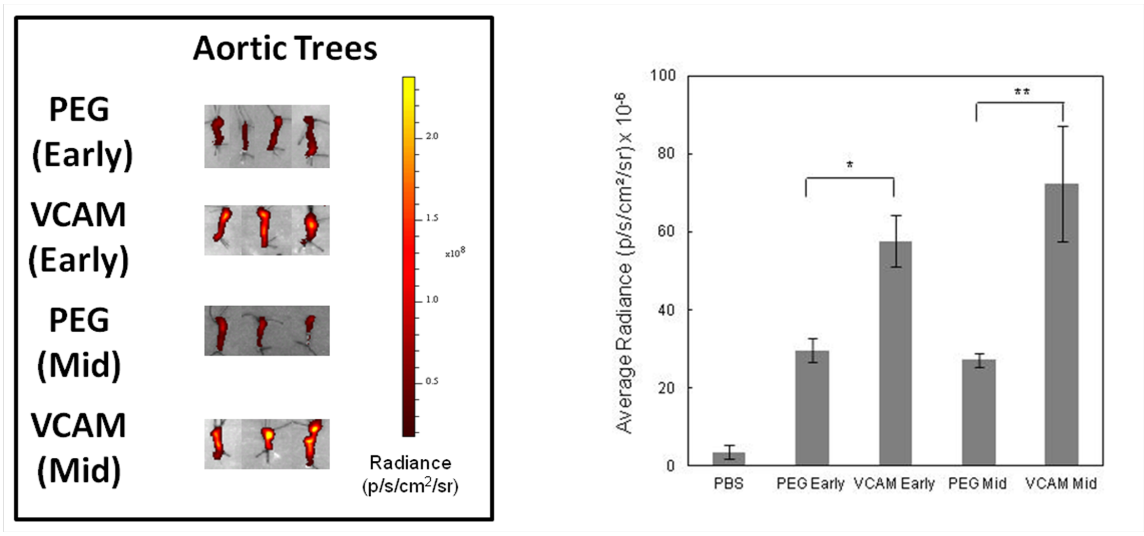

Figure 3.9 Histological sections show targeting to VCAM-1. No specific targeting is observed in early (a-c) or mid-stage (j-l) mice with PEG control micelles. (d-i) Deposition of VCAM-1 targeted micelles is observed in early stage mice in areas that overlap with VCAM-1 expression in both the endothelium (d-f) and adventitia (g-i). VCAM-1 targeting is also observed in mid-stage mice (m-o). In all images, consecutive slices were used for Cy7 imaging and immunohistochemistry. From left to right: brightfield, fluorescence, and anti-VCAM-1 stained slices. Brown: VCAM-1. Red: Cy7.

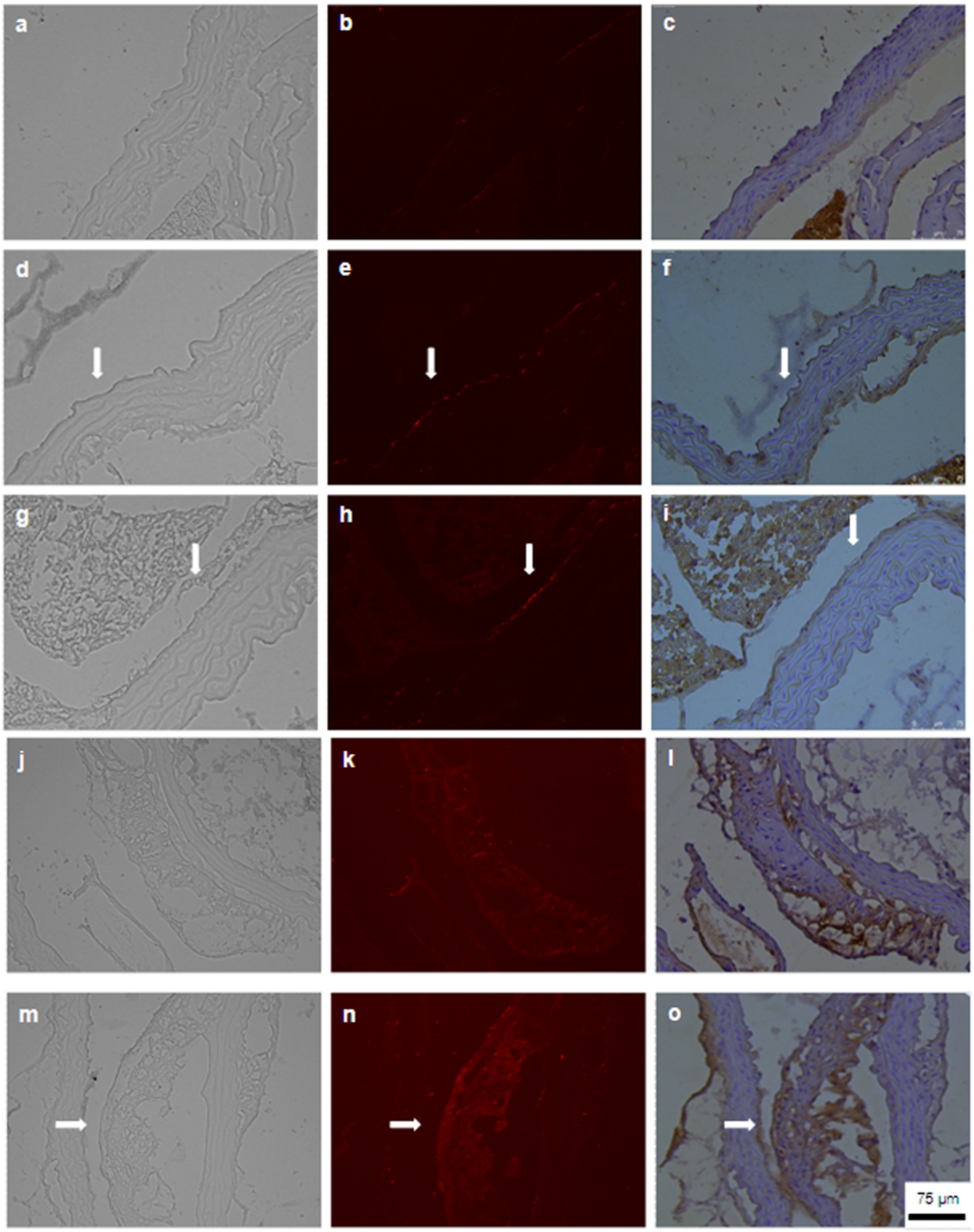

Figure 3.10 Biodistribution of PEG and VCAM-1 micelles 24 hr after injection. Relative distribution of PEG and VCAM-1 targeted micelles reveals clearance dominated through the liver and kidneys, showing the potential of both RES (reticuloendothelial system) and renal system clearance.

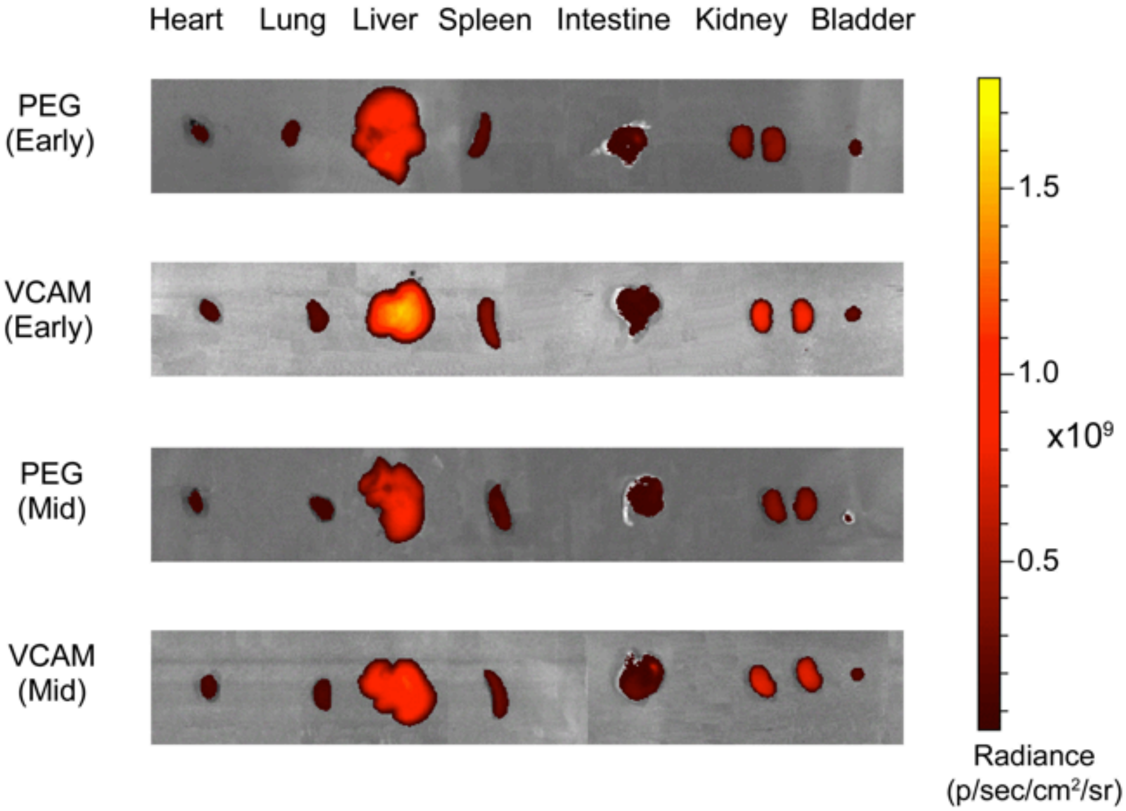

Figure 3.11 Biocompatibility of PEG and VCAM-1 micelles 24 hr after injection. H&E staining reveals no tissue damage, showing the *in vivo* biocompatibility of both PEG and VCAM-1 targeted micelles.

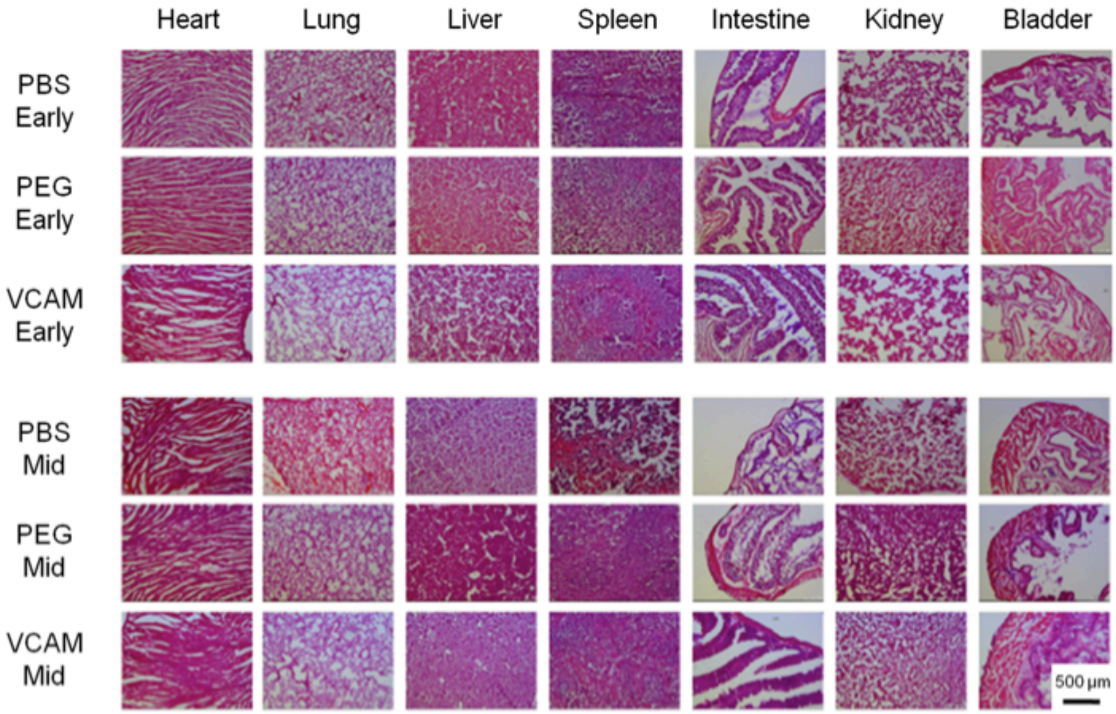

Table 3.1 Secondary structure of VCAM-1 targeting peptide and micelles. Quantification using fitting algorithms composed of a linear combination of polylysine basis spectra shows similar secondary structure in both the VCAM-1 targeting peptide and micelle. 200 µM solutions in water were used.

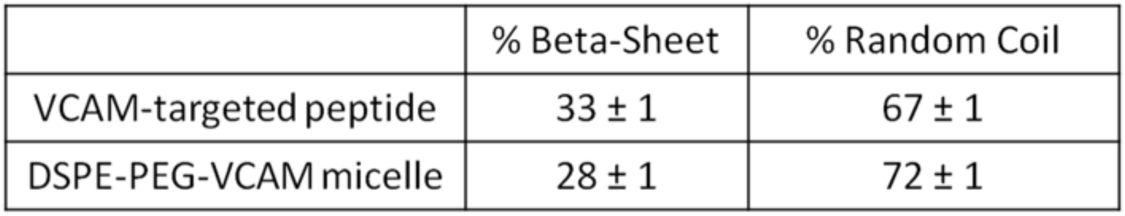

	% Beta-Sheet	% Random Coil
VCAM-targeted peptide	33 ± 1	67 ± 1
DSPE-PEG-VCAM micelle	28 ± 1	72 ± 1

References:

[1] Go AS, Mozaffarian D, Roger VL, Benjamin EJ, Berry JD, Borden WB, et al. Executive summary: heart disease and stroke statistics-2013 update: a report from the American Heart Association. Circulation 2013;127:143-52.
[2] Libby P. Inflammation in atherosclerosis. Nature 2002;420:868-74.
[3] Hansson GK, Libby P. The immune response in atherosclerosis: a double-edged sword. Nat Rev Immunol 2006;6:508-19.
[4] Lewis DR, Kamisoglu K, York AW, Moghe PV. Polymer-based therapeutics: nanoassemblies and nanoparticles for management of atherosclerosis. Wiley Interdiscip Rev Nanomed Nanobiotechnol 2011;3:400-20.
[5] Finn AV, Nakano M, Narula J, Kolodgie FD, Virmani R. Concept of vulnerable/unstable plaque. Arterioscler Thromb Vasc Biol 2010;30:1282-92.
[6] Nahrendorf M, Jaffer FA, Kelly KA, Sosnovik DE, Aikawa E, Libby P, et al. Noninvasive vascular cell adhesion molecule-1 imaging identifies inflammatory activation of cells in atherosclerosis. Circulation 2006;114:1504-11.
[7] Iiyama K, Hajra L, Iiyama M, Li H, DiChiara M, Medoff BD, et al. Patterns of vascular cell adhesion molecule-1 and intercellular adhesion molecule-1 expression in rabbit and mouse atherosclerotic lesions and at sites predisposed to lesion formation. Circ Res 1999;85:199-207.
[8] Cybulsky MI, Iiyama K, Li H, Zhu S, Chen M, Iiyama M, et al. A major role for VCAM-1, but not ICAM-1, in early atherosclerosis. J Clin Invest 2001;107:1255-62.
[9] Ley K, Huo Y. VCAM-1 is critical in atherosclerosis. J Clin Invest 2001;107:1209-10.
[10] O'Brien KD, Allen MD, McDonald TO, Chait A, Harlan JM, Fishbein D, et al. Vascular cell adhesion molecule-1 is expressed in human coronary atherosclerotic plaques. Implications for the mode of progression of advanced coronary atherosclerosis. J Clin Invest 1993;92:945-51.
[11] Nakashima Y, Raines EW, Plump AS, Breslow JL, Ross R. Upregulation of VCAM-1 and ICAM-1 at atherosclerosis-prone sites on the endothelium in the ApoE-deficient mouse. Arterioscler Thromb Vasc Biol 1998;18:842-51.
[12] Dimastromatteo J, Broisat A, Perret P, Ahmadi M, Boturyn D, Dumy P, et al. In vivo molecular imaging of atherosclerotic lesions in ApoE(-/-) mice using VCAM-1-specific, 99mTc-labeled peptidic sequences. J Nucl Med 2013;54:1442-9.
[13] Kelly KA, Allport JR, Tsourkas A, Shinde-Patil VR, Josephson L, Weissleder R. Detection of vascular adhesion molecule-1 expression using a novel multimodal nanoparticle. Circ Res 2005;96:327-36.
[14] Burtea C, Laurent S, Port M, Lancelot E, Ballet S, Rousseaux O, et al. Magnetic resonance molecular imaging of vascular cell adhesion molecule-1 expression in inflammatory lesions using a peptide-vectorized paramagnetic imaging probe. J Med Chem 2009;52:4725-42.
[15] Michalska M, Machtoub L, Manthey HD, Bauer E, Herold V, Krohne G, et al. Visualization of vascular inflammation in the atherosclerotic mouse by ultrasmall superparamagnetic iron oxide vascular cell adhesion molecule-1-specific nanoparticles. Arterioscler Thromb Vasc Biol 2012;32:2350-7.

[16] Trent A, Marullo R, Lin B, Black M, Tirrell M. Structural properties of soluble peptide amphiphile micelles. Soft Matter 2011;7:9572-82.
[17] Lukyanov AN, Torchilin VP. Micelles from lipid derivatives of water-soluble polymers as delivery systems for poorly soluble drugs. Adv Drug Deliv Rev 2004;56:1273-89.
[18] Peters D, Kastantin M, Kotamraju VR, Karmali PP, Gujraty K, Tirrell M, et al. Targeting atherosclerosis by using modular, multifunctional micelles. Proc Natl Acad Sci U S A 2009;106:9815-9.
[19] Berndt P, Fields GB, Tirrell M. Synthetic lipidation of peptides and amino acids: monolayer structure and properties. J Am Chem Soc 1995;117:9515-22.
[20] Thapa N, Hong HY, Sangeetha P, Kim IS, Yoo J, Rhee K, et al. Identification of a peptide ligand recognizing dysfunctional endothelial cells for targeting atherosclerosis. J Control Release 2008;131:27-33.
[21] Lien S, Lowman HB. Therapeutic peptides. Trends Biotechnol 2003;21:556-62.
[22] Kelly KA, Nahrendorf M, Yu AM, Reynolds F, Weissleder R. In vivo phage display selection yields atherosclerotic plaque targeted peptides for imaging. Mol Imaging Biol 2006;8:201-7.
[23] Davies MJ, Gordon JL, Gearing AJ, Pigott R, Woolf N, Katz D, et al. The expression of the adhesion molecules ICAM-1, VCAM-1, PECAM, and E-selectin in human atherosclerosis. J Pathol 1993;171:223-9.
[24] Knorr R, Trzeciak A, Bannwarth W, Gillessen D. New coupling reagents in peptide chemistry. Tetrahedron Lett 1989;30:1927-30.
[25] Fields GB, Noble RL. Solid phase peptide synthesis utilizing 9-fluorenylmethoxycarbonyl amino acids. Int J Pept Protein Res 1990;35:161-214.
[26] Chattopadhyay A, London E. Fluorimetric determination of critical micelle concentration avoiding interference from detergent charge. Anal Biochem 1984;139:408-12.
[27] Greenfield N, Fasman GD. Computed circular dichroism spectra for the evaluation of protein conformation. Biochemistry 1969;8:4108-16.
[28] Whitman SC. A practical approach to using mice in atherosclerosis research. Clin Biochem Rev 2004;25:81-93.
[29] Israelachvili JN. Intermolecular and surface forces. 3rd ed. San Diego: Elsevier; 2011, p. 538-50.
[30] Marullo R, Kastantin M, Drews LB, Tirrell M. Peptide contour length determines equilibrium secondary structure in protein-analogous micelles. Biopolymers 2013;99:573-81.
[31] Missirlis D, Farine M, Kastantin M, Ananthanarayanan B, Neumann T, Tirrell M. Linker chemistry determines secondary structure of p53(14-29) in peptide amphiphile micelles. Bioconjug Chem 2010;21:465-75.
[32] Tu RS, Marullo R, Pynn R, Bitton R, Bianco-Peled H, Tirrell MV. Cooperative DNA binding and assembly by a bZip peptide-amphiphile. Soft Matter 2010;6:1035-44.
[33] Bruckman MA, Jiang K, Simpson EJ, Randolph LN, Luyt LG, Yu X, et al. Dual-modal magnetic resonance and fluorescence imaging of atherosclerotic plaques in vivo using VCAM-1 targeted tobacco mosaic virus. Nano Lett 2014;14:1551-8.

[34] Chung EJ, Cheng Y, Morshed R, Nord K, Han Y, Wegscheid ML, et al. Fibrin-binding, peptide amphiphile micelles for targeting glioblastoma. Biomaterials 2014;35:1249-56.
[35] Diehl KH, Hull R, Morton D, Pfister R, Rabemampianina Y, Smith D, et al. A good practice guide to the administration of substances and removal of blood, including routes and volumes. J Appl Toxicol 2001;21:15-23.
[36] Lukyanov AN, Gao Z, Mazzola L, Torchilin VP. Polyethylene glycol-diacyllipid micelles demonstrate increased acculumation in subcutaneous tumors in mice. Pharm Res 2002;19:1424-9.
[37] Lobatto ME, Fuster V, Fayad ZA, Mulder WJ. Perspectives and opportunities for nanomedicine in the management of atherosclerosis. Nat Rev Drug Discov 2011;10:835-52.
[38] Choi HS, Liu W, Misra P, Tanaka E, Zimmer JP, Ipe BI, et al. Renal clearance of quantum dots. Nat Biotechnol 2007;25:1165-70.
[39] Rao J. Shedding light on tumors using nanoparticles. ACS Nano 2008;2:1984-6.

Chapter 4

Imaging Atherosclerotic Plaques using Peptide-Modified Iron Oxide Nanoparticles and Magnetic Particle Imaging

Abstract

Atherosclerosis is widely regarded as the leading cause of cardiovascular disease, one of the foremost causes of death not only in the United States, but around the world. Detecting atherosclerotic plaques remains challenging due to the slow and often asymptomatic nature of the disease. Imaging atherosclerotic plaques at the molecular level, however, could provide a means to carefully watch the progression of atherosclerosis and determine the most appropriate method of treatment. To this end, we have developed fibrin-binding superparamagnetic iron oxide particles (SPIOs) that are designed to specifically bind to late stage atherosclerotic plaques for use with magnetic particle imaging (MPI). SPIOs are a positive contrast agent when using MPI as this imaging technique directly measures a magnetic signal produced by the SPIOs when subjected to a magnetic field. These SPIO nanoparticles are shown to bind to fibrin in a linearly dependent manner that would allow for diagnosis of the amount of fibrin present in a given plaque. A model fibrin clot incubated with fibrin-binding SPIOs shows the ability of MPI to image the morphology of plaques, as well. Translating these results *in vivo* is possible because the MPI signal does not attenuate in the presence of tissues. Analysis of fibrin-binding SPIOs in a mouse model of atherosclerosis, ApoE -/- mice, showed low levels of deposition in the aortic tree, but clearance through the liver. Given the large liver signal, additional improvements to the nanoparticle system need to be made to increase the circulation time of these SPIOs and allow for specific binding to fibrous plaques to occur. Nevertheless, these fibrin-targeted SPIOs show great promise for binding to their intended target in a fashion linearly dependent on the amount of fibrin present, which would greatly enhance the ability to diagnose the severity of vulnerable atherosclerotic plaques using MPI.

4.1 Introduction

Magnetic particle imaging (MPI), a novel medical imaging modality conceived in 2005, holds great promise for imaging atherosclerosis in humans due to its inherent properties [1-3]. MPI provides a means to directly image superparamagnetic iron oxide nanoparticles (SPIOs) and therefore does not result in signal loss to tissues or penetration depth [4, 5]. Imaging is performed via the application of a magnetic field for which patient-based magnetostimulation safety parameters have been established [6]. The lack of ionizing radiation is a notable advantage over other currently commercialized imaging modalities. The use of iron oxide particles leads to clearance via the liver [7, 8] and allows for MPI to be safe for patients with chronic kidney disease [9], which represent approximately 11% of the population [10]. The correlation between chronic kidney disease and cardiovascular disease, though, leads to a much higher percentage of patients presenting with both of these diseases [11], where the use of kidney-cleared agents as gadolinium or iodine can be harmful [12, 13]. Perhaps most important is the positive contrast nature of the SPIO signal in MPI, which is in stark contrast to the negative contrast found in MRI [1]. Positive contrast allows SPIO deposition within the body to be quantified and provides a morphological analysis of the deposition, both of which are key for imaging atherosclerotic plaques in real time within the human body.

Atherosclerosis is the main cause of cardiovascular disease and is characterized by the formation of lipid-filled plaques located throughout the artery wall [14]. Atherosclerotic plaque formation begins with the accumulation of low density lipoprotein (LDL) within the artery wall and leads to an inflammatory response that recruits monocytes to the developing plaque [15]. As monocytes differentiate into macrophages and consume LDL, they become part of the growing lipid core of the plaque as foam cells. Over time, a fibrous cap can develop as a signifier of very late stages of plaque progression. The thickness of the fibrous cap has been suggested to correlate to the vulnerability of atherosclerotic plaques to rupture [16-18]. A thin fibrous cap leaves the plaque quite susceptible to rupturing and consequently downstream complications such as a heart attack or stroke due to the formation of a thrombus [19]. It is therefore hypothesized that the ability to determine the thickness and extent of fibrous cap formation would be beneficial to diagnosing those patients that have plaques susceptible to rupture. For this reason, we seek here to form a fibrin-binding SPIO nanoparticle that is both specific to fibrin as well as provides a means to quantify the amount of fibrin present within a plaque.

The literature demonstrates the use of peptides or antibodies to functionalized drug delivery or contrast agent systems to elicit binding to fibrin [20-26]. Specifically, a short, five amino acid peptide, CREKA, has been shown to bind directly to fibrin in a mouse model of atherosclerosis [27]. The biologically active sequence has been shown to be just REKA [21, 28], which allows for incorporation of an N-terminal cysteine for conjugation to a contrast agent. Both invasive and non-invasive techniques exist for imaging atherosclerotic plaques, but they suffer from a variety of disadvantages such as the use of ionizing radiation, signal loss to tissues, or a lack of penetration depth within tissues.

Here, a fibrin-targeting SPIO contrast agent is presented that binds to fibrin in a manner linearly dependent on the amount of fibrin present. Evidence is shown for the successful functionalization of iron oxide nanoparticles with the fibrin-binding peptide CREKA. A model clot is shown attached to a tube as a representation of the fibrous caps found *in vivo* and MPI imaging shows the ability to image the morphology of the plaque. To extend this work *in vivo*, a standard atherosclerosis mouse model, ApoE -/- mice, were injected with CREKA-functionalized SPIOs or control, amine-terminated SPIOs and their deposition in the aortic tree and clearance through the liver was assessed.

4.2 Materials and Methods

4.2.1 Synthesis and Purification of Labeled Iron Oxide Particles

Peptides were synthesized using standard fluorenylmethyloxycarbonyl chloride (Fmoc) solid phase peptide synthesis on rink amide resin with 0.47 mmol/g loading [29-31]. Fmoc protected amino acids were coupled using 3x molar excess of hydroxybenzotriazole (HOBt, AAPPTec LLC, Louisville, KY), 2-(1H-Benzotriazole-1-

yl)-1,1,3,3-tetramethyluronium hexafluorophosphate (HBTU, AAPPTec LLC, Louisville, KY), and *N,N*-diisopropylethylamine (DIPEA, Sigma-Aldrich, St. Louis, MO). The N-terminus of the peptide was acetylated using acetic anhydride following deprotection of the final Fmoc group using 1% 4-methylpiperidine (Sigma-Aldrich, St. Louis, MO) and 2% 1,8-diazabicyclo[5.4.0]undec-7-ene (DBU, Sigma-Aldrich, St. Louis, MO) by volume in dimethylformamide (DMF, Sigma-Aldrich, St. Louis, MO) in triplicate for five minutes each. The fibrin-binding sequence: CREKA was utilized for all functionality studies, but was modified to allow for the addition of a fluorescein dye to determine the number of peptides/particle as follows. The 1-(4,4-dimethyl-2,6-dioxocyclohexylidene)ethyl (Dde) group was first deprotected from the peptide, C-aminohexanoic acid-K(Dde)-aminohexanoic acid-REKA, using 2% hydrazine by volume (Alfa Aesar, Ward Hill, MA) in DMF. The deprotection reaction was done in triplicate with each deprotection reaction proceeding for five minutes. Addition of the fluorophore was achieved through a coupling solution of 2 equivalents of 5-(and-6)-carboxyfluorescein (Life Technologies, Carlsbad, CA), 4 equivalents of HOBt, 4 equivalents of HBTU, and 2 equivalents of DIPEA and was allowed to react for 5 hours. Cleavage from the resin along with complete deprotection of amino acid side chains was achieved using a trifluoroacetic acid (TFA):triisopropylsilane:water:1,2-ethanedithiol (94:1:2.5:2.5) solution for 2 hours. Cold diethyl ether was used to precipitate the resulting product. Purification was completed using reverse phase high performance liquid chromatography (HPLC, Prominence, Shimadzu Corporation, Kyoto, Japan) with a C_8 Waters column (Waters Corporation, Milford, MA). Matrix-assisted laser desorption/ionization (MALDI) mass spectrometry (Voyager DE Pro, Applied Biosystems, Life Technologies, Carlsbad, CA) allowed for confirmation of product purity.

Peptide-functionalized iron oxide particles were formed using a well-established method [32] (Figure 4.1). Briefly, amine-functionalized iron oxide particles (Micromod Partikeltechnologie GmbH, Rostock, Germany) were incubated with 3-(2-pyridyldithio)propionic acid *N*-hydroxysuccinimide ester (SPDP, Sigma-Aldrich, St. Louis, MO) dissolved in minimal dimethyl sulfoxide (DMSO, Sigma-Aldrich, St. Louis, MO) and adjusted to a pH of 6.5-7.5 using 100 mM phosphate buffer. The resulting solution was allowed to react for 4 hours before unreacted linker was removed by centrifugation using 100,000 molecular weight cut off vials (EMD Millipore, Billerica, MA) at 3,000 rpm for 5 minutes x 4. Particles were then incubated with an excess of CREKA peptide at a pH of 6.5-7.5 and allowed to shake at room temperature overnight. Purification proceeded as described above to remove unreacted peptide at 2,500 rpm for 5 min x 2 followed by 3,000 rpm for 5 min x 2.

4.2.2 Characterization of Iron Oxide Particles

To determine the number of peptides bound per particle, synthesized particles containing the fluorescent CREKA peptide were incubated with an excess of tris(2-carboxyethyl)phosphine hydrochloride (TCEP-HCl, Sigma-Aldrich, St. Louis, MO) for 4 hours at a pH of 6.5-7.5 to reduce the disulfide bond between the fluorescent CREKA peptide and the iron oxide particles. Resulting solutions were purified by centrifugation in a 100,000 molecular weight cut off vial at 3,000 rpm, 3,500 rpm, and 4,000 rpm for 5 minutes each followed by 4,000 rpm for 7 minutes to remove any excess solution. The filtered solution contained peptide, but was contaminated with a small amount of iron oxide particles that impeded accurate UV-visible (UV-vis) spectroscopy measurements. The resulting solutions were therefore filtered with 0.2 µm polyethersulfone filters (PES, GE Healthcare Bio-Sciences, Pittsburgh, PA), lyophilized, and re-constituted in 5 mM NaOH for UV-vis measurements. To control for the loss of peptide to the filter, fluorescent CREKA peptide was also filtered with 0.2 µm PES filters, lyophilized, and re-constituted in 5 mM NaOH to create a standard curve. UV-vis measurements were completed using 2 µL of each sample (N=4) on a NanoQuant plate (Tecan Group Ltd., Mannedorf, Switzerland) and read using a plate reader (absorbance: 492 nm, Infinite 200 Pro, Tecan Group Ltd., Mannedorf, Switzerland).

Fourier transform infrared spectroscopy (FTIR) was used to assess the successful binding of peptide to iron oxide particles using a PerkinElmer FT-IR Spectrometer with a diamond ATR accessory (Frontier, Waltham, MA). Iron oxide particles were lyophilized and analyzed at room temperature.

4.2.3 MPI Relaxometer and Scanner

The point spread function (PSF) of superparamagnetic iron oxide particles (SPIOs) was measured using a MPI relaxometer at a field of 25 kHz to determine the iron content of each sample. The peak signal intensity is proportional to the SPIO mass due to the linear and shift invariant qualities of x-space MPI [33]. Each SPIO sample was analyzed with the MPI relaxometer to correct for the iron content prior to any functionality study both *ex vivo* and *in vivo*.

In all experiments described, the MPI relaxometer was used with an excitation frequency of 25 kHz and excitation amplitude of 40 mT peak-to-peak (pp). The 25 kHz excitation signal was combined with a bias ramp field spanning 75 mT, centered at 0. In this manner, each MPI relaxometer scan excited the sample across a magnetic field of view (FOV) ranging from about -80 to +80 mT to capture the full magnetic relaxation behavior. Due to the fact that there is no gradient in the relaxometer system, there is no spatial localization of the signal. The relaxometer simply integrates all of the SPIO signal in the entire sample volume. In this sense, it can be described as a “0D” scanner.

Select experiments were run using the 3D field-free point (FFP) scanner in the Berkeley Imaging Systems Lab. This system uses an excitation frequency of 20.05 kHz and contains magnetic field gradients up to 7 T/m for spatial localization of the signal from SPIO tracer located in the FOV. In general, the pulse sequence details such as spatial FOV, partial field of view (pFOV) overlap, and number of averages vary between scans. 2D images are obtained by taking slices from the reconstructed 3D image or via projection methods such as the maximum intensity projection (MIP).

4.2.4 Fibrin Binding Assay

Binding to fibrin was determined through the formation of fibrin clots. Fibrin clot formation was modeled after a previously described procedure [20]. Briefly, lyophilized human plasma (Sigma-Aldrich, St. Louis, MO) and thrombin from human plasma (Sigma-Aldrich, St. Louis, MO) were reconstituted in a 100 mM calcium chloride (Acros Organics, Geel, Belgium) in water solution. Clots were formed in petri dishes by combining plasma, calcium chloride, and thrombin (2 units/µL) at a volumetric ratio of 3:1:0.27, respectively. Clots were allowed to incubate for 3 hours at 37°C and were washed extensively in 1X PBS prior to analysis with the MPI relaxometer with scanning conditions as described above.

To form a fibrin clot inside of a tube as a model plaque, a 225 μL plasma clot was first formed as described above by mixing the elements inside of a tube. Non-crosslinked components were removed by draining followed by passive pumping of the iron oxide solution through the tube via a 1 mL syringe. Particles were incubated with the clot for 3 hours prior to multiple rounds of washing with 1X PBS.

4.2.5 In Vitro Biocompatibility

To assess cell viability, human umbilical vein endothelial cells (HUVEC, Lonza Group Ltd, Basel, Switzerland) were cultured. Cells were grown in EGM-2 endothelial cell media (Lonza Group, Ltd, Basel, Switzerland) at 37°C and 5% CO_2 and were used for cell studies between passages 3-5. Cell viability was assessed by loading 5,000 cells/well in a 96 well plate. Cells were allowed to attach overnight before incubation with 10-1,000 μg iron/mL. As a control, cells received media only. Incubation proceeded for 24 hours. Each well was washed two times with 1X PBS. The presto blue assay (Invitrogen, Life Technologies, Carlsbad, CA) was used to determine cell viability and the results were read using a plate reader (ex. 560 nm, em. 590 nm, Infinite 200 Pro, Tecan Group Ltd., Mannedorf, Switzerland).

4.2.6 In Vivo Injections and Imaging

Female, transgenic, 4 week old mice homozygous for the *Apoe*^{tm1Unc} mutation (The Jackson Laboratory, Bar Harbor, ME) were fed a high fat diet (42% by fat, Harlan TD.88137, Indianapolis, IN) for 24 weeks to generate stage V lesions [34]. All animal experiments were approved by the University of California, Berkeley Animal Care and Use Committee (ACUC, Berkeley, CA). Mice were housed at the University of California, Berkeley. Prior to injection of 100 μL of a 20 mg Fe/kg solution in 1X PBS of either control particles or CREKA-functionalized particles, the tail vein was dilated in warm water (N=5). After 24 hours in circulation, the mice were anesthetized with 2.5% isoflurane in O_2 and imaged using the 3D FFP MPI scanner described previously. Mice were then euthanized via CO_2 overdose and the aortic tree, heart, and liver were harvested. The relative iron oxide particle signal from the aortic tree was analyzed using the MPI relaxometer.

4.2.7 Histology and Prussian Blue Staining

The aortic tree, heart, and liver were harvested and washed in cold 1X PBS followed by fixation overnight in 4% paraformaldehyde at 4°C. Tissues were then incubated in a 30% sucrose in 1X PBS solution for a minimum of 2 hours before half of the sucrose solution was removed and replaced with OCT (optimum cutting temperature compound, Tissue Tek, Sakura Finetek, Torrance, CA). After a 2 hour incubation period, the tissues were embedded in OCT (Tissue Tek, Sakura Finetek, Torrance, CA) and stored frozen at -80°C. Cryosectioning was achieved using a Microm HM 505 E (MICROM International GmbH, Walldorf, Germany) cryomicrotome. Organs were sliced at a thickness of 7 μm. Following sectioning, additional processing was completed via hematoxylin and eosin staining or Prussian blue staining kit (Ocean NanoTech, Springdale, AR). A DMI6000 B Leica Microsystems (Wetzlar, Germany) microscope was used to image the stained slides.

4.3 Results

4.3.1 Characterization of CREKA-Functionalized Iron Oxide Particles

FTIR analysis of dry CREKA-functionalized iron oxide particles showed the presence of several peaks not present in the amine-terminated iron oxide particles ("bare particles"). These key peaks provide evidence for the successful addition of CREKA peptide to the iron oxide particles. These peaks appear at 1154 cm^{-1}, 1562 cm^{-1}, and 1634 cm^{-1}, which are characteristic of a secondary amine stretch, secondary amine bend, and carbonyl stretch, respectively (Figure 4.2 and Table 4.1) [35]. Additionally, UV-vis analysis, corrected by the percentage of peptide lost to the filtering process (Figure 4.11), ranged from 104-458 peptides/particle with an average of 274 peptides/particle. The hydrodynamic diameter, as supplied by Micromod, the manufacturer of the amine-terminated iron oxide particles, was approximately 100 nm. Transmission electron microscopy (TEM) shows the iron oxide core to be approximately 24 ± 3 nm (Figure 4.12).

4.3.2 Fibrin Binding of Iron Oxide Particles

In vitro binding was assessed using a fibrin clot assay. Fibrin clots of varying sizes formed from human plasma, calcium chloride, and thrombin from human plasma were incubated with an equal amount of iron oxide particles from two groups: control Micromod or CREKA-functionalized Micromod. Iron oxide particles were first tested using the relaxometer to ensure equivalent MPI peak signal from control and CREKA particles. As observed in Figure 4.3, a nearly linear relationship between peak MPI iron oxide signal and clot size was shown. MPI peak signal from fibrin clots incubated with control Micromod particles does not scale with clot size.

A fibrin clot was also formed inside of a plastic tube as a model atherosclerotic late-stage plaque. After incubation with CREKA-functionalized Micromod particles for 3 hours, a representative MPI scan is shown in Figure 4.4. The largest signal is observed in the region where the clot is located and begins to mimic the shape of the clot as seen in the photograph (Figure 4.4, a).

4.3.3 Biocompatibility of Functionalized Materials In Vitro

Biocompatibility of CREKA-functionalized iron oxide particles was determined *in vitro* using a presto blue cell viability assay. Cell death was not observed until cells were incubated with a large concentration of iron oxide particles, namely 1,000 μg Fe/mL (Figure 4.5). Cells were incubated with the iron oxide particles overnight. Due to the interference of iron oxide particles with obtaining an accurate signal using a plate reader, the media alone was removed and used for analysis.

4.3.4 Iron Oxide Particle Biocompatibility and Deposition In Vivo

Prussian blue staining of the heart from mice receiving both control and CREKA-functionalized iron oxide particles showed no accumulation of iron oxide (Figure 4.6). Slices of the heart at a range of locations were stained with no iron oxide discovered at any depth. Iron oxide particles were abundant in the liver of both groups of mice, those receiving the control and CREKA particles (Figure 4.6). H&E staining, however, revealed no morphological or cellular changes in the heart or liver after a 24 hour circulation time, showing that both of these materials are biocompatible after 24 hours *in vivo* (Figure 4.7).

Prussian blue staining of the excised aortic tree revealed minimal iron oxide particles in both mice receiving the control or CREKA particles. As observed in Figure 4.8a and c, many slices showed no iron oxide particles. However, iron oxide particles did appear in the plaque region in slices of the aortic tree from ApoE -/- mice receiving either control or CREKA particles (Figure 4.8b and d).

4.3.5 Imaging ApoE -/- Mice using Magnetic Particle Imaging

ApoE -/- mice were imaged with a magnetic particle imaging (MPI) system 24 hours after injection with 100 μL of a 20 mg Fe/kg solution. MPI revealed a saturated signal in the liver, which masked the ability to distinguish the aortic tree or the cardiovascular system from the liver (Figure 4.10). No iron oxide particles were observed in any region beyond the liver and surrounding organs. Excision of the aortic tree and analysis via MPI did not result in any distinguishable signal.

4.4 Discussion

CREKA-functionalized SPIOs were shown to be successfully synthesized using IR spectroscopy. Appearance of peaks corresponding to a carbonyl amide stretch (1634 cm^{-1}), a secondary amine bend (1562 cm^{-1}), and a secondary amine stretch (1154 cm^{-1}), all of which correspond to the addition of a peptide as compared to the SPIO particles alone, provide evidence for the successful synthesis of peptide-functionalized SPIO particles (Figure 4.2 and Table 4.1). Here, the number of peptides/particle reported is approximately 274. This value is highly dependent on the number of amine-terminated chains per particle and thus varies throughout the literature depending on the particular characteristics of each system, despite using a similar synthesis technique [32]. The range in values for the number of peptides/particle could be due to the polydispersity of the starting material, control Micromod-amine particles.

The specific targeting ability of CREKA-functionalized SPIO particles was shown through an *in vitro* fibrin clot assay. The peptide, CREKA, has previously been established to bind to fibrin *ex vivo* [21] and *in vivo* [27] and, in fact, only the REKA sequence is necessary for binding, allowing inclusion of a cysteine for conjugation purposes [21, 28]. By changing the clot size and therefore the amount of fibrin, a linear trend in iron oxide content was established using the CREKA SPIOs (Figure 4.3). The use of non-specific, control SPIOs showed no correlation between clot size and iron oxide content, providing evidence that control SPIOs bind non-specifically with a baseline amount bound regardless of the fibrin content. The implication for this binding capability is the ability to image the severity of plaques and extent of fibrin *in vivo* based upon the MPI signal. Through direct targeting of markers of different stages of plaque development, it may be possible to diagnose the progression of atherosclerosis in a quantifiable manner and watch atherosclerosis progression over time. Further evidence for the applicability of MPI imaging is shown in Figure 4.4, where a model clot was imaged to show the potential to image the morphology of fibrin deposition. This can be extended *in vivo* to be able to image plaque morphology as well.

Prior to *in vivo* analysis, *in vitro* biocompatibility was confirmed via cell viability after a 24 hour incubation time. Cell death was not observed until an exceedingly large amount of iron was incubated with the cells, namely 1,000 μg Fe/mL (Figure 4.5). For reference, the injected dose of SPIOs is approximately 250-317 μg Fe/mL based on a 20 g mouse [36] and a large amount of injected SPIOs are known to quickly clear from the blood stream via macrophages [7]. This ultimately further reduces the systemic concentration of SPIOs, but also reduces the number of particles available to bind to the site of interest, namely, atherosclerotic plaques in the aorta.

Given the *in vitro* biocompatibility after a 24 hour incubation time, CREKA-functionalized SPIOs and control SPIOs were investigated using a well established atherosclerosis mouse model, ApoE -/- mice. ApoE -/- mice are known to develop lesions of varying stages, which can be controlled by the length of expose to a high fat diet [34, 37]. Here, ApoE -/- mice were fed a high fat diet for 24 weeks to generate stage V lesions characterized by the development of a fibrous cap. Initial live, *in vivo* imaging using a MPI scanner led to images saturated by the liver signal (Figure 4.10). To further determine the amount of iron oxide particles in the aortic tree, excised tissues were cryosectioned and stained using Prussian blue (Figure 4.8). This revealed areas of iron oxide particles within the plaque as well as within the media, or the interior of the artery wall (data not shown). Interestingly, iron oxide particles were not observed at the corners or crest of the plaque where fibrin would be expected [27]. This could potentially be due to macrophage clearance of SPIOs on the luminal side of the atherosclerotic plaque. SPIO uptake by macrophages could also have resulted in the accumulation of iron oxide particles within the plaque. Brown regions in the aortic tree are thought to be blood, as determined by H&E staining (Figure 4.9). The lack of large amounts of accumulated iron oxide particles may account for the weak to indistinguishable signal from the aortic trees using MPI. However, our previous pilot study was able to distinguish a signal in the brachiocephalic artery using MRI [38]. Given these results, we believe that as the resolution of MPI improves as well as an optimal, single magnetic moment particle is developed, in the future we will be able to identify the morphology and relative signal strength from atherosclerotic plaques *in vivo*. Additional improvements to the system can be achieved via a time course study to establish the clearance of the SPIOs and therefore a time frame over which the liver signal does not saturate the resulting image. Other peptide targeting systems could also be explored to allow for time to intervene in the progression of atherosclerosis, namely using a VCAM-1 targeting peptide [39-41], RGD [42, 43], or other peptides that bind to earlier stages of plaque progression. Optimization of both the size of magnetic particles used given the dependence of size on nanoparticle clearance [44] as well as the number of peptides per particle could potentially greatly improve this system. Taking advantage of monocyte re-circulation to the aorta could also provide an opportunity to improve the targeting ability of these SPIOs [45].

Despite the low deposition of SPIOs in the aortic tree, the study successfully showed that no non-specific accumulation of SPIOs was observed in the heart (Figure 4.6). Clearance was seen through the liver (Figure 4.6, 4.10), as is expected for SPIOs [7], especially given their size range, which is larger than the renal system cut-off of approximately 5.5 nm [46, 47]. Additionally, no cellular of morphological changes were observed in the liver via H&E staining (Figure 4.7), which provides evidence that these materials are not harmful *in vivo* up to 24 hours in circulation and future time course studies will be used to fully assess *in vivo* biocompatibility as well as the time frame for complete clearance of the contrast agent.

4.5 Conclusions

We present here a peptide-functionalized SPIO nanoparticle system that binds to its target, fibrin, in a linearly dependent manner as quantified via MPI. We also show the ability to image the morphology of model atherosclerotic clots. *In vivo,* these iron oxide particles are cleared through the liver, which is important for imaging atherosclerosis in patients with chronic kidney disease. MPI provides a means to image *in vivo* without losing signal to tissues and therefore does not suffer from penetration depth losses as other imaging techniques. Combining the linear relationship between SPIO MPI signal and amount of deposited SPIOs with the ability to distinguish plaque morphology, magnetic particle imaging holds great promise for the detection of atherosclerosis in humans.

4.6 Supplemental Information

4.6.1 Standard Curve for Fluorescein Absorption

To account for the loss of peptide to the filtering process, CREKA-fluorescein peptide was filtered in the same fashion as described in section 4.2.2. The resulting solution was lyophilized and the concentration of remaining peptide was determined using the Beer-Lambert Law. Absorption values for 2 μL samples loaded onto a NanoQuant plate (Tecan Group Ltd., Mannedorf, Switzerland) were determined using a plate reader (absorbance: 492 nm, Infinite 200 Pro, Tecan Group Ltd., Mannedorf, Switzerland). The concentration of peptide prior to filtration and post-filtering were used to create a standard curve, as shown in Figure 4.11.

4.6.2 Transmission Electron Microscopy

The iron oxide core size was determined using transmission electron microscopy (TEM). Iron oxide particle solutions were loaded onto ultrathin carbon type-A 400 mesh copper grids using 1 μL of sample. The grids were allowed to nearly dry before excess solution was wicked away using filter paper. TEM was performed using a FEI Tecnai 12 TEM at an accelerating voltage of 120 kV. Figure 4.12 shows a TEM image of the Micromod-amine particles. ImageJ was used to calculate an average iron oxide core size of 24 ± 3 nm. Given the non-spherical nature of the particles, dynamic light scattering could not be used to adequately determine the hydrodynamic diameter of the particles.

Figure 4.1 Synthesis of peptide-functionalized iron oxide particles. Amine-functionalized iron oxide particles were reacted with pyridyl disulfide and purified. Purified particles were then allowed to react overnight with CREKA peptide to form CREKA-functionalized particles.

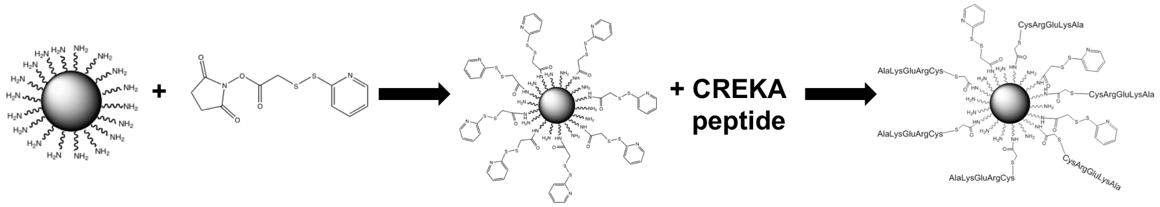

Figure 4.2 IR shows peptide bound to iron oxide particles. The appearance of several, distinct peaks for the creation of an amide or peptide bond appear in the lower spectrum for the Micromod + CREKA particles versus the top, control Micromod particle spectrum.

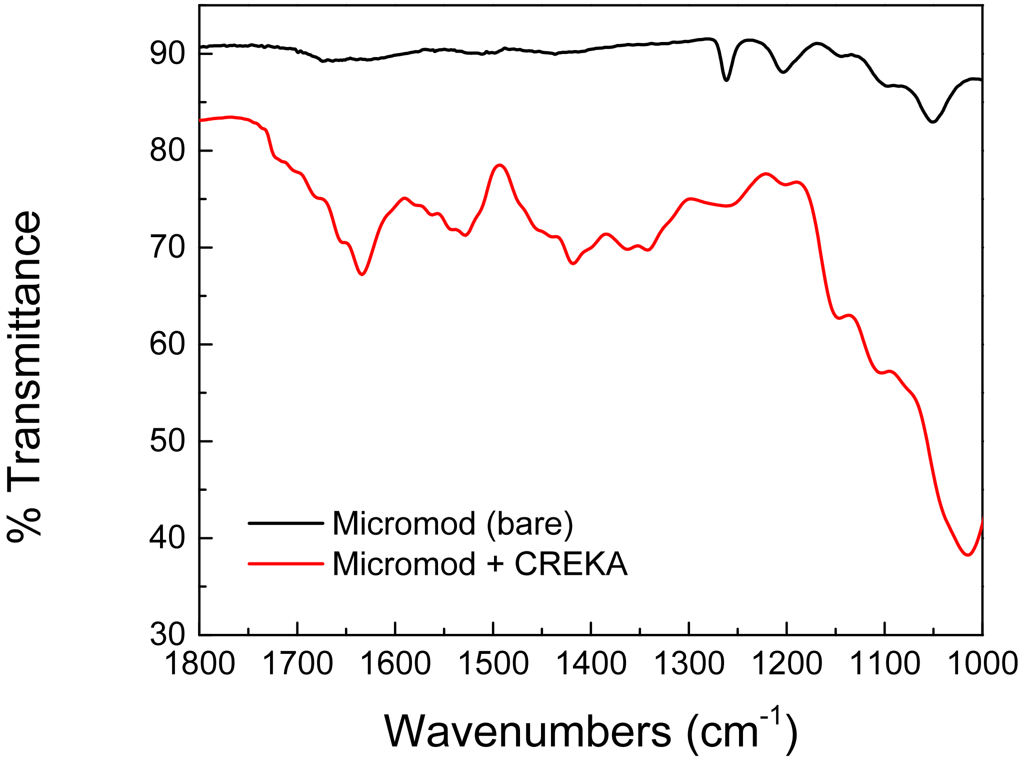

Table 4.1 Assignment of IR peaks from peptide addition. Peaks which appear in the Micromod + CREKA spectrum that are not observed in the control, Micromod particle spectrum are assigned. Each assigned peak corresponds to the addition of a peptide to the iron oxide particles.

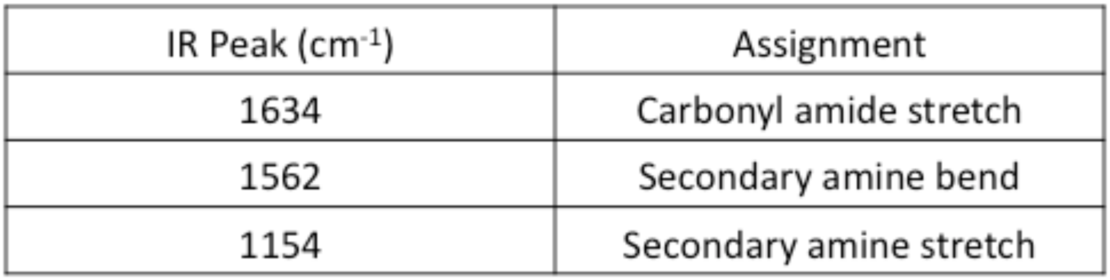

IR Peak (cm^{-1})	Assignment
1634	Carbonyl amide stretch
1562	Secondary amine bend
1154	Secondary amine stretch

Figure 4.3 Clot-binding assay. No trend in MPI peak signal is observed for the control iron oxide particles whereas a linear trend in MPI peak signal is seen between the clot size and MPI peak signal for CREKA-functionalized iron oxide particles, showing the targeting ability of the CREKA particles. An increase of 3-5 times the signal from the targeted CREKA particles was observed versus the non-targeted control particles for the 450 - 675 µL clots.

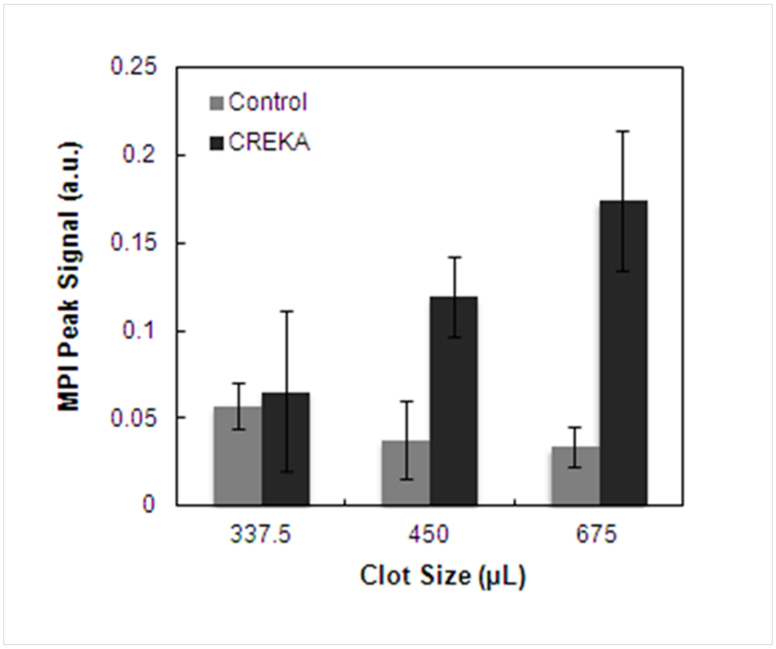

Figure 4.4 Model fibrin clot. A fibrin clot was formed as a model atherosclerotic plaque inside of a plastic tube (a) and imaged using MPI. Two small clots are observed in (a) and regions of strong signal are correspondingly seen in the same location in the x (b) and y (c) directions.

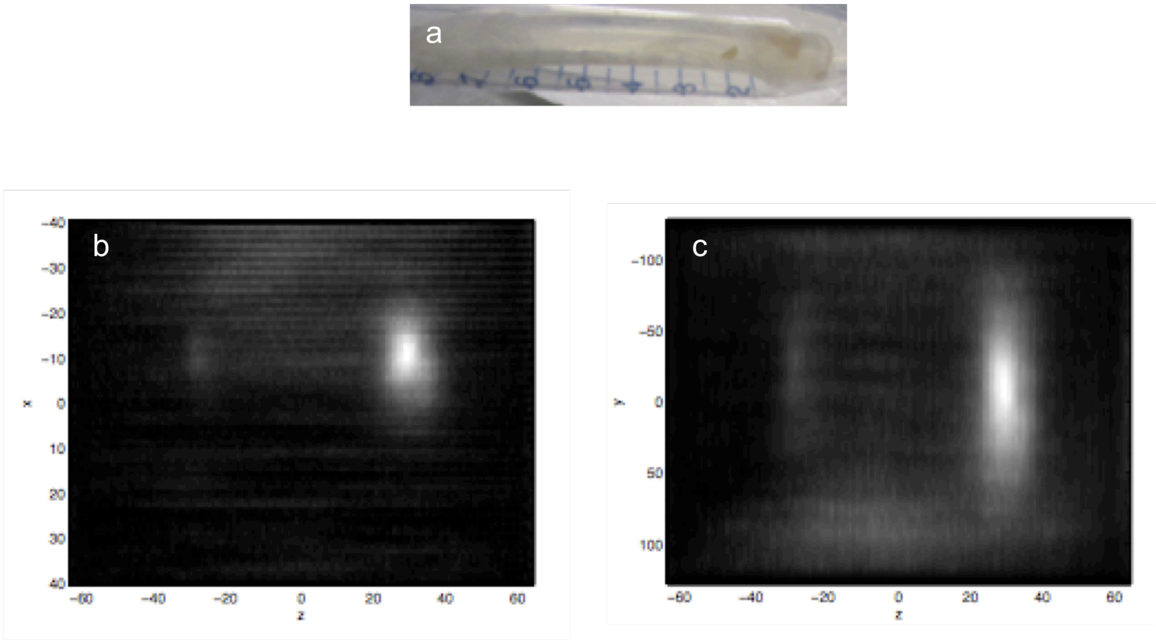

Figure 4.5 ***In vitro*** **biocompatibility of iron oxide particles.** A 24 hour incubation with iron oxide particles showed good cell viability. Cell death is only observed after incubation with 1,000 μg iron/mL.

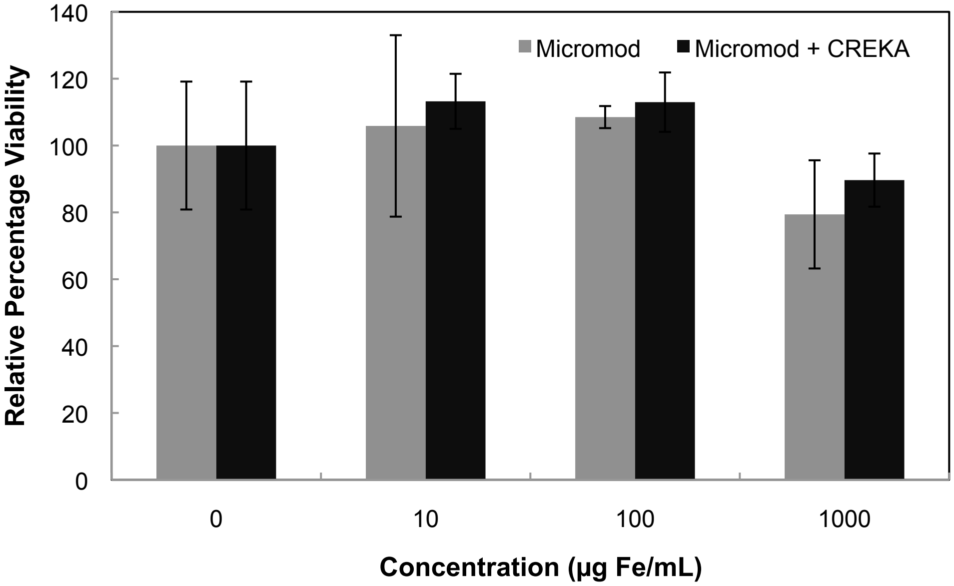

Figure 4.6 Prussian blue staining of iron oxide particles. a-b: Iron oxide particles were not observed in the heart via Prussian blue staining. c-d: Prussian blue staining of the liver reveals iron oxide particles in both mice that received the control and CREKA-functionalized particles. Blue: iron oxide particles.

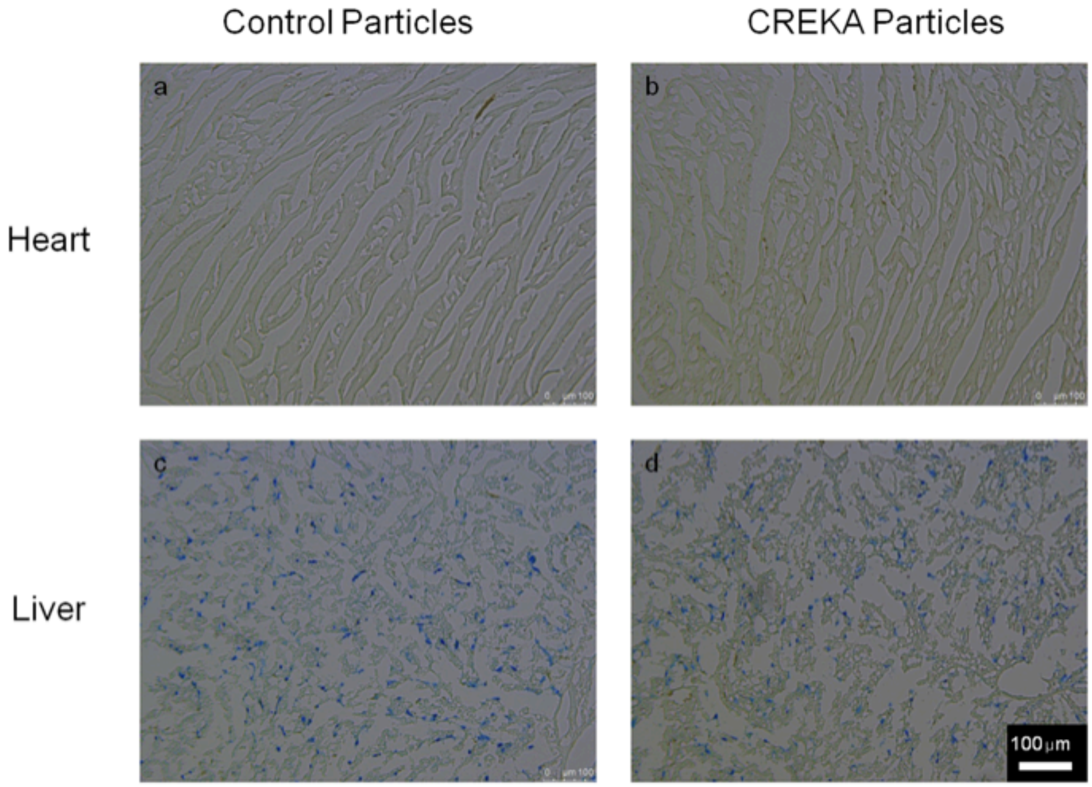

Figure 4.7 H&E shows biocompatibility in the heart and liver after a 24 hr circulation time. No morphological changes were observed in the heart (a-b) or liver (c-d) as shown by H&E staining.

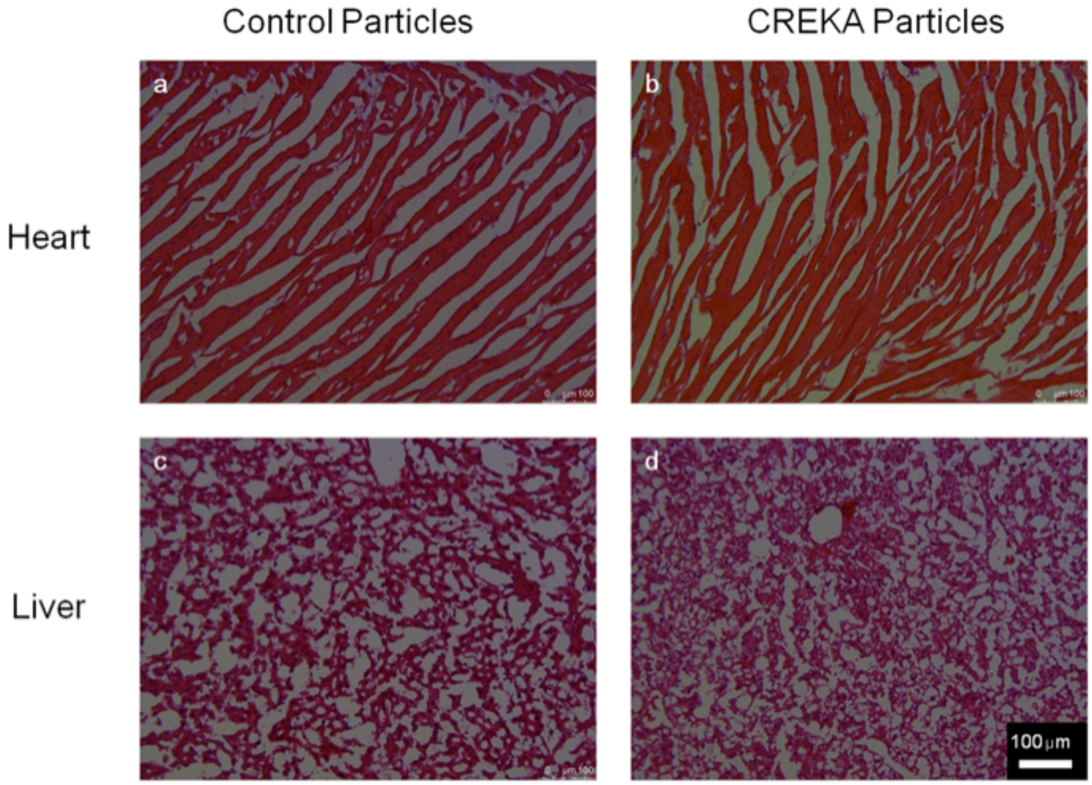

Figure 4.8 Prussian blue staining of the aortic tree. Aortic tree slices stained with Prussian blue exhibited a range of deposited iron oxide particles from no particles (a,c) to particles observed in the plaque (b,d) for both control and CREKA-functionalized particles. Blue: iron oxide particles.

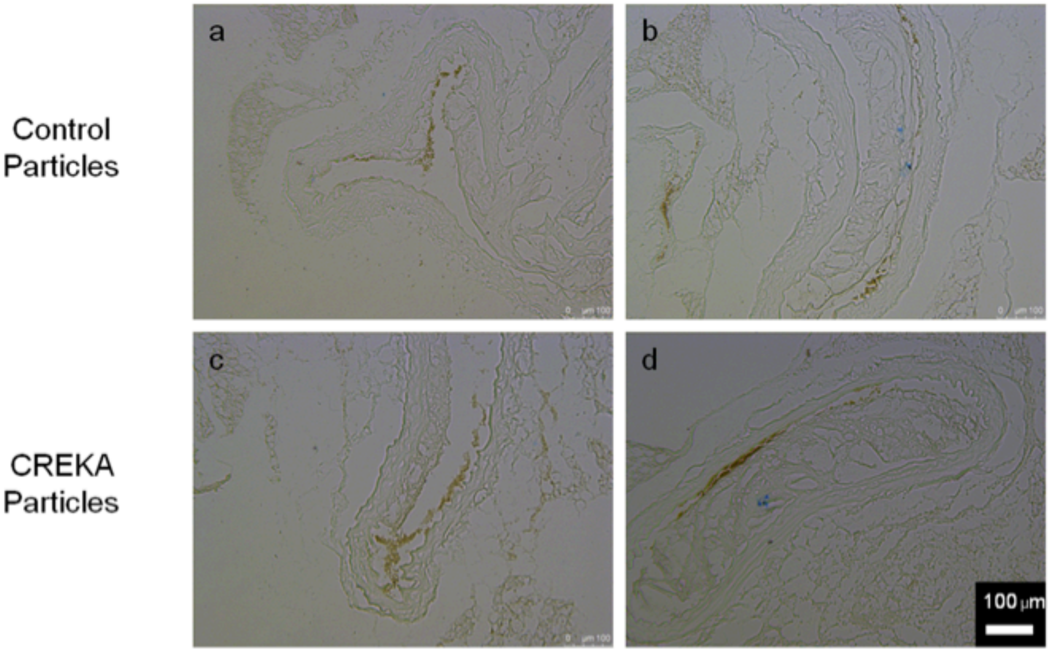

Figure 4.9 H&E staining of aortic trees. H&E staining shows that the brown region of the interior of the aortic tree slice is from blood due to its characteristic color and morphology after staining. Aortic tree images from mice receiving (a) control particles or (b) CREKA-functionalized particles are presented.

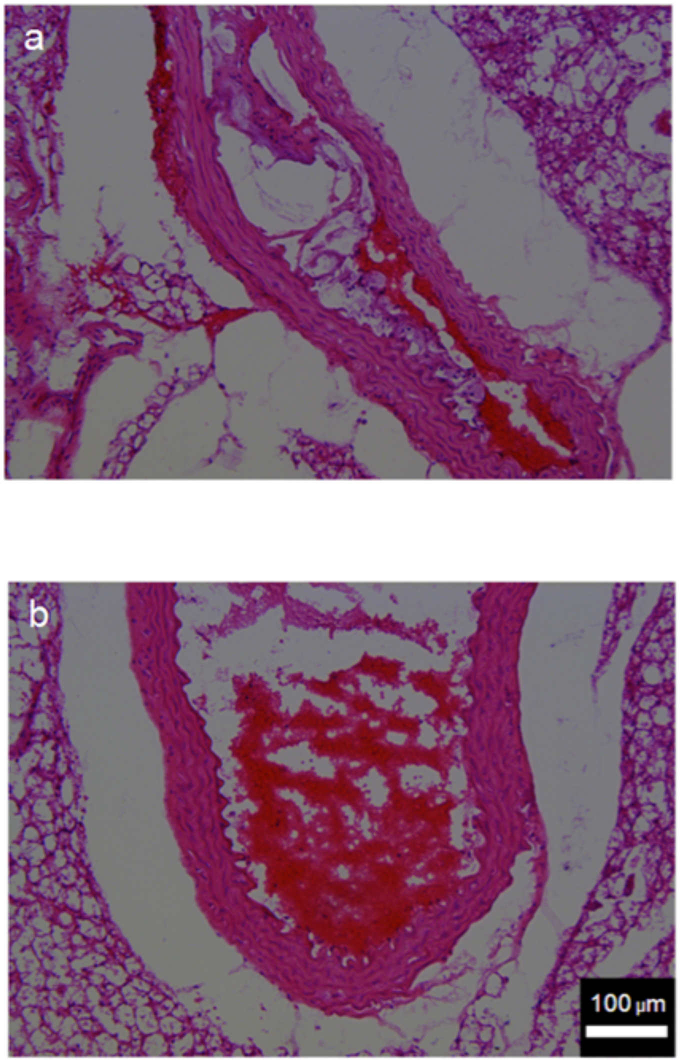

Figure 4.10 Live *in vivo* image using Magnetic Particle Imaging of ApoE -/- mice. A large liver signal from clearance of iron oxide particles masks any ability to image the aortic tree in ApoE -/- mice receiving CREKA-functionalized particles.

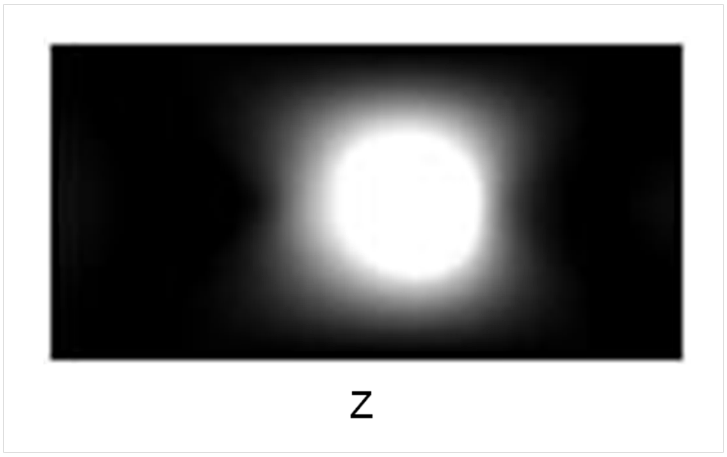

Figure 4.11 Quantification of the number of peptides per particle. In order to account for the loss of peptide to the filter, control solutions of known quantities of peptide were filtered and analyzed using UV-visible absorbance values. These values were used to correct for the percentage of peptide lost to the filter.

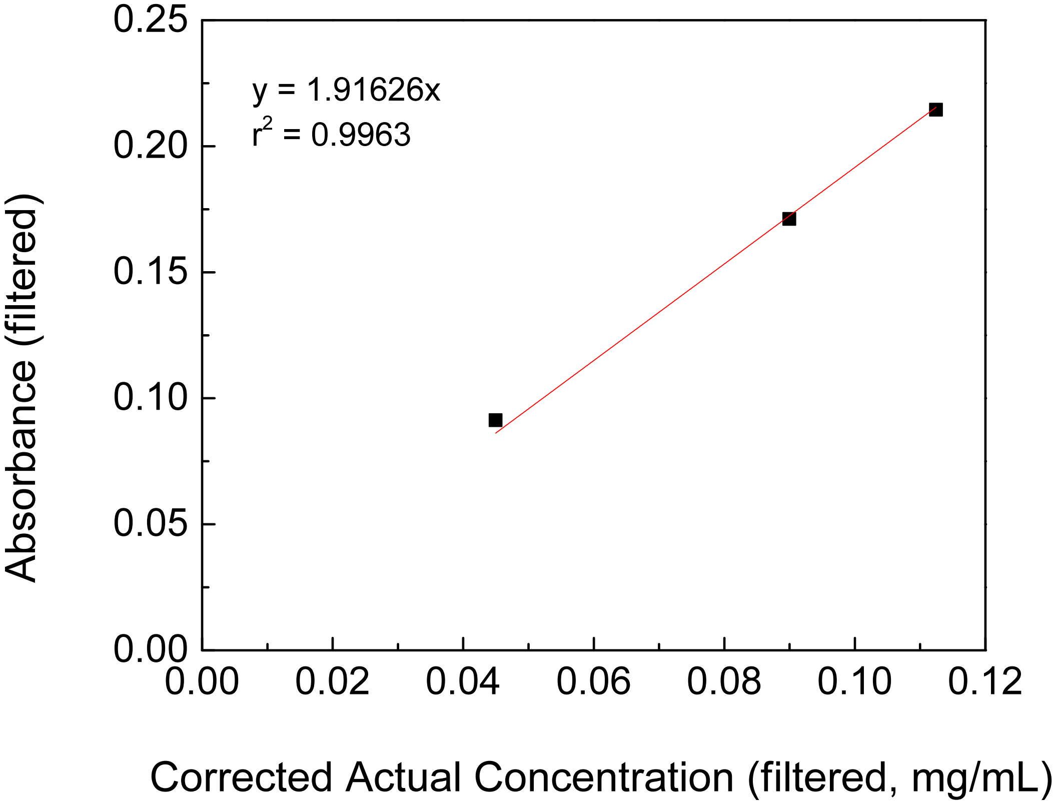

Figure 4.12 TEM of Micromod-amine particles. TEM of Micromod-amine particles shows an average iron oxide core cluster size of 24 ± 3 nm.

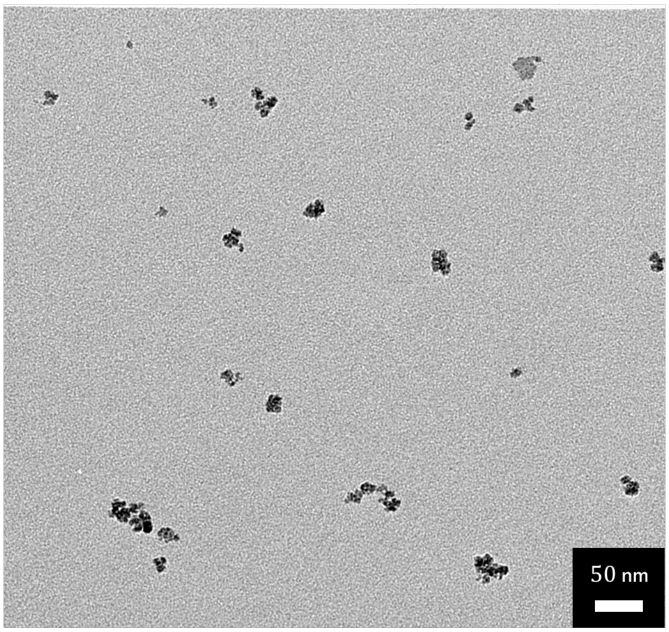

References:

[1] Saritas EU, Goodwill PW, Croft LR, Konkle JJ, Lu K, Zheng B, et al. Magnetic particle imaging (MPI) for NMR and MRI researchers. J Magn Reson 2013;229:116-26.
[2] Goodwill PW, Conolly SM. The X-space formulation of the magnetic particle imaging process: 1-D signal, resolution, bandwidth, SNR, SAR, and magnetostimulation. IEEE Trans Med Imaging. 2010;29:1851-9.
[3] Gleich B, Weizenecker J. Tomographic imaging using the nonlinear response of magnetic particles. Nature. 2005;435:1214-7.
[4] Goodwill PW, Tamrazian A, Croft LR, Lu CD, Johnson EM, Pidaparthi R, et al. Ferrohydrodynamic relaxometry for magnetic particle imaging. Appl Phys Lett 2011;98:262502.
[5] Goodwill PW, Saritas EU, Croft LR, Kim TN, Krishnan KM, Schaffer DV, et al. X-space MPI: magnetic nanoparticles for safe medical imaging. Adv Mater 2012;24:3870-7.
[6] Saritas EU, Goodwill PW, Zhang GZ, Conolly SM. Magnetostimulation limits in magnetic particle imaging. IEEE Trans Med Imaging. 2013;32:1600-10.
[7] Weissleder R, Stark DD, Engelstad BL, Bacon BR, Compton CC, White DL, et al. Superparamagnetic iron oxide: pharmacokinetics and toxicity. AJR Am J Roentgenol 1989;152:167-73.
[8] Ferrucci JT, Stark DD. Iron oxide-enhanced MR imaging of the liver and spleen: review of the first 5 years. AJR Am J Roentgenol 1990;155:943-50.
[9] Lu M, Cohen MH, Rieves D, Pazdur R. FDA report: Ferumoxytol for intravenous iron therapy in adult patients with chronic kidney disease. Am J Hematol 2010;85:315-9.
[10] Coresh J, Astor BC, Greene T, Eknoyan G, Levey AS. Prevalence of chronic kidney disease and decreased kidney function in the adult US population: Third National Health and Nutrition Examination Survey. Am J Kidney Dis. 2003;41:1-12.
[11] Reddan DN, Szczech LA, Tuttle RH, Shaw LK, Jones RH, Schwab SJ, et al. Chronic kidney disease, mortality, and treatment strategies among patients with clinically significant coronary artery disease. J Am Soc Nephrol 2003;14:2373-80.
[12] McCullough PA. Contrast-induced acute kidney injury. J Am Coll Cardiol 2008;51:1419-28.
[13] Kuo PH, Kanal E, Abu-Alfa AK, Cowper SE. Gadolinium-based MR contrast agents and nephrogenic systemic fibrosis. Radiology 2007;242:647-9.
[14] Libby P. Inflammation in atherosclerosis. Nature 2002;420:868-74.
[15] Lewis DR, Kamisoglu K, York AW, Moghe PV. Polymer-based therapeutics: nanoassemblies and nanoparticles for management of atherosclerosis. Wiley Interdiscip Rev Nanomed Nanobiotechnol 2011;3:400-20.
[16] Finn AV, Nakano M, Narula J, Kolodgie FD, Virmani R. Concept of vulnerable/unstable plaque. Arterioscler Thromb Vasc Biol 2010;30:1282-92.
[17] Vallabhajosula S, Fuster V. Atherosclerosis: imaging techniques and the evolving role of nuclear medicine. J Nucl Med 1997;38:1788-96.
[18] Zaman AG, Helft G, Worthley SG, Badimon JJ. The role of plaque rupture and thrombosis in coronary artery disease. Atherosclerosis 2000;149:251-66.
[19] Hansson GK, Libby P. The immune response in atherosclerosis: a double-edged sword. Nat Rev Immunol 2006;6:508-19.

[20] Flacke S, Fischer S, Scott MJ, Fuhrhop RJ, Allen JS, McLean M, et al. Novel MRI contrast agent for molecular imaging of fibrin: implications for detecting vulnerable plaques. Circulation 2001;104:1280-5.
[21] Simberg D, Duza T, Park JH, Essler M, Pilch J, Zhang LL, et al. Biomimetic amplification of nanoparticle homing to tumors. Proc Natl Acad Sci U S A 2007;104:932-6.
[22] Overoye-Chan K, Koerner S, Looby RJ, Kolodziej AF, Zech SG, Deng Q, et al. EP-2104R: A fibrin-specific gadolinium-based MRI contrast agent for detection of thrombus. J Am Chem Soc 2008;130:6025-39.
[23] Yu X, Song SK, Chen J, Scott MJ, Fuhrhop RJ, Hall CS, et al. High-resolution MRI characterization of human thrombus using a novel fibrin-targeted paramagnetic nanoparticle contrast agent. Magn Reson Med 2000;44:867-72.
[24] Sirol M, Fuster V, Badimon JJ, Fallon JT, Moreno PR, Toussaint JF, et al. Chronic thrombus detection with in vivo magnetic resonance imaging and a fibrin-targeted contrast agent. Circulation 2005;112:1594-600.
[25] Song Y, Huang Z, Xu J, Ren D, Wang Y, Zheng X, et al. Multimodal SPION-CREKA peptide based agents for molecular imaging of microthrombus in a rat myocardial ischemia-reperfusion model. Biomaterials 2014;35:2961-70.
[26] Pilch J, Brown DM, Komatsu M, Jarvinen TA, Yang M, Peters D, et al. Peptides selected for binding to clotted plasma accumulate in tumor stroma and wounds. Proc Natl Acad Sci U S A 2006;103:2800-4.
[27] Peters D, Kastantin M, Kotamraju VR, Karmali PP, Gujraty K, Tirrell M, et al. Targeting atherosclerosis by using modular, multifunctional micelles. Proc Natl Acad Sci U S A 2009;106:9815-9.
[28] Lempens EHM, Merkx M, Tirrell M, Meijer EW. Dendrimer display of tumor-homing peptides. Bioconjug Chem 2011;22:397-405.
[29] Berndt P, Fields GB, Tirrell M. Synthetic lipidation of peptides and amino acids: monolayer structure and properties. J Am Chem Soc 1995;117:9515-22.
[30] Knorr R, Trzeciak A, Bannwarth W, Gillessen D. New coupling reagents in peptide chemistry. Tetrahedron Lett 1989;30:1927-30.
[31] Fields GB, Noble RL. Solid phase peptide synthesis utilizing 9-fluorenylmethoxycarbonyl amino acids. Int J Pept Protein Res 1990;35:161-214.
[32] Josephson L, Tung CH, Moore A, Weissleder R. High-efficiency intracellular magnetic labeling with novel superparamagnetic-Tat peptide conjugates. Bioconjug Chem 1999;10:186-91.
[33] Goodwill PW, Conolly SM. Multidimensional x-space magnetic particle imaging. IEEE Trans Med Imaging 2011;30:1581-90.
[34] Whitman SC. A practical approach to using mice in atherosclerosis research. Clin Biochem Rev 2004;25:81-93.
[35] J. Coates, in: R.A. Meyers (Ed.), Encyclopedia of Analytical Chemistry, J. Wiley & Sons Ltd, UK, 2000, p. 1-23.
[36] Diehl KH, Hull R, Morton D, Pfister R, Rabemampianina Y, Smith D, et al. A good practice guide to the administration of substances and removal of blood, including routes and volumes. J Appl Toxicol 2001;21:15-23.
[37] Getz GS, Reardon CA. Animal Models of Atherosclerosis. Arterioscler Thromb Vasc Biol 2012;32:1104-15.

[38] Drews LB, Croft LR, Kosuge H, Saritas EU, Goodwill PW, McConnell MV, et al. Imaging atherosclerotic plaques in vivo using peptide-functionalized iron oxide nanoparticles. Magnetic Particle Imaging (IWMPI), 2013 International Workshop on. doi: 10.1109/IWMPI.2013.6528388.
[39] Kelly KA, Allport JR, Tsourkas A, Shinde-Patil VR, Josephson L, Weissleder R. Detection of vascular adhesion molecule-1 expression using a novel multimodal nanoparticle. Circ Res 2005;96:327-36.
[40] Michalska M, Machtoub L, Manthey HD, Bauer E, Herold V, Krohne G, et al. Visualization of vascular inflammation in the atherosclerotic mouse by ultrasmall superparamagnetic iron oxide vascular cell adhesion molecule-1-specific nanoparticles. Arterioscler Thromb Vasc Biol 2012;32:2350-7.
[41] Kelly KA, Nahrendorf M, Yu AM, Reynolds F, Weissleder R. In vivo phage display selection yields atherosclerotic plaque targeted peptides for imaging. Mol Imaging Biol 2006;8:201-7.
[42] Kitagawa T, Kosuge H, Uchida M, Dua MM, Iida Y, Dalman RL, et al. RGD-conjugated human ferritin nanoparticles for imaging vascular inflammation and angiogenesis in experimental carotid and aortic disease. Mol Imaging Biol 2012;14:315-24.
[43] Burtea C, Laurent S, Murariu O, Rattat D, Toubeau G, Verbruggen A, et al. Molecular imaging of alpha v beta3 integrin expression in atherosclerotic plaques with a mimetic of RGD peptide grafted to Gd-DTPA. Cardiovasc Res 2008;78:148-57.
[44] Alexis F, Pridgen E, Molnar LK, Farokhzad OC. Factors affecting the clearance and biodistribution of polymeric nanoparticles. Mol Pharm 2008;5:505-15.
[45] Kircher MF, Grimm J, Swirski FK, Libby P, Gerszten RE, Allport JR, et al. Noninvasive in vivo imaging of monocyte trafficking to atherosclerotic lesions. Circulation 2008;117:388-95.
[46] Choi HS, Liu W, Misra P, Tanaka E, Zimmer JP, Ipe BI, et al. Renal clearance of quantum dots. Nat Biotechnol 2007;25:1165-70.
[47] Rao J. Shedding light on tumors using nanoparticles. ACS Nano 2008;2:1984-6.

Chapter 5

Characterization of Mixed Micelle Formation using Multiple Peptide Amphiphiles

Abstract

The growing use of nanoparticle systems to address challenges in biomedicine establishes a need to understand the potential of these materials to be amended for different applications. These applications dictate nanoparticles of a certain size and shape. Peptide amphiphiles self-assemble into a variety of structures such as micelles, which can be loaded with hydrophobic drugs or imaging agents, or cylindrical micelles that form fibrous networks and are therefore an ideal material for a wide range of biomedical applications. Mixing of a variety of amphiphiles provides a means to form micelles with the capability of serving multiple functions. Establishing the ability to combine different amphiphiles within the same micelle, however, is key to developing such multifunctional materials. In this work, the extent of mixing in the formation of micelles with two different amphiphiles is assessed. The ability to form micelles with a uniform geometry when combining amphiphiles individually known to produce different geometry micelles is also shown. Even when a mixed population of spherical and cylindrical micelles is observed, Förster resonance energy transfer (FRET) provides evidence for the ability to incorporate different peptide amphiphiles into one micelle. Amphiphiles known to form spherical micelles are additionally shown to alter the geometry of amphiphiles that customarily produce cylindrical micelles. Through these studies, the formation of mixed micelles is not only characterized, but shows the functionality of peptide amphiphile micelles for a multitude of different applications.

5.1 Introduction

Peptide amphiphile micelles represent a unique class of self-assembling materials with the ability to form distinct, single population nanoparticles. Due to their self-assembled nature, the inclusion of multiple amphiphiles in the same micelle is not only possible, but presents one of the definite advantages of this nanoparticle system. While the formation of mixed micelles has been previously presented in the literature [1], the use of mixing to dictate the shape of micelle formed as well as the extent of mixing has yet to be discussed in depth. Given the growing use of peptide amphiphile micelles, particularly in biomedical applications, the shape and size of micelle formed has become exceedingly important and has been shown to affect the biodistribution and circulation time of the resulting nanoparticle [2-5].

Peptide amphiphiles self-assemble in aqueous solution to form micelles above the critical micelle concentration (CMC) and are formed through the conjugation of a hydrophilic peptide headgroup to a hydrophobic tail [6-9]. Peptide amphiphile micelles are advantageous for biomedical applications due to their low CMCs [10], leading to good stability, and incorporation of short peptides versus whole proteins. Small, spherical nanoparticles with diameters ranging from 10-200 nm have been shown to have an increase in circulation time when intravenously injected [10]. Peptide amphiphile micelles have also been shown to self-assemble into long, cylindrical micelles capable of forming gel-like structures for tissue engineering applications [11-14]. Self-assembly allows for the incorporation of a mixture of amphiphiles to tune the stiffness of gel formed [11]. Each application dictates certain size and shape nanoparticles, thus the ability to control these attributes could greatly enhance the self-assembled micelle platform. Previous work using hydrophobically-modified dendrimers to template the formation of spherical nanoparticles from otherwise cylindrical micelle or vesicle forming peptide amphiphiles provided a construct to facilitate sphere formation [15]. However, the capability to form small, spherical micelles without introducing additional molecules would provide a means to maintain the desirable small size and loading capacity of micelles. As an example, currently used peptide amphiphile micelles for vaccine applications employ cylindrical nanoparticles [16]. Injection of spherical micelles formed from the same cylindrical micelle forming amphiphiles may lead to an increase in the cellular uptake of the micelles and therefore form a potentially more effective vaccine. In addition, the ability to simply change the percentage of peptide displayed per micelle may increase the capacity of injected micelles to bind to their intended target [17]. Creating micelles that display an excess of peptide may inhibit binding due to the interaction among peptides as well as crowding between peptides that prevents interaction between the peptide and the desired target.

The formation of uniformly mixed micelles, however, is difficult to detect. Förster resonance energy transfer (FRET) can be used to show that mixing between different dye-labeled amphiphiles is occurring, however, quantification of the extent of mixing is rarely done. In this work, three different mixed micelle systems are evaluated to determine the point at which one population of mixed micelles is formed. Two differing hydrophobic tails, diC$_{16}$ and DSPE-PEG$_{2000}$, were utilized in these studies. DSPE-PEG$_{2000}$ is an amphiphile itself combining a hydrophobic alkyl portion with the hydrophilic PEG component. Three micelle systems mixing these hydrophobic tails were analyzed: diC$_{16}$ tail with two different peptides, diC$_{16}$ tail amphiphile combined with a DSPE-PEG$_{2000}$ tail amphiphile, and two DSPE-PEG$_{2000}$ amphiphiles with differing peptides. The ability to mix two amphiphiles with different peptide headgroups would allow for dual targeting of two different targets simultaneously. In this work, the two peptides were chosen to bind to markers of atherosclerotic plaques. CREKA, a five amino acid peptide known to bind to fibrin [1, 18], was evaluated for its ability to form mixed micelles with a VCAM-1 targeting peptide [19]. VCAM-1 is expressed by endothelial cells that line the atherosclerotic plaque and its accessibility to nanoparticles injected into the blood stream makes it a reasonable target for a nanoparticle delivery system. Combining these two targeting peptides would potentially allow for the ability to bind to both early and late stage plaques simultaneously through VCAM-1 and fibrin targeting. Alternatively, mixing of a cylindrical-forming amphiphile, diC$_{16}$CREKA, with an amphiphile previously shown to form spherical micelles [1, 20], was hypothesized to induce sphere formation when mixed with diC$_{16}$CREKA at a critical concentration. The critical concentration for inducing sphere formation in an otherwise cylindrical micelle-forming amphiphile will be considered. Through these studies, the ability to both form mixed micelles as well as the challenges encountered will be discussed.

5.2 Materials and Methods

5.2.1 Peptide Amphiphile Synthesis and Purification

Peptides were synthesized using standard Fmoc peptide synthesis techniques [6, 21, 22] and purchased fully protected on resin from ChinaTech Peptide (Suzhou, China). Resin was swelled in dichloromethane (DCM, Thermo Fisher Scientific, Waltham, MA) for a minimum of 10 minutes prior to removal of the final, N-terminal Fmoc group using 1% 4-methylpiperidine (Sigma-Aldrich, St. Louis, MO) and 2% 1,8-diazabicyclo[5.4.0]undec-7-ene (DBU, Sigma-Aldrich, St. Louis, MO) by volume in dimethylformamide (DMF, Sigma-Aldrich, St. Louis, MO). The Fmoc deprotection reaction was repeated in triplicate for 5 minutes each. To form diC$_{16}$ amphiphiles, a 2x molar excess of hydroxybenzotriazole (HOBt, AAPPTec LLC, Louisville, KY), 2-(1H-Benzotriazole-1-yl)-1,1,3,3-tetramethyluronium hexafluorophosphate (HBTU, AAPPTec LLC, Louisville, KY), *N,N*-diisopropylethylamine (DIPEA, Sigma-Aldrich, St. Louis, MO), and diC$_{16}$ tail were dissolved in DMF with minimal DCM, if required for solubilization, and allowed to react overnight. To add either fluorescein or rhodamine dye, the 1-(4,4-dimethyl-2,6-dioxocyclohexylidene)ethyl (Dde) group was first deprotected using 2% hydrazine by volume (Alfa Aesar, Ward Hill, MA) in DMF. The reaction was done in triplicate for 5 minutes each. Fluorescein dye was added using 1.25 molar excess of HOBt, HBTU, 5-(and-6)-carboxyfluorescein (Life Technologies, Carlsbad, CA), and DIPEA in DMF. The reaction was allowed to proceed for a minimum of 5 hours. Rhodamine dye was similarly added using 5(6)-carboxytetramethylrhodamine (Novabiochem, Darmstadt, Germany). Complete deprotection of the amino acid side chain protecting groups as well as cleavage of the peptide from resin was achieved using a mixture of trifluoroacetic acid (TFA):triisopropylsilane:water:1,2-ethanedithiol (94:1:2.5:2.5) solution. Peptides and peptide amphiphiles were precipitated in cold diethyl ether prior to purification. Purification was completed using reverse phase high performance liquid chromatography (HPLC, Prominence, Shimadzu Corporation, Kyoto, Japan) with a C$_8$ Waters column (Waters Corporation, Milford, MA). The solvent system consisted of water and acetonitrile with 0.1% TFA. To form DSPE-PEG$_{2000}$ amphiphiles, pure peptide was reacted with 1,2-distearoyl-sn-glycero-3-phosphoethanolamine-N-[maleimide(polyethylene glycol)-2000] (DSPE-PEG$_{2000}$-maleimide) (Avanti Polar Lipids, Alabaster, AL) in water using a 10% molar excess of peptide. The reaction mixture was maintained at a pH between 6.5 and 7.5 and allowed to react overnight. Purification was completed as outlined above using a C$_4$ Waters column. Peptides synthesized are outlined in Table 5.1. Product identity was determined using matrix-assisted laser desorption/ionization (MALDI) mass spectrometry (Voyager DE Pro, Applied Biosystems, Life Technologies, Carlsbad, CA). The concentration of PA in solution was determined using amino acid analysis (Molecular Structure Facility, UC Davis, Davis, CA). DSPE-PEG$_{2000}$-fluorescein was synthesized using 5-(and 6-)carboxyfluorescein, succinimidyl ester (NHS-fluorescein, Thermo Fisher Scientific, Waltham, MA) with 10% molar excess DSPE-PEG$_{2000}$-amine (Avanti Polar Lipids, Alabaster, AL) in 10 mM sodium carbonate buffer with 10% methanol by volume overnight at 4°C.

5.2.2 Micelle Formation

Peptide amphiphile monomers were first lyophilized and subsequently dissolved in methanol. Methanol was dried via nitrogen to form a film on the interior wall of a glass vial. Films were dried under vacuum overnight and were rehydrated in water. Aqueous micelle solutions were allowed to equilibrate for a minimum of 3 hours. DiC_{16} micelles were formed via re-hydration of lyophilized peptide amphiphile powders and allowed to equilibrate overnight due to the inability to reliably re-hydrate diC_{16} micelle films.

5.2.3 Characterization of Micelle Size and Shape

To determine the geometry of micelles formed, transmission electron microscopy (TEM) was utilized. Cryogenic transmission electron microscopy (cryo-TEM) samples were prepared using an environmentally controlled Vitrobot Mark IV at 24°C and 100% humidity from FEI. TEM samples were prepared between 0.5 to 10 mg/mL using a 3.5 µL sample. PA solution was loaded onto lacey carbon coated copper grids and blotted using filter paper for 1-3 seconds. Samples were then exposed to liquid nitrogen cooled liquid ethane. Samples were imaged using a FEI Tecnai T20 microscope in a Gatan cryo-holder and were maintained at a temperature below 100 K. Image processing was completed via ImageJ and Gatan Digital Micrograph software. To prepare samples for negative stain TEM, 25 to 100 µM aqueous micelle solutions were formed. Samples were loaded onto ultrathin carbon type-A 400 mesh copper grids using 1 µL of sample. Grids were allowed to nearly dry before being blotted with water to remove salts. Negative stain was achieved using a 1% phosphotungstic acid in water solution using 1 µL of stain and applied for 2 minutes prior to removal of excess solution. Grids were imaged at an accelerating voltage of 120 kV using a FEI Tecnai 12 TEM.

Micelle size was additionally determined using dynamic light scattering (DLS) with a single angle Viscotek 802 DLS (Malvern Instruments, Malvern, UK). Micelle solutions were prepared at 100 µM. To determine the hydrodynamic radii, the Stokes-Einstein equation was used and the diffusion coefficient was determined from the auto correlation function.

5.2.4 Mixed Micelle Characterization

FRET was analyzed using 25 µM peptide amphiphile aqueous solutions. Control samples were formed using the same concentration of each individual amphiphile as was incorporated into the corresponding mixed micelle. Fluorescein and rhodamine, a known FRET pair, were used to label amphiphiles. Samples were maintained at 25°C using a Jasco-FP6500 specrofluorometer (excitation: 475 nm).

5.3 Results

5.3.1 DiC_{16} Peptide Amphiphile Micelles

Cryo-transmission electron microscopy (cryo-TEM) of diC_{16}VCAM micelles showed the formation of small, spherical micelles with a tight size distribution (Figure 5.1, a). Spherical objects with a white border are ice, whereas micelles do not have a distinct white border. Negative stain TEM of diC_{16}CREKA micelles illustrated the formation of cylindrical micelles (Figure 5.1, b). Cryo-TEM of a 50:50 mixture of diC_{16}VCAM and diC_{16}CREKA resulted in a mixed population of spherical and cylindrical micelles (Figure 5.1, c). To determine if the spherical and cylindrical micelles represented mixtures of diC_{16}VCAM and diC_{16}CREKA amphiphiles or if they were composed of only diC_{16}VCAM or diC_{16}CREKA amphiphiles alone, an analysis of Förster resonance energy transfer (FRET) was completed. Fluorescein and rhodamine are a known FRET pair. DiC_{16}VCAM was therefore labeled with fluorescein and diC_{16}CREKA was similarly labeled with rhodamine to test for FRET. Figure 5.2 shows a decrease in the fluorescein emission peak and an increase in the rhodamine emission peak versus their respective background values, which is indicative of FRET. The excitation wavelength, 475 nm, was chosen to be sufficiently low such that the resulting control rhodamine emission peak would be small.

To further elicit the ability to form one population of uniform mixed micelles, a range of mole percentages of each amphiphile were evaluated using negative stain TEM (Figure 5.3). Using 10 mole percent of either amphiphile resulted in the formation of one distinct population of micelles. Spherical micelles were observed with 10:90 mole percent diC_{16}CREKA:diC_{16}VCAM. Alternatively, 90:10 mole percent diC_{16}CREKA: diC_{16}VCAM resulted in the formation of only cylindrical micelles. At 30:70 diC_{16}CREKA:diC_{16}VCAM, a majority of spherical micelles were seen via TEM, but the formation of some cylindrical micelles also occurred. As stated above, a mixed population of spherical and cylindrical micelles at 50:50 diC_{16}CREKA:diC_{16}VCAM was observed (Figure 5.1, c). A majority of cylindrical micelles was observed at 70:30 diC_{16}CREKA:diC_{16}VCAM (Figure 5.3). The appearance of FRET was also evaluated with each micelle system. Figure 5.4 shows that FRET was observed at each condition tested, despite the appearance of both spherical and cylindrical micelles with some micelle formulations.

5.3.2 Using DSPE-PEG$_{2000}$ to Confer Spherical Micelles

A solution of 100 mole percent diC_{16}CREKA was shown to form cylindrical micelles (Figure 5.5, a). In order to form spherical micelles, a range of mole percentages of DSPE-PEG$_{2000}$ were incorporated into mixed micelle formulations of diC_{16}CREKA:DSPE-PEG$_{2000}$. 75:25 mole percent diC_{16}CREKA:DSPE-PEG$_{2000}$ resulted in a mixture of both short, cylindrical micelles and spherical micelles (Figure 5.5, b). Further analysis revealed a mixture of cylindrical (Figure 5.6, a) and spherical micelles (Figure 5.6, b). At 50:50 diC_{16}CREKA:DSPE-PEG$_{2000}$, the presence of short, cylindrical micelles was still evident, but an increase in spherical micelles was also observed (Figure 5.5, c). Nearly all micelles imaged via TEM at 25:75 diC_{16}CREKA:DSPE-PEG$_{2000}$ were spherical, but the appearance of a small population of cylindrical micelles did still exist (Figure 5.5, d).

5.3.3 DSPE-PEG$_{2000}$ Peptide Amphiphile Micelles

Using two amphiphiles that independently form spherical micelles, DSPE-PEG$_{2000}$-CREKA and DSPE-PEG$_{2000}$-VCAM, the range of sizes of micelles formed via mixing of these two amphiphiles was evaluated using dynamic light scattering (DLS) (Figure 5.7 and 5.8). A linear relationship between the hydrodynamic diameter of the resulting micelle and the loading percentage of the DSPE-PEG$_{2000}$-VCAM amphiphile was observed (Figure 5.8). Micelles were formed in the range of 12.8 ± 0.6 nm to 21 ± 1 nm.

5.4 Discussion

The multivalent display of numerous targeting peptides is advantageous when developing drug delivery or diagnostic vehicles for diseases such as atherosclerosis where the number of markers of the disease are extensive and change over time. For this reason, the development of a mixed micelle incorporating two different targeting peptides through the use of two amphiphiles was evaluated. By using two amphiphiles that independently formed micelles of different geometries, a visual inspection of the resulting mixed micelle formulations was possible. The combination of TEM and FRET was used to determine not only the morphology of micelles formed, but whether one specific geometry micelle was created from samples where FRET, and therefore mixed micelle formation, was observed. DiC_{16}CREKA was shown to form cylindrical micelles via negative stain TEM whereas diC_{16}VCAM formed spherical micelles as determined from cryo-TEM (Figure 5.1). Micelles formed using a diC_{16} tail have largely been shown to form cylindrical micelles [15, 16, 23]. For this reason, cryo-TEM, which is more accurate for demarking nanoparticles in the 10s of nanometer range because no stain is required, versus negative stain TEM, was used to show that spherical micelles were indeed formed from diC_{16}VCAM. Negative stain TEM can be used to observe these small, spherical micelles on the order of 10-20 nm in diameter, but it can be challenging to distinguish stain from particles. The formation of spheres is not unexpected, though, when considering the critical packing factor [24]. The large headgroup conferred by the charged residues of the VCAM peptide may contribute to the formation of spherical micelles.

Initial mixing of diC_{16}CREKA and diC_{16}VCAM using 50 mole percent of each amphiphile showed the formation of both cylindrical and spherical micelles (Figure 5.1), suggesting that no mixed micelles were formed. Analysis of a 50:50 mixture of diC_{16}CREKA and diC_{16}VCAM using FRET, however, resulted in a decrease in the fluorescein emission peak and an increase in the rhodamine emission peak, showing that FRET was observed with this micelle system (Figure 5.2). Given the use of a low concentration of micelles to avoid interaction among spherical and cylindrical micelles as well as the short distance over which energy transfer can occur to observe FRET, it is expected that fluorescein to rhodamine energy transfer occurred within the same micelle. This suggests that the spherical and/or cylindrical micelles formed are not composed of a single amphiphile, but there is indeed a degree of mixing occurring. In fact, this has been alluded to in the literature where the dissimilarity of the headgroup can affect the ability to induce ideal mixing [25].

Given that some degree of mixing was found using mixed micelles composed of diC_{16}CREKA and diC_{16}VCAM, a range of mole percentages of each amphiphile were formed and analyzed. TEM analysis revealed that a high percentage of greater than 70 mole percent of one amphiphile led to the formation of one uniform population of micelles in terms of micelle shape. Using a majority of diC_{16}CREKA led to cylindrical micelles (Figure 5.3, c and d) and a majority of diC_{16}VCAM resulted in spherical micelles (Figure 5.3, a and b). The formation of mixed micelles was further verified using FRET (Figure 5.4). Observing FRET in each mixed micelle formulation shows the formation of micelles composed of both peptide amphiphiles. Due to the pH-dependence of fluorescein combined with the pH dependent solubility of the histidine-rich VCAM peptide sequence, additional work must be done to maintain the same pH in each micelle formulation, thereby allowing for quantification of the energy transfer in each micelle system and the resulting composition of the mixed micelles. Also, given the high percentage of dye-labeled amphiphile, quenching of the dye is expected and would hinder the ability to quantify the extent of mixing using this system.

In order to attempt to confer a spherical shape to an otherwise cylindrical micelle forming system, the addition of DSPE-PEG$_{2000}$ was used. Unlike the addition of diC$_{16}$VCAM, no additional interaction due to a peptide sequence is involved in this system. Mixtures of diC$_{16}$CREKA and DSPE-PEG$_{2000}$ resulted in the apparent formation of mixed micelles at a high concentration of DSPE-PEG$_{2000}$ (Figure 5.5). Forming cylindrical micelles that incorporated the DSPE-PEG$_{2000}$ monomer was not achieved up to 75% diC$_{16}$CREKA (Figure 5.5 and 5.6). Due to the large headgroup area conferred by the 2,000 molecular weight PEG, it may be expected that DSPE-PEG$_{2000}$ would not easily be incorporated into a cylindrical micelle. Filtering of the peptide amphiphile micelle solutions to remove the cylindrical micelles and leave only spherical micelles was also done to test for FRET. While the initial indication shows some degree of energy transfer, additional studies would need to be done as a large amount of peptide amphiphile was lost to the filtering system (data not shown). These studies show the ability to incorporate an otherwise cylindrical micelle forming amphiphile into a spherical micelle. Due to the desire to inject small, spherical nanoparticles that have been shown to have an increase in cellular uptake versus cylindrical nanoparticles *in vivo* [26], this capability can be quite advantageous and relies solely upon the self-assembled nature of the micelle system. In addition, recent literature has shown that the ability to bind to a target of interest may require only a small percentage of the amphiphiles to present a targeting peptide [17] and this system can be easily amended to alter the percent of monomers within a micelle that incorporate a targeting peptide.

As has been observed, it may be easier to incorporate different amphiphiles into the same micelle when using the same hydrophobic tail with amphiples known to form the same geometry micelle. Therefore, the use of two amphiphiles with the same hydrophobic tail and shown to confer spherical micelles in Chapters 2 and 3 for the CREKA and VCAM micelles, respectively, was also examined. DSPE-PEG$_{2000}$-CREKA and DSPE-PEG$_{2000}$-VCAM were mixed at differing mole ratios and analyzed via DLS. The correlation between average hydrodynamic diameter and the mole percent of DSPE-PEG$_{2000}$-VCAM amphiphile shows a linear trend with the average hydrodynamic diameter of micelles formed between 12.8 ± 0.6 nm to 21 ± 1 nm (Figure 5.8). DLS also showed one population of micelles for each system studied with the trend in diameter being the only change observed (Figure 5.7). This suggests that not only are mixed micelles being formed, but that it is possible to alter the size of the resulting micelle by using amphiphiles of varying lengths. This may be a key component to forming micelles of a desired size and shape as the size of nanoparticle systems and their interaction with the body is better understood. In fact, both size and shape play a large role in the clearance mechanism and circulation time *in vivo* [2, 5].

It should be noted that a different VCAM-1 targeting sequence was used in these studies versus those used in Chapter 3. The sequence presented here is the mirror image of the sequence used in Chapter 3 and may target VCAM-1 just as well as the sequence in Chapter 3, as the orientation from N-terminus to C-terminus of a short peptide may not be as important to binding as the incorporation of the specific amino acids, but the targeting ability of this peptide was not evaluated. However, mixed micelle formation is not expected to be affected by the flipped sequence as the hydrophobic tail has henceforth been shown to dictate the degree of mixed micelle formation.

5.5 Conclusions

From these studies of mixed micelle formation, we can elicit many of the characteristics that dictate the geometry of the micelle that is formed. It was found that two amphiphiles with differing peptide headgroups can be easily formed into mixed micelles when the individual components had the same hydrophobic tail and assembled into the same geometry micelle. In fact, DSPE-PEG$_{2000}$-CREKA and DSPE-PEG$_{2000}$-VCAM each have been previously shown to individually form spherical micelles and their incorporation into mixed micelles provided a means to change the hydrodynamic diameter of spherical micelles. Mixing of two differing hydrophobic tails from amphiphiles known to form dissimilar geometry micelles proved more challenging, but a range over which one single geometry micelle was formed was established. The ability to easily incorporate a spherical-micelle inducing amphiphile into a self-assembled system and alter the shape of the resulting micelle from cylindrical to spherical is quite promising for future applications, particularly in the biomedical regime. Similarly, micelles presenting two different targeting peptides were shown to form mixed micelles. Combining the already promising benefits of self-assembled peptide amphiphile micelles with the ability to dictate the resulting size and shape of micelle formed along with an understanding of the mixing of different amphiphile systems creates a platform for easily designing a micelle system to match the desired application.

Table 5.1 Summary of peptide amphiphiles used to study the formation of mixed micelles.

Peptide Amphiphile	**Peptide Sequence**
diC$_{16}$CREKA	C-aminohexanoic acid-K (rhodamine)-aminohexanoic acid-REKA
diC$_{16}$VCAM	CGGK (fluorescein)-GGVHPKQHR
DSPE-PEG$_{2000}$-CREKA	CREKA
DSPE-PEG$_{2000}$-VCAM	CGKSGGRHQKPHV

Figure 5.1 Mixed micelles formed from diC$_{16}$VCAM and diC$_{16}$CREKA. A 50:50 mixture of diC$_{16}$VCAM (a) and diC$_{16}$CREKA (b) resulted in the formation of both spherical and cylindrical micelles (c).

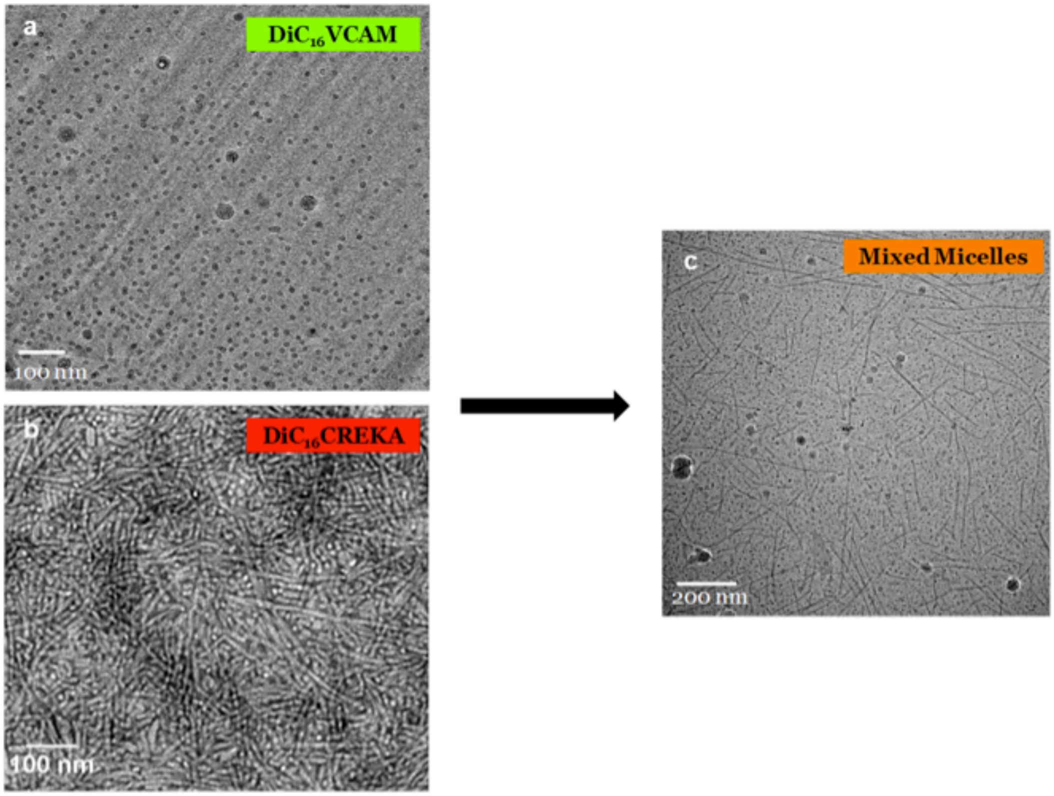

Figure 5.2 FRET shows formation of mixed micelles composed of diC$_{16}$VCAM and diC$_{16}$CREKA. A 50:50 mixture of fluorescein labeled diC$_{16}$-VCAM and rhodamine labeled diC$_{16}$-CREKA at 25 μM exhibit FRET, showing that micelles are composed of both labeled amphiphiles.

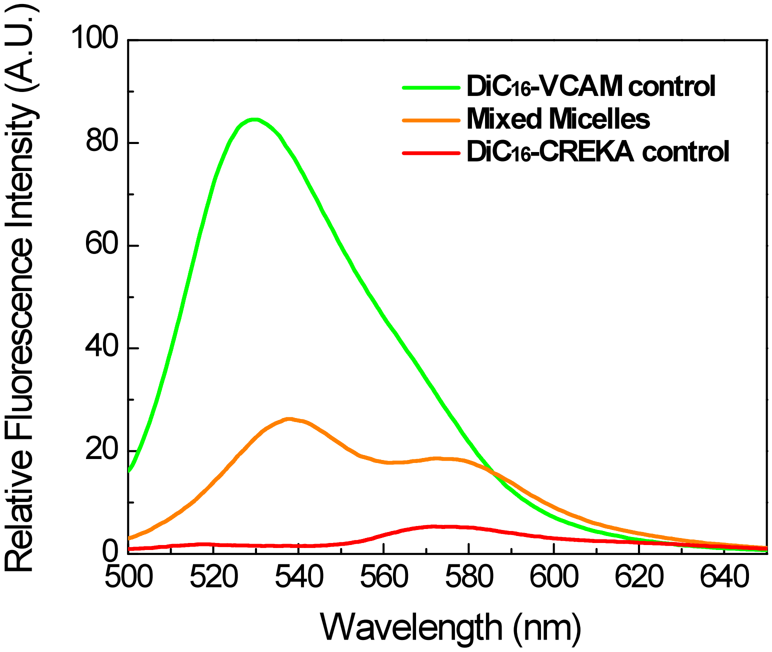

Figure 5.3 Evaluating the extent of mixing in micelles composed of diC$_{16}$VCAM and diC$_{16}$CREKA. An increase in diC$_{16}$VCAM leads to increasingly spherical micelles, whereas the increased addition of diC$_{16}$CREKA led to the formation of cylindrical micelles.

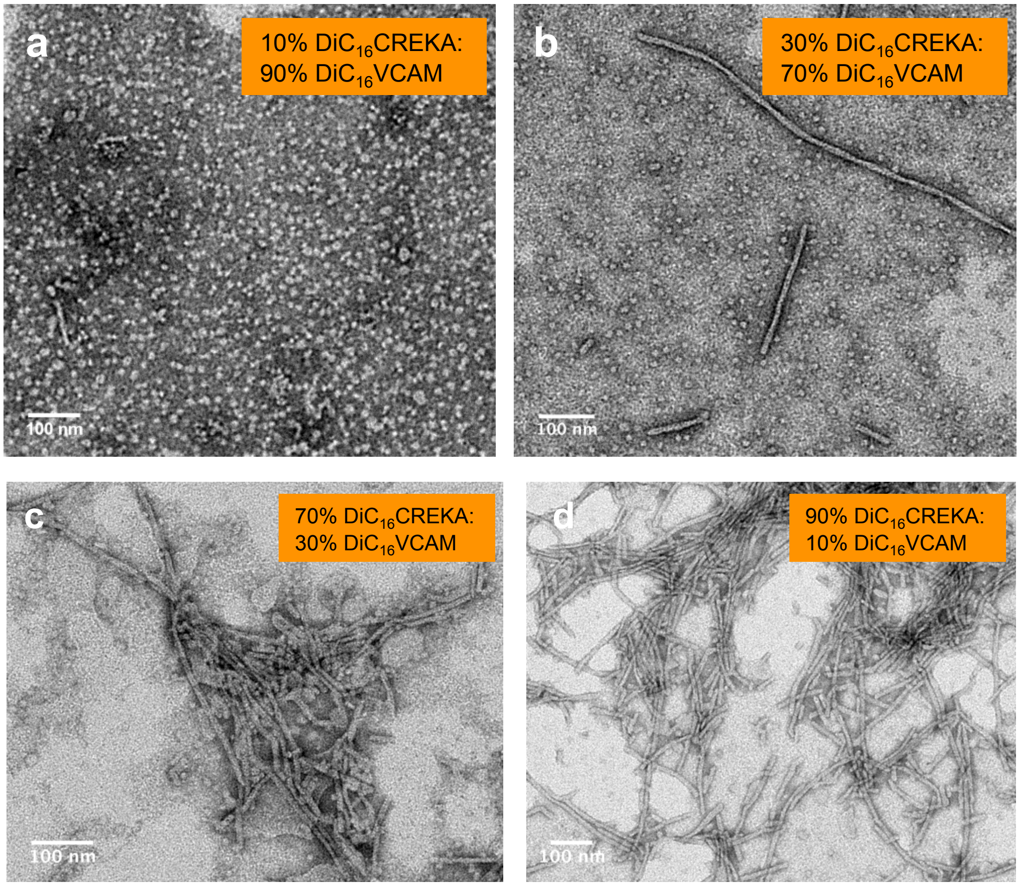

Figure 5.4 FRET shows formation of mixed micelles over a range of compositions. At each composition of diC$_{16}$VCAM and diC$_{16}$CREKA evaluated, FRET is observed, providing evidence for the formation of mixed micelles.

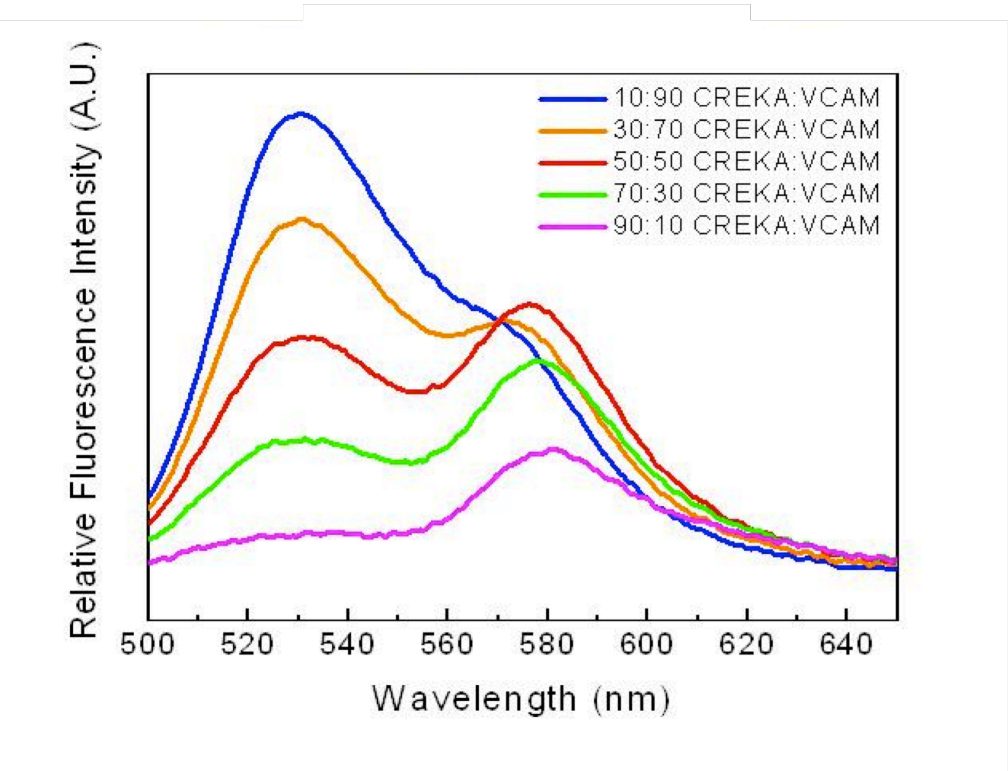

Figure 5.5 Determining the ability to form mixed micelles composed of diC$_{16}$CREKA and DSPE-PEG$_{2000}$-fluorescein. An increase in DSPE-PEG$_{2000}$ amphiphile leads to an increasing amount of spherical micelles. In (d), a majority of spherical micelles are observed, showing the ability to alter the shape of micelle formed by diC$_{16}$CREKA monomers.

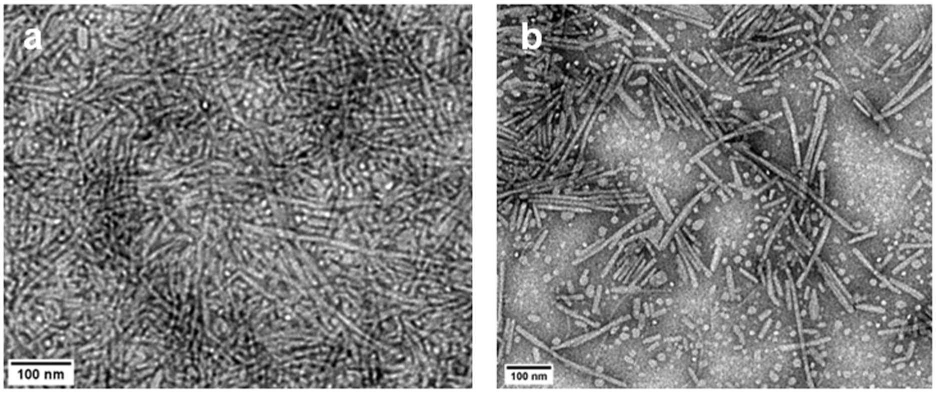

100% DiC$_{16}$CREKA

75% DiC$_{16}$CREKA: 25% DSPE-PEG-fluorescein

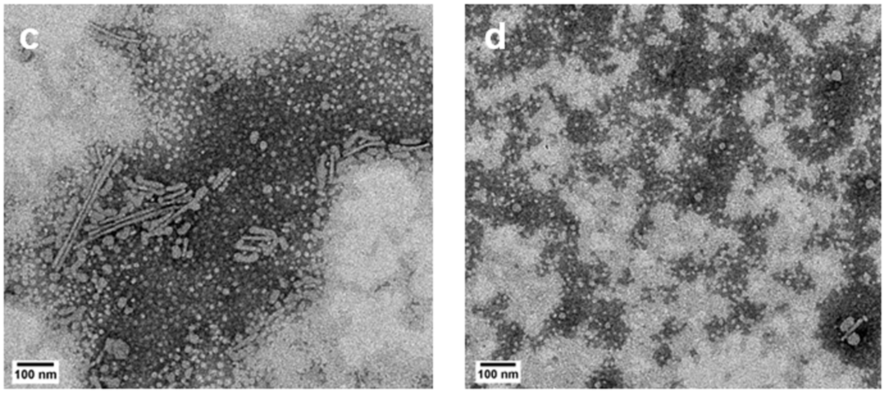

50% DiC$_{16}$CREKA: 50% DSPE-PEG-fluorescein

25% DiC$_{16}$CREKA: 75% DSPE-PEG-fluorescein

Figure 5.6 Analysis of diC$_{16}$CREKA and DSPE-PEG$_{2000}$ mixed micelles. Further examination of the 75:25 mole percent diC$_{16}$CREKA:DSPE-PEG$_{2000}$-fluorescein condition shows the variety of micelles formed. Short, cylindrical micelles are observed in contrast to the long, cylindrical micelles imaged using 100 mole percent diC$_{16}$CREKA.

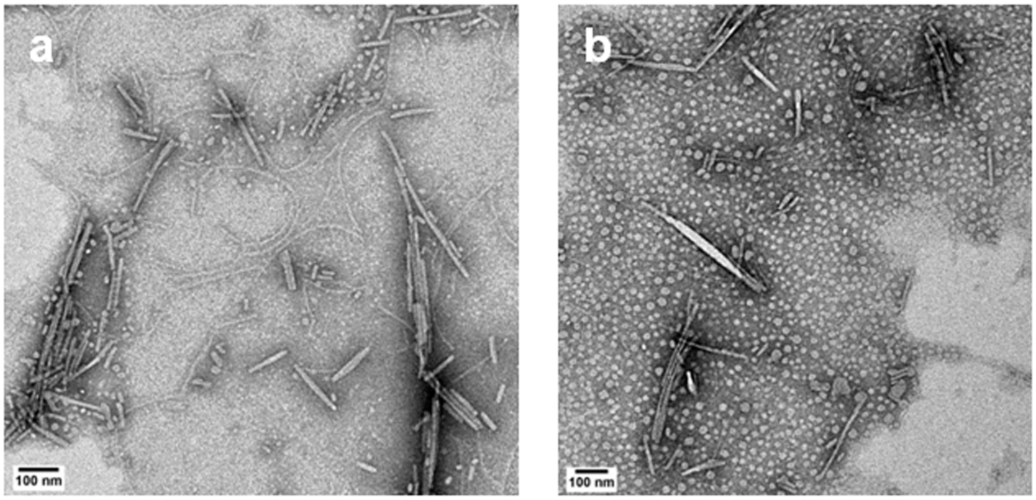

Figure 5.7 Mixing DSPE-PEG$_{2000}$-CREKA and DSPE-PEG$_{2000}$-VCAM. DLS showed a single, tight population of micelles with an increase in hydrodynamic diameter observed as the percentage of DSPE-PEG$_{2000}$-VCAM increased.

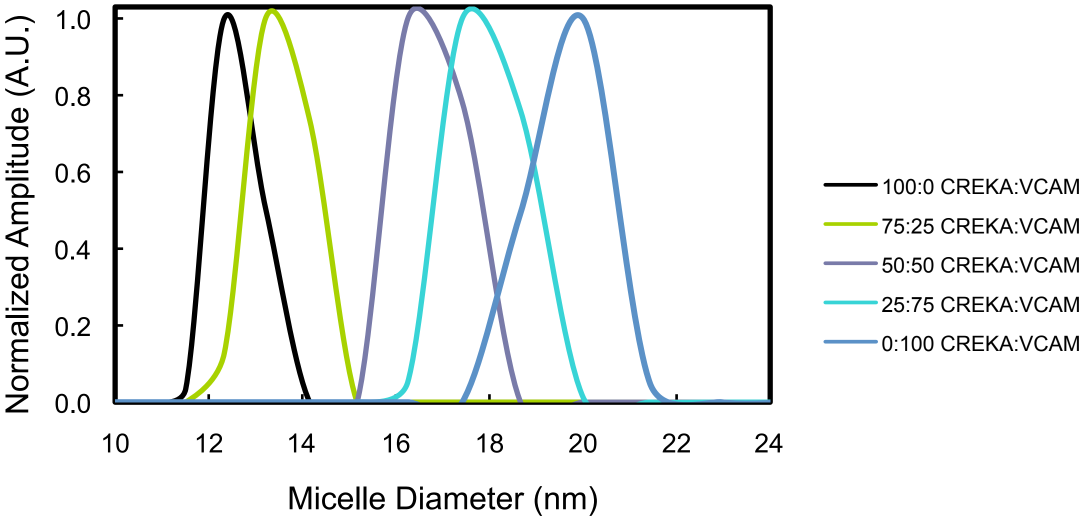

Figure 5.8 Micelle diameter is linearly dependent on the percentage of DSPE-PEG$_{2000}$-VCAM. The hydrodynamic diameter was shown to be linearly dependent on the mole percentage of DSPE-PEG$_{2000}$-VCAM and DSPE-PEG$_{2000}$-CREKA.

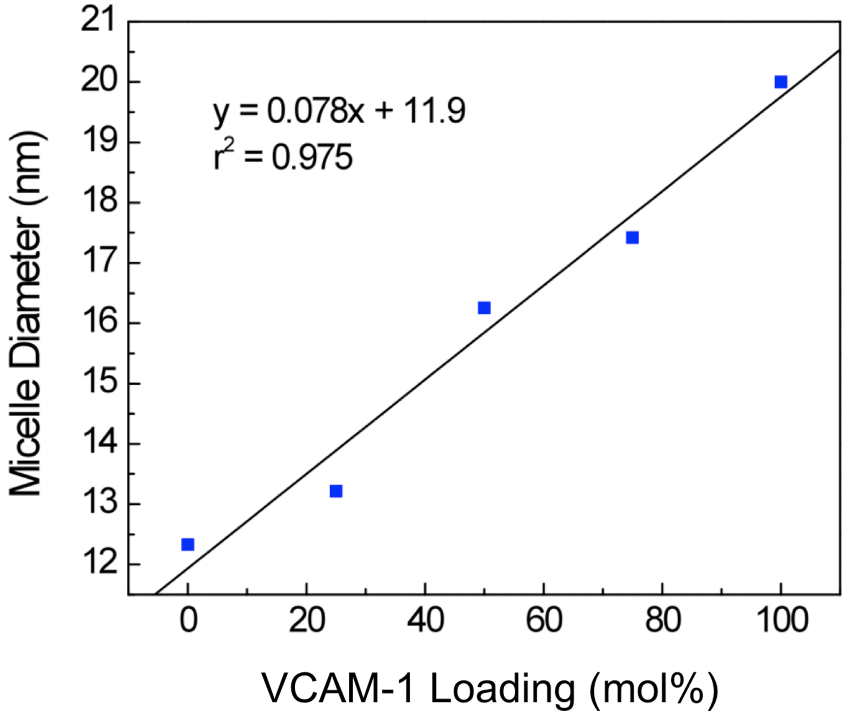

References:

[1] Peters D, Kastantin M, Kotamraju VR, Karmali PP, Gujraty K, Tirrell M, et al. Targeting atherosclerosis by using modular, multifunctional micelles. Proc Natl Acad Sci U S A 2009;106:9815-9.
[2] Champion JA, Walker A, Mitragotri S. Role of particle size in phagocytosis of polymeric microspheres. Pharm Res 2008;25:1815-21.
[3] Torchilin VP. Micellar nanocarriers: Pharmaceutical perspectives. Pharm Res 2007;24:1-16.
[4] Duan X, Li Y. Physicochemical characteristics of nanoparticles affect circulation, biodistribution, cellular internalization, and trafficking. Small 2013;9:1521-32.
[5] Champion JA, Katare YK, Mitragotri S. Particle shape: a new design parameter for micro- and nanoscale drug delivery carriers. J Control Release. 2007;121:3-9.
[6] Berndt P, Fields GB, Tirrell M. Synthetic lipidation of peptides and amino acids: monolayer structure and properties. J Am Chem Soc 1995;117:9515-22.
[7] Hamley IW. Self-assembly of amphiphilic peptides. Soft Matter 2011;7:4122-38.
[8] Cavalli S, Albericio F, Kros A. Amphiphilic peptides and their cross-disciplinary role as building blocks for nanoscience. Chem Soc Rev 2010;39:241-63.
[9] Versluis F, Marsden HR, Kros A. Power struggles in peptide-amphiphile nanostructures. Chem Soc Rev 2010;39:3434-44.
[10] Lewis DR, Kamisoglu K, York AW, Moghe PV. Polymer-based therapeutics: nanoassemblies and nanoparticles for management of atherosclerosis. Wiley Interdiscip Rev Nanomed Nanobiotechnol 2011;3:400-20.
[11] Lin BF, Megley KA, Viswanathan N, Krogstad DV, Drews LB, Kade MJ, et al. pH-responsive branched peptide amphiphile hydrogel designed for applications in regenerative medicine with potential as injectable tissue scaffolds. J Mater Chem 2012;22:19447-54.
[12] Niece KL, Hartgerink JD, Donners JJ, Stupp SI. Self-assembly combining two bioactive peptide-amphiphile molecules into nanofibers by electrostatic attraction. J Am Chem Soc 2003;125:7146-7.
[13] Webber MJ, Tongers J, Newcomb CJ, Marquardt KT, Bauersachs J, Losordo DW, et al. Supramolecular nanostructures that mimic VEGF as a strategy for ischemic tissue repair. Proc Natl Acad Sci U S A 2011;108:13438-43.
[14] Hartgerink JD, Beniash E, Stupp SI. Self-assembly and mineralization of peptide-amphiphile nanofibers. Science 2001;294(5547):1684-8.
[15] Lin BF, Marullo RS, Robb MJ, Krogstad DV, Antoni P, Hawker CJ, et al. De novo design of bioactive protein-resembling nanospheres via dendrimer-templated peptide amphiphile assembly. Nano Lett 2011;11:3946-50.
[16] Black M, Trent A, Kostenko Y, Lee JS, Olive C, Tirrell M. Self-assembled peptide amphiphile micelles containing a cytotoxic T-cell epitope promote a protective immune response in vivo. Adv Mater 2012;24:3845-9.
[17] Kusunose J, Zhang H, Gagnon MK, Pan T, Simon SI, Ferrara KW. Microfluidic system for facilitated quantification of nanoparticle accumulation to cells under laminar flow. Ann Biomed Eng 2013;41:89-99.

[18] Simberg D, Duza T, Park JH, Essler M, Pilch J, Zhang LL, et al. Biomimetic amplification of nanoparticle homing to tumors. Proc Natl Acad Sci U S A 2007;104:932-6.
[19] Kelly KA, Nahrendorf M, Yu AM, Reynolds F, Weissleder R. In vivo phage display selection yields atherosclerotic plaque targeted peptides for imaging. Mol Imaging Biol 2006;8:201-7.
[20] Chung EJ, Cheng Y, Morshed R, Nord K, Han Y, Wegscheid ML, et al. Fibrin-binding, peptide amphiphile micelles for targeting glioblastoma. Biomaterials 2014;35:1249-56.
[21] Knorr R, Trzeciak A, Bannwarth W, Gillessen D. New coupling reagents in peptide chemistry. Tetrahedron Lett 1989;30:1927-30.
[22] Fields GB, Noble RL. Solid phase peptide synthesis utilizing 9-fluorenylmethoxycarbonyl amino acids. Int J Pept Protein Res 1990;35:161-214.
[23] Trent A, Marullo R, Lin B, Black M, Tirrell M. Structural properties of soluble peptide amphiphile micelles. Soft Matter 2011;7:9572-82.
[24] Israelachvili JN. Intermolecular and surface forces. 3rd ed. San Diego: Elsevier; 2011, p. 538-50.
[25] Tanford C. The hydrophobic effect: formation of micelles and biological membranes. New York: Wiley-Interscience; 1973, p. 81-85.
[26] Elsabahy M, Wooley KL. Design of polymeric nanoparticles for biomedical delivery applications. Chem Soc Rev 2012;41:2545-61.